MULTI SCALE TRANSPORT PHENOMENA IN LOW-PRESSURE PLASMAS

BY

MICHAEL JAMES GRAPPERHAUS

B.S., University of Illinois at Urbana-Champaign, 1991
M.S., University of Illinois at Urbana-Champaign, 1993

THESIS

Submitted in partial fulfillment of the requirements
for the degree of Doctor of Philosophy in Nuclear Engineering
in the Graduate College of the
University of Illinois at Urbana-Champaign, 1998

Urbana, Illinois

MULTI SCALE TRANSPORT PHENOMENA IN LOW-PRESSURE PLASMAS

Michael J. Grapperhaus, Ph.D.
Department of Nuclear Engineering
University of Illinois at Urbana-Champaign, 1998
M. J. Kushner, Advisor

Plasma processing for microelectronics fabrication has become important in many steps of integrated circuit production from mask set production to device definition and interconnect production. The non equilibrium chemistry possible in partially ionized plasmas provides an economical method to produce chemical radicals, and in addition, biasing the substrate provides an anisotropic ion flux to surfaces with a controlled energy. As dimensions of the features in microelectronic devices shrink, understanding and control of the plasma properties become increasingly important to ensure quality and reproducibility of processing steps. To model high-density low-pressure processing plasmas, a wide range of length and time scales must be addressed. Length scales range from the Debye length, which is in the range of 1-100 *m*m, to the reactor dimensions, which are tens of cm; time scales range from the plasma frequency of 0.1-10 GHz to the applied voltage frequency, which can be a low as 10-1000 kHz.

Near the boundaries in a plasma, charge separation occurs on scales which are on the order of the Debye length. This means that grid sizes used in the bulk of the plasma, typically a few mm, cannot resolve the behavior near the walls. To accurately represent the boundary conditions, a model which represents the small scales in the sheath region is needed. A sheath model, whose predictions closely match experimental results, has been developed and is integrated within the Hybrid Plasma Equipment Model (HPEM). Plasmas have been examined having inductively coupled powers from 200 to 800 W and rf bias powers from 50 to 400 W for Ar and Ar/Cl_2 gas mixtures. It was found that the sheath voltage wave form remained nearly sinusoidal and that the plasma density, and consequently the ion flux to the surface, scaled primarily with inductively coupled power.

Ionized-metal physical vapor deposition (IMPVD) provides a means of depositing metalization layers with an anisotropic metal flux so that high aspect-ratio features can be filed without the formation of voids. Modifications have been made to the HPEM to model IMPVD systems, including sputtering from surface, electron motion in magnetic fields, and slowing of sputtered atoms to thermal speeds in the plasma volume. The deposition rate of metal on the substrate is found to be reduced as pressure increases due to the increase in diffusive losses. It is also seen that the sputtering of the auxiliary coils can be a significant issue in IMPVD systems, which must be addressed in a realistic tool design.

The surface chemistry in plasma processing reactors plays an important role in the behavior of the entire plasma. Surface topography on the wafer being processed, which determines the chemical behavior of the surface, varies on spatial scales which are much smaller than the reactor dimensions. To account for the surface effects on the plasma behavior, a mesoscale Monte Carlo simulation (MMCS) has been developed which joins the die-scale surface chemistry with the plasma scale in the HPEM. The presence of etch products in the plasma is seen to perturb the bulk plasma. The presence of photoresist redeposition is seen to have a minor, but important, effect on the etch rate. At low pressure, the etch rate is increased, although the probability of a given ion causing an etch is decreased.

ACKNOWLEDGMENTS

I would like to acknowledge the National Science Foundation (NSF), Semiconductor Research Corporation (SRC), University of Wisconsin Engineering Research Center (ERC) for Plasma Aided Manufacturing, Office of Naval Research, Air Force Office of Scientific Research (AFOSR)/Defense Advanced Research Projects Administration (DARPA) Multidisciplinary University Research Initiative, and Sandia/ SEMATECH Cooperative Research Development Agreement (CREDA) on Plasma Modeling.

I give special thanks to my advisor, Professor Mark J. Kushner, for his advice in matters scientific, philosophical and otherwise. I am glad that he was able to, if not understand, at least tolerate my humor. I would like to thank the members of my family for their support and for always believing in me: my dad, Paul, who always reminded me to take time out to go fishing; my mom, Rita, who always made sure I was all right; my brothers, Ken and Craig, their wives, Missie and Melody, and my nephews, Gage and Casey.

I am also grateful to all my fellow ODP lab mates through the years: Rob Hoekstra, Dr. Eric Keiter, Dr. Shahid Rauf, Ron Kinder, Peter Xu, Da Zhang, June Lu, Kelly Voyles, Dr. Fred Huang, Dr. Helen Hwang, Dr. Ann Gentile, Dr. Phillip Stout, Dr. Irène Pérès, Dr. Peter Ventzek, Dr. Jong Won Shon, Dr. Seung Choi, and Jean Sexton.

I would like to thank Matt Campbell for helping to remind me that Arts and Science includes art. I would like to thank Lisa Haynes, who taught me not to be afraid to let it show that I am an engineer. I would also like to thank Bryan and Karen Mason, Jim Bonkowski, Elisa Pascual, Anu Mahajan and Matt Harris. Finally I would like to thank the little people: Tigger, Pooka, Fred, and all the other Sidhe.

TABLE OF CONTENTS

1. Introduction

Plasma processing for microelectronics fabrication has become important in many steps of integrated circuit production from mask set production to device definition and interconnect production. The nonequilibrium chemistry possible in partially ionized plasmas provides an economical method to produce chemical radicals, and in addition, biasing the substrate provides an anisotropic ion flux to surfaces with a controlled energy. As dimensions of the features in microelectronic devices shrink, understanding and control of the plasma properties become increasingly important to ensure quality and reproducibility of processing steps.

High-density plasma sources ([e] > 10^{11} - 10^{12} cm^{-3}) have become important tools in the fabrication of sub-half-micron features in microelectronics devices. These sources typically operate at low pressure, from 1 mTorr to 1 Torr. Low-pressure high-density sources produce more anisotropic etching and deposition than traditional parallel plate plasmas due to the low collisionality of the ions across the thin sheaths obtained in these reactors. Several low pressure-high density sources have been developed in recent years, such as electron cyclotron resonance, helicon wave, surface wave and inductively coupled discharges. Inductively Coupled Plasma (ICP) reactors are one high-plasma-density tool which provides uniform plasma properties across a large substrate. ICP tools have the ability to independently vary the applied substrate voltage and the inductively coupled power with the intent of having independent control of ion energies and ion fluxes to the wafer.[1-6] Previous works have shown that plasma density and ion energies are interdependent, but the desired operating conditions can usually be achieved by the proper combination of inductively coupled power and substrate bias voltage.[3,4]

A schematic of an ICP tool, a generic LAM Transformer Coupled Plasma (TCP) tool, is shown in Fig. 1.1.[3] (All figures/tables appear at the end of the chapter.) The

reactor consists of a spiral coil, which sits on a quartz window. The coil is excited at radio frequency (rf), typically 13.56 MHz, which induces a secondary current in the plasma below the window heating the plasma electrons. Power deposition is usually 100s to a few 1000s W. The substrate is independently biased with 10s to 100s W. The gas pressure is usually a few to 10s mTorr, with a flow rate of 10s to 100s sccm in this case injected from a ring near the quartz window.

In the etching steps of microelectronic device production, the device pattern is transferred to a mask on the wafer surface. This mask allows the etching away of exposed wafer material, so that when the mask is removed, the desired pattern is transferred. A purely chemical etch removes material in all directions at an equal rate because there is no directionality to the fluxes of reactive species. As microelectronic device dimensions become smaller and more closely spaced, it is desirable to etch preferentially in the vertical direction. This can be accomplished in plasma etching tools by reactive ion etching (RIE) in which ions are accelerated across the sheath and therefore strike the surface with an anisotropic angular distribution. Therefore, RIE occurs preferentially in vertical direction.

High-density plasmas have a wide range of length and time scales which must be addressed. Some of the important scales and values typical in plasma processing reactors are shown in Table 1.1. To address issues regarding low-pressure, rf plasmas, such as plasma uniformity, several models have been developed. The first two-dimensional model for rf discharges was published by Tsai and Wu in 1990.[7] This model was later expanded in 1993 to include electron momentum and energy equations.[8-10] Dalvie, Surendra and Selwyn also published a two-dimensional model using the drift diffusion approximation along with the energy equation for electrons and showed the enhanced ionization which occurs at the outer radius of a parallel plate system.[11] A two-dimensional fluid model for rf capacitive plasmas was also published by Boeuf, et al. and

Boeuf and Pitchport in which they were able to show that the existence of a dc self bias for electrodes of unequal size can be predicted in rf models.[12,13] Ventzek et al. published a two-dimensional hybrid electron Monte Carlo-drift diffusion model for ICP reactors, including rf capacitive coupling on the substrate, which was the first two-dimensional model for inductively coupled discharges.[14] This model included a semi-implicit solution of Poisson's equation. Passchier and Goedheer and Goedheer et al. published a drift diffusion model using a semi-implicit solution of Poisson's equation along with fully implicit time stepping for electron motion.[15,16] Also in 1993, Lymberopoulos and Economou published a two-dimensional model using the finite element method and made comparisons to the GEC reference cell.[17,18]

Porteous et al. published a two-dimensional model for an electron cyclotron resonance discharge using a fluid model for electrons and a Monte Carlo technique for ions in 1994.[19] Stewart et al. and Bukowski et al. published a fluid model for ICP reactors in which comparisons were made between solenoidal and planar coil configurations.[20,21] Ventzek et al. extended their previous model with an off-line ion and neutral Monte Carlo for heavy-body plasma chemistry; they also investigated capacitive coupling from the inductive coils.[22] A two-dimensional fluid code for ICP reactors was published by DiPeso et al. using quasi-neutrality for electrons, but including electron momentum in the azimuthal direction.[23] A two-dimensional ambipolar model for ICP reactors was developed by Paranjpe, in which modifications to enhance the uniformity of the plasma, such as coil positioning and dielectric window contouring, were investigated.[24] Ventzek et al. also used their model to predict plasma uniformity by examining various coil placements and dielectric window configurations.[6]

In 1995, Dai and Wu and Wu and Dai proposed a two-dimensional analytic model for ICP reactors using mode analysis techneques.[25,26] Jager, Berry, Tolliver and Batchelor developed a two-dimensional model to investigate power coupling in a ICP reactor,

including capacitive coupling and line losses in the coils.[27] Kortshagen et al. developed a two-dimensional fluid model for ICP reactors and for replacing the isotropic electron energy equation with a nonlocal electron energy distribution, which depends on total energy.[28] Economou et al. presented a two-dimensional direct simulation Monte Carlo model for the transport of ions and neutrals in high density plasma reactors using results from a fluid model for plasma distributions.[29] Wu et al. published a generalized Monte Carlo flux method model which is two-dimensional in position space and two-dimensional in velocity space.[30]

In 1996, Kolobov et al. presented a two-dimensional nonlocal electron kinetics model for ICP reactors.[31] Collison and Kushner published a hybrid electron Monte Carlo-fluid model including ion drag terms between positive and negative ion species.[32] Also, Hoekstra and Kushner presented a two-dimensional Monte Carlo model for Ion and Neutral species showing low-pressure effects and ion energy-angular distribution functions.[33] Wise et al. published a two-dimensional ambipolar fluid model coupled with a sheath model for rapid two-dimensional solutions in ICP reactors.[34] Kushner et al. published the first three-dimensional fluid model for ICP reactors.[35] Yamada et al. published a model for a multifrequency ICP source with a two-dimensional ambipolar plasma model to examine beat frequency effects.[36] Yang and Wu published a two-dimensional nonlocal kinetics model for ICP reactors.[37]

In 1997, Grapperhaus and Kushner published an rf sheath model integrated into a hybrid electron Monte Carlo-fluid model.[38] Wu et al. published a two-dimensional model for ICP reactors and examined a bell-jar geometry.[39] Rauf and Kushner incorporated noncollisional heating effects in the solution of the azimuthal electric field into a hybrid electron Monte Carlo-fluid model for ICP sources.[40] Two-dimensional modeling of rf plasmas covers a vast range. The fastest models are typically the fully fluid models, especially when the ambipolar approximation is used. Although fluid models can be very

sophisticated, including momentum equations and, in some cases, nonlocal electron energy distributions to capture kinetic effects. On the other end of the range are fully Monte Carlo models, which capture all of the kinetic properties of the plasmas which are particularly important at low presure, but tend to run more slowly. Because of the disparate time scales between the electrons and the heavy species, there has not been a full Monte Carlo simulation of a plasma. There have been many hybrid Monte Carlo-fluid models. The heavy-body Monte Carlo simulations usually take an assumed or previously computed electron density and electron impact source rates and concentrate on long mean free path transport, heavy body chemistry and energy and angular distributions of fluxes to the surface. Electron Monte Carlo simulations are used to capture effects such as noncollisional heating, long mean free path effects such as the disparity between heating and electron impact source locations, and electron impact source rates, which can be significantly impacted by depletion of the electron energy in the tail.

To address these modeling issues, a two-dimensional, cylindrically symmetric, Hybrid Plasma Equipment Model (HPEM) has been developed at the University of Illinois.[6,14,32,33,35,38,40] The HPEM is capable of representing a variety of heating sources from rf capacitive, rf inductive, electron beam, and dc magnetron. Complex geometries can be represented as well as gas flows and electron kinetics. An overview of the HPEM is given in Chapter 2.

In modeling plasma etching equipment having rf biases on the substrate, the rf sheath must be accurately represented to properly simulate the ambipolar fields, electron stochastic heating and the dc bias. In high-plasma-density reactors, the rf sheath width may be $\leq$100s *m*m thick, whereas reactor dimensions are 10s cm.[41-44] Numerically resolving the thin sheath in computer models of these devices therefore requires large computing resources and, in many cases, is impractical. Much progress has been made in developing semi-analytical solutions for rf sheaths as encountered in plasma etching

reactors.[41-48] However, because these semi-analytical models typically require a priori knowledge of the bulk plasma conditions, they must be integrated with plasma equipment models to be applied to conditions of interest.

Several sheath models have been developed in recent years, among them Lieberman,[41,45] Metze et al. (MEO),[46] and Riley.[47] The Lieberman model assumes that the electrons are sufficiently cold to be completely excluded from the sheath region, and that the ions are affected only by the time averaged potential, which is essentially the high-frequency limit. The MEO model allows electrons to have a temperature, but assumes that the ions respond to the instantaneous sheath voltage, which is the low-frequency limit. The unified sheath model developed by Riley is an attempt to bridge the frequency range between these two models. It assumes that the ions move in a time-damped or averaged potential governed by a relaxation time τ_r, which is approximately the ion transit time.

Sheath models typically require the bulk plasma properties as input, and typically make assumptions about the bulk plasma conditions. Two of these assumptions are that the electric field at the sheath edge is assumed to be zero, and that the shape of the total current as a function of time through the sheath must be specified. Since boundary conditions for the sheath have been shown to have an important effect on the sheath voltage and current,[42,43,49,50] sheath models should ultimately be integrated with the solution of the bulk plasma conditions in a self-consistent fashion.

To address the issue of the sheath-length scale, a self-consistent sheath model has been integrated with the HPEM. Due to the fact that the sheath is thin compared to the dimensions of interest, the sheath locally appears to be one-dimensional, and the sheath model (SM) takes advantage of this scaling. The SM consists of a one-dimensional local model which is implemented at each mesh point at the boundary of the plasma and the reactor. The SM tracks the charging/discharging of the sheath during the rf cycle by

integrating, in time, the electron and ion currents into and out of the sheath. Ions are assumed to traverse the sheath without collision in a time-damped potential as in the Riley model. It is also assumed that the electrons within the sheath can be described by a Boltzmann distribution. The charged particle profiles in the sheath are then known, and Poisson's equation can be integrated to determine the sheath-voltage drop at a given location at the boundary and point in time. The sheath voltage drop is then applied as a jump condition in the solution of Poisson's equation in the entire reactor. The sheath model is discussed in Chapter 3.

Another multiscale phenomenon of interest is the sputter deposition of metals.[51-54] A common method for metal deposition is use of a magnetron discharge. A negative dc voltage of a few hundred volts is applied to the cathode, ions are accelerated though the sheath at the cathode and sputter material from the surface. In addition to sputtering, secondary electrons are emitted, and subsequently are trapped by the strong magnetic field, thus maintain a ring-shaped discharge below the cathode. Pressure is kept low, at a few mTorr, thus most sputtered atoms travel to the wafer surface without scattering, so that uniformity can be better controlled. As microelectronic device dimensions continue to shrink and the aspect ratio (depth to width) of features to be filled increases, the filling of vias between metalization layers during fabrication of microelectronic devices increasingly requires anisotropic deposition fluxes to prevent void formation. Typical magnetron sputter deposition sources emit atoms in a distribution of angles from the sputter surface. This means that the flux of atoms reaching the surface has a wide angular distribution. Although this tends to give good step coverage of low-aspect ratio features, high-aspect ratio features tend to be filled poorly because of the development of overhang structures which can close forming voids as shown in Fig. 1.2.[51,55]

One method used to provide more anisotropic deposition is to introduce columnation between the sputter source and the wafer.[51,56] The disadvantage of this

approach is that deposition rates are greatly reduced since many atoms will be deposited on the collimator. Another approach is to use a metal plasma to deposit the desired film. In this case ions are accelerated across the sheath and arrive with small angular spread. One configuration used to achieve this is a magnetron sputter source in conjunction with an auxiliary plasma source; this technique is referred to as ionized-metal physical vapor deposition (IMPVD).[51-54] The goal is to ionize a significant fraction of the sputtered metal atoms prior to their depositing on the substrate. By applying a bias to the substrate to accelerate the metal ions, an anisotropic deposition flux can be produced. The substrate bias serves the additional purpose of providing a sputter flux (either metal ions or buffer gas ions) which competes with deposition, particularly on the lip of the via, and serves to remove encroaching metal atom deposits which could form voids. The IMPVD technique has been developed and demonstrated by Yamashita[53] and Rossnagel and Hopwood[51,52] for deposition of aluminum and copper. In experiments by Rossnagel and Hopwood, the ionized fraction of the aluminum metal atom flux to the substrate was as large as 90%. A zero-dimensional model of IMPVD has been developed by Hopwood and Qian, and provides results which compare favorably with measurements.[54]

A schematic of a typical IMPVD system is shown in Fig. 1.3. The metal source is a dc magnetron. The bias applied to the substrate can be either dc or rf. The secondary ionization source is an rf powered inductive coil immersed in the plasma. Operating conditions for this system are typically 100's to a few kW power on both the magnetron and the inductive coils, giving electron density in the range of 10^{11} - 10^{13} cm^{-3}. In neutral metal PVD, the buffer gas pressure is usually only a few mTorr with the intent of having metal atoms traverse the reactor from target to substrate having few, if any, collisions. In IMPVD, the buffer gas pressure is somewhat higher (many mTorr to 10s mTorr) with the intent of slowing the sputtered metal atoms in the buffer gas and providing opportunity for them to be ionized. Unfortunately, this also increases the

diffusion losses of metal atoms to surfaces other than the substrate. Experimental scaling studies have shown that, for a constant sputtering rate, the fraction of the metal atoms which are ionized increases with increasing buffer gas pressure while the deposition rate decreases.[54]

Modeling of traditional sputtering systems is typically by Monte Carlo methods,[56,57] which is attractive because of the low operating pressure, typically a few mTorr. A zero-dimensional model of highly ionized metal deposition systems was presented by Hopwood and Qian.[54] To model this process in two dimensions, the HPEM will be used as a starting point to describe the electron kinetics, fluid transport and inductive fields. One problem encountered in using a fluid model for the sputtered atoms is that the emitted atoms typically leave the surface with a few times the binding energy, which is on the order of eV. In this case, a Monte Carlo simulation must be developed to describe the slowing down of these atoms until they reach thermal speeds. In addition, at the pressures of interest for these plasmas, the gyrofrequency is the same order of magnitude as the electron collision frequency. This requires special consideration for the movement of the electrons in the electron kinetics, since the electron can perform a significant fraction of a gyro-orbit before having a collision, yet is too collisional to model as a guiding center motion particle. This has been addressed by modifying the electron time-stepping routine in the electron Monte Carlo module. The IMPVD models are discussed in Chapter 4.

A third multiple-length-scale phenomenon of interest is the effect of surface chemistry. In an etching system there are several effects which can impact the etch rate. A survey of theses effects has been published by Gottscho et al..[58] One effect is macroloading, in which the etch rate decreases as the total area to be etched increases. This effect is especially important in large batch reactors where multiple wafers are processed simultaneously. Another phenomenon which can affect etch rate is aspect-ratio

dependent etching, which is often referred to as RIE lag and reverse RIE lag.[58-64] RIE lag is the effect of high aspect-ratio (depth to width) features etching more quickly than lower aspect-ratio features. One way this may occur is when the transport of neutral species to the bottom of the feature decreases because the size of the feature is smaller than the mean free path of the atom. This leads to a smaller neutral-to-ion flux ratio at the bottom of the feature, since the transport of the neutrals becomes Knudsen-diffusion limited. Because the ratio of neutrals to ions decreases, the etch process can become neutral starved, reducing the etch rate of the high aspect-ratio feature relative to that of a low aspect-ratio feature. Reverse RIE lag is when low aspect ratio features etch more slowly than high aspect ratio features. One possible cause of this is systems in which inhibitor deposition on the sidewalls is needed to prevent isotropic etching. In these systems, the deposition of inhibitor into high aspect-ratio features can be more limited than transport of reactive neutrals. This leads to a reduced etch rate in lower aspect-ratio features, because there is more inhibitor deposited on the bottom of the feature, compared to high aspect features.

Another effect on etch rate is microloading, which is distinct from aspect-ratio dependent etching.[58,59,65] Microloading occurs when there are regions of different pattern density. Features in regions of high pattern density will locally deplete reactive species, resulting in a lower etch rate for features in the high pattern density region compared to regions with lower pattern density. In addition, there can be an effect, in which the inhibitor becomes depleted, compared to reactive species, in regions of high pattern density leading to lower etch rates in regions of low pattern density. A similar effect is seen in chemical vapor deposition systems, where gas-phase reactants are depleted in high pattern density regions, reducing the deposition rate.[66,67]

Feature sizes are on the scale of 0.1's *m*m, die scales are cm's, pattern density varies on orders of mm's, while plasma reactor scales are on orders of 10's cm. This is

illustrated in Fig. 1.4. Creation of etch products on the surface and etching or sputtering of mask material can significantly impact reactor-scale plasma properties. In addition, microloading can affect the local etch rate of different patterns on the die. Futhermore, a related surface chemistry effect can occur because of sputtering and redeposition of photoresist material, which alters the etch rate, since redeposited photoresist must be removed before etching can continue. These processes occur on a length scale of 100s μm[59], yet are tied to reactor length scales because of flow patterns and reactive species production sources. To address the problems related to die-scale etch effects, a Monte Carlo simulation of die-scale etch chemistry has been developed and incorporated within the HPEM. The meso-scale Monte Carlo simulaton (MSMCS) tracks ions and reactive neutrals near and on the surface, including surface chemistry and surface coverage. In order to determine interactions between the bulk plasma scale and the die scale, this model is used to modify the boundary conditions for the fluid portion of the plasma simulation. This model is discussed in Chapter 5.

Table 1.1. Length and time scales of interest in high density plasma processing equipment.

Reactor Dimensions	10's cm
Wafer Diameter	10-30 cm
Neutral Mean Free Path	1-10's cm
Ion Mean Free Path	0.1-10's cm
Sheath Thickness	10-100 μm
Debye Length	1-100 μm
Pattern Surface Features	0.1-10's μm
Applied Voltage Frequency	0.5-100's MHz
Electron Collision Frequency	~10 MHz for typical conditions
Cyclotron Frequency	2.8 MHz/Gauss
Ion Sheath Transit Time	10^{-9}-10^{-10} s
Plasma Frequency	0.1-10 GHz

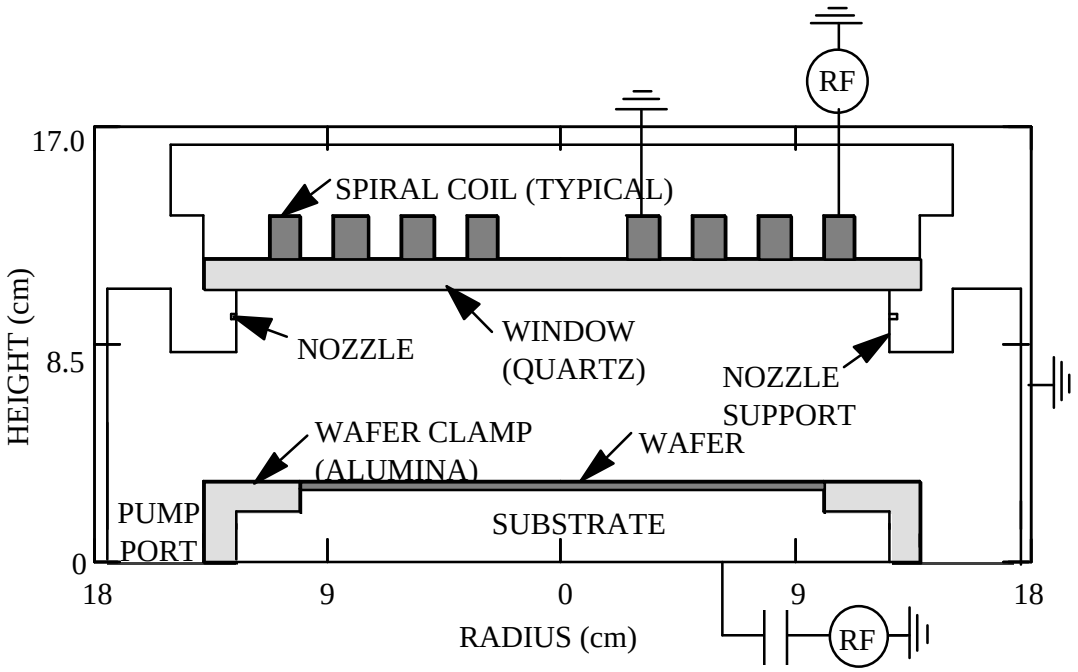

Fig. 1.1. Schematic of an inductively coupled etch reactor.

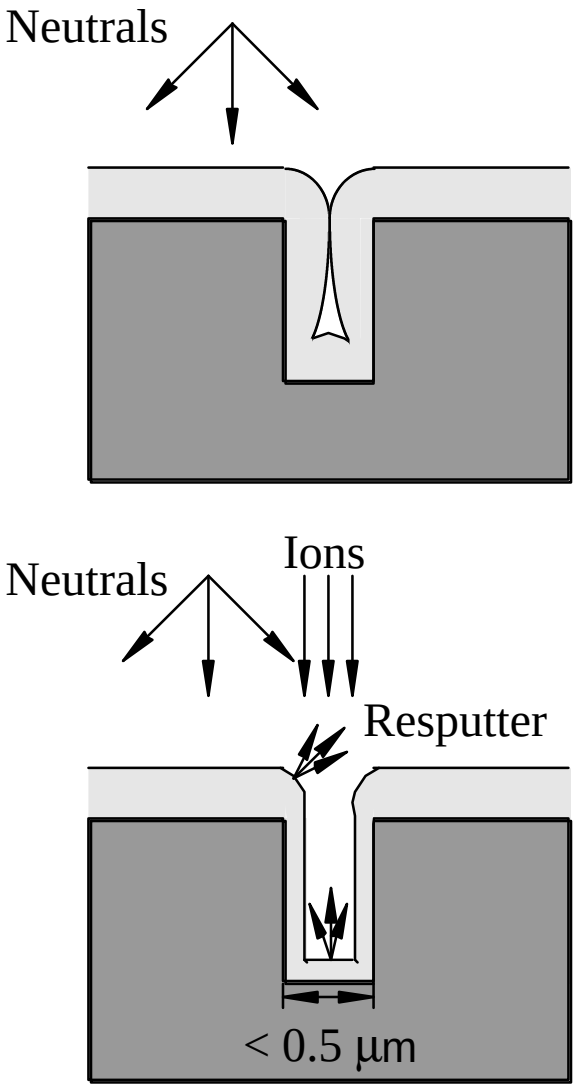

Fig. 1.2. Schematic of a void formed from deposition in a trench caused by preferential deposition higher on the trench wall because of angular spread of incident species. Deposition of ions provides a method to fill features without forming voids.

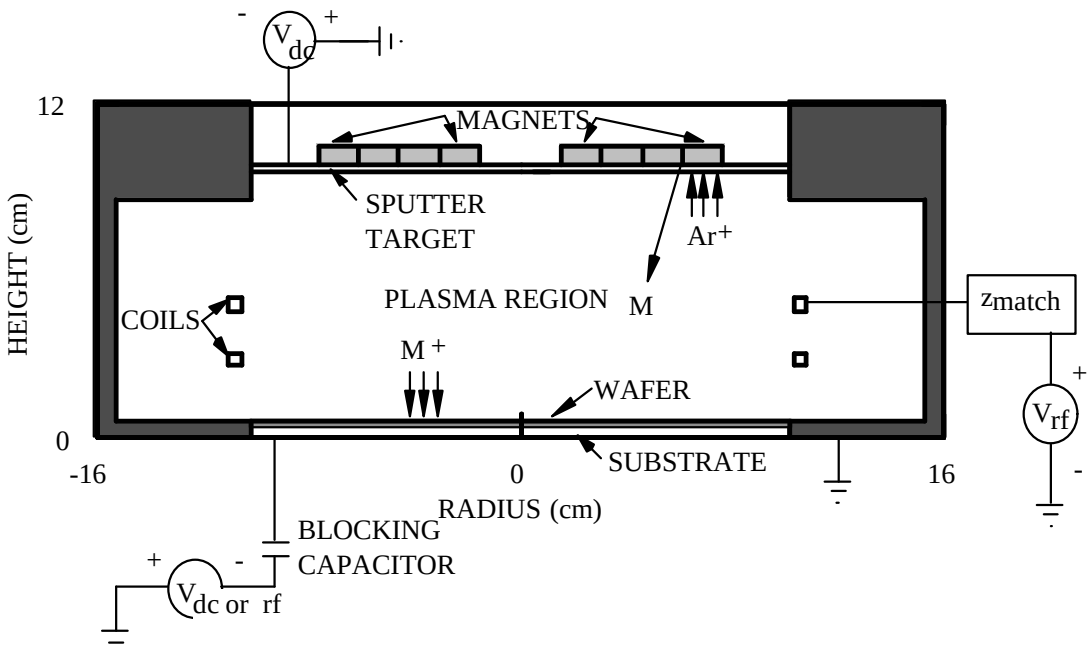

Fig. 1.3. Schematic of a magnetron sputter system.

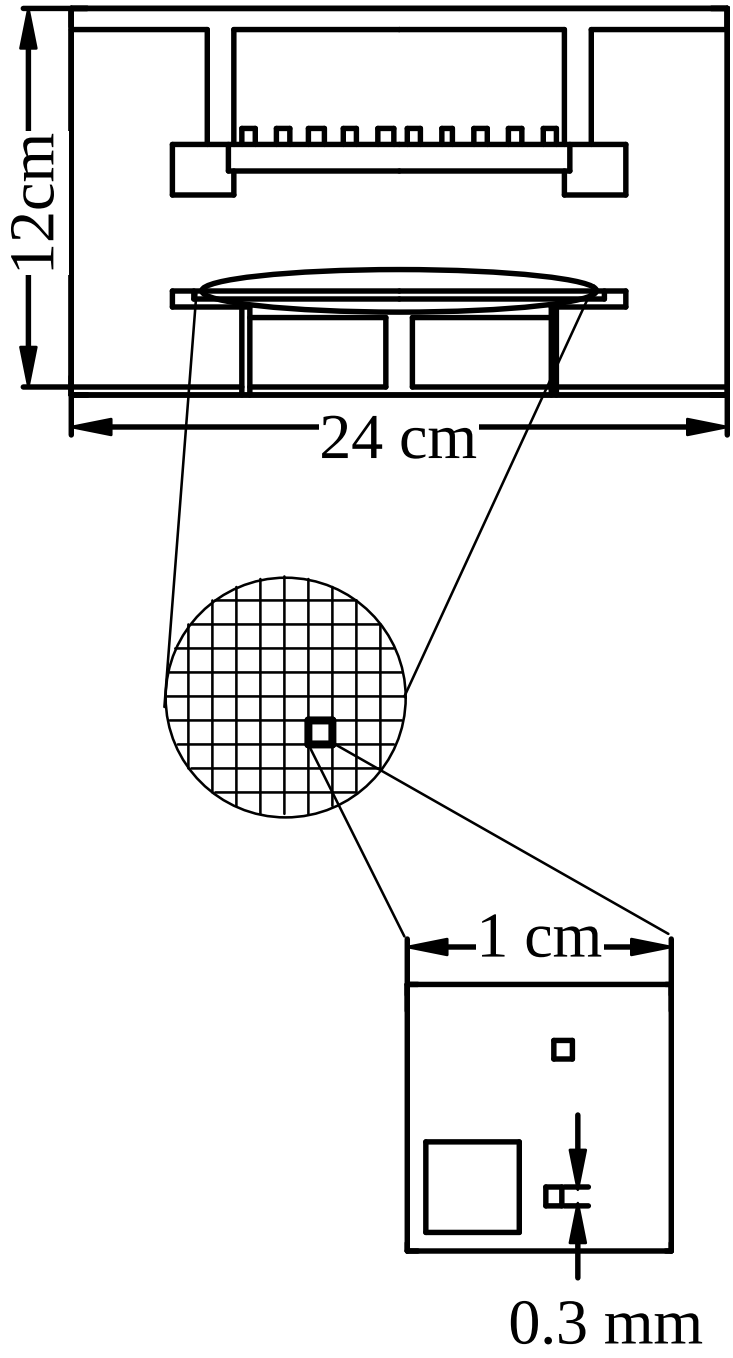

Fig. 1.4. Relative dimensions of interest between the die-scale features and the reactor scale.

1.1 References

[1] J. Hopwood, *Plasma Sources Sci. Tecnol.*, vol. 1, p. 109, 1992.

[2] J. B. Carter, J. P. Holland, E. Peltzer, B. Richardson, E. Bogle, H. T. Nguyen, Y. Melaku, D. Gates and M. Ben-Dor, *J. Vac. Sci. Tecnol. A*, vol. 11, p. 1301, 1993.

[3] J. H. Keller, J. C. Foster and M. S. Barnes, *J. Vac. Sci. Tecnol. A*, vol. 11, p. 2487, 1993.

[4] M. S. Barnes, J. C. Foster and J. H. Keller, *Appl. Phys. Lett.*, vol. 62, p. 2622, 1993.

[5] R. Patric, R. Schoenborn and H. Toda, *J. Vac. Sci. Tecnol. A*, vol. 11, p. 1296, 1993.

[6] P. L. G. Ventzek, M. Grapperhaus and M. J. Kushner, *J. Vac. Sci. Tecnol. B*, vol. 16, p. 3118, 1994

[7] J. H. Tsai and C. Wu, *Phys. Rev. A*, vol. 41, p. 5626, 1990.

[8] F. F. Young and C. Wu, *Appl. Phys. Lett.*, vol. 62, p. 473, 1993.

[9] F. F. Young and C. Wu, *J. Appl. Phys.*, vol. 74, p. 839, 1993.

[10] F. F. Young and C. Wu, *IEEE Trans. Plasma Sci.*, vol. 21, p. 312, 1993.

[11] M. Dalvie, M. Surendra and G. S. Selwyn, *Appl. Phys. Lett.*, vol. 62, p. 3207, 1993.

[12] J. P. Boeuf, L. C. Pitchford, A. Fiala, and Ph. Belenguer, *Surf. and Coat. Technol.*, vol. 59, p. 32, 1993.

[13] J. P. Boeuf and L. C. Pitchford, *Phys. Rev. E*, vol. 51, p. 1376, 1995.

[14] P. L. G. Ventzek, T. J. Sommerer, R. J. Hoekstra and M. J. Kushner, *Appl. Phys. Lett.*, vol. 63, p. 605, 1993.

[15] J. D. P. Passchier and W. J. Goedheer, *J. Appl. Phys.*, vol. 74, p. 3744, 1993.

[16] W. J. Goedheer, P. M. Meijer, J. Bezemer, J. Diederick, P. Passchier and W. G. H. M. van Sark, *IEEE Trans. Plasma Sci.*, vol. 23, p. 644, 1995.

[17] D. P. Lymberopoulos and D. J. Economou, *Appl. Phys. Lett.*, vol. 63, p. 2478, 1993.

[18] D. P. Lymberopoulos and D. J. Economou, *J. Vac. Sci. Technol. A*, vol. 12, p. 1229, 1994.

[19] R. K. Porteous, H.-M. Wu and D. B. Graves, *Plasma Sources Sci. Tecnol.*, vol. 3, p. 25, 1994.

[20] R. A. Stewart, P. Vitello, and D. B. Graves, *J. Vac. Sci. Tecnol. A*, vol. 12, p. 478, 1994.

[21] J. D. Bukowski, D. B. Graves, and P. Vitello, *J. Appl. Phys.*, vol. 80, p. 2614, 1996.

[22] P. L. G. Ventzek, R. J. Hoekstra and M. J. Kushner, *J. Vac. Sci. Technol. B*, vol. 12, p. 461, 1993.

[23] G. DiPeso, V. Vahedi, D. W. Hewett, and T. D. Rognlien, *J. Vac. Sci. Tecnol. A*, vol. 12, p. 1387, 1994.

[24] A. P. Paranjpe, *J. Vac. Sci. Tecnol. A*, vol. 12, p. 1221, 1994.

[25] F. Dai and C. J. Wu, *IEEE Trans. Plasma Sci.*, vol. 23, p. 65, 1995.

[26] C. J. Wu and F. Dai, *IEEE Trans. Plasma Sci.*, vol. 23, p. 74, 1995.

[27] E. F. Jager, L. A. Berry, J. S. Tolliver, and D. B. Batchelor,*Phys. Plasmas*, vol. 2, p. 2598, 1995.

[28] U. Kortshagen, I. Pukropski and L. D. Tsendin, *Phys. Rev. E*, vol. 51, p. 6063, 1995.

[29] D. J. Economou, T. J. Bartel, R. S. Wise and D. P. Lymberopoulos, *IEEE Trans. Plasma Sci.*, vol. 23, p.581, 1995.

[30] C. Wu, C. Li, J.-H. Tsai and F. F. Young, *IEEE Trans. Plasma Sci.*, vol. 23, p. 650, 1995.

[31] V. I. Kolobov, G. J. Parker and W. G. N. Hitchon, *Phys. Rev. E*, vol. 53, p. 1110, 1996.

[32] W. Z. Collison and M. J. Kushner,. *Appl. Phys. Lett.*, vol. 68, p. 903, 1996.

[33] R. J. Hoekstra and M. J. Kushner, *J. Appl. Phys.*, vol. 79, p. 2275, 1995.

[34] R. S. Wise, D. P. Lymberopoulos and D. J. Economou, *Appl. Phys. Lett.*, vol. 68, p. 2499, 1996.

[35] M. J. Kushner, W. Z. Collison, M. J. Grapperhaus, J. P. Holland and M. S. Barnes, *J. Appl. Phys.*, vol. 80, p. 1337, 1996.

[36] N. Yamada, P. L. G. Ventzek, H. Date, Y. Sakai and H. Tagashira, *J. Vac. Sci. Technol. A*, vol. 14, p. 2859, 1996.

[37] Y. Yang and H. Wu, *J. Appl. Phys.*, vol. 80, p. 3699, 1996.

[38] M. J. Grapperhaus and M. J. Kushner, *J. Appl. Phys.*, vol. 81, p. 569, 1997.

[39] H.-M. Wu, B. W. Yu, M. Li and Y. Yang, *IEEE Trans. Plasma Sci.*, vol. 25, p. 1, 1997.

[40] S. Rauf and M. J. Kushner, *J. Appl. Phys.*, vol. 81, p. 5966, 1997.

[41] M. A. Lieberman, *Ieee Trans. Plasma Sci.*, vol. 16, p. 638, 1988.

[42] V. A. Godyak and N. Sternberg, *IEEE Trans. Plasma Sci.*, vol. 18, p.159, 1990.

[43] N. Sternberg and V. A. Godyak, *IEEE Trans. Mag.*, vol. 30, p. 3100, 1994.

[44] K. B”rnig, *Appl. Phys. Lett.*, vol. 60, p. 1553, 1992.

[45] M. A. Lieberman, *Ieee Trans. Plasma Sci.*, vol. 17, p. 338, 1989.

[46] A. Metze, D. W. Ernie, and H. J. Oskam, *J. Appl. Phys.*, vol. 60, p. 3081, 1986.

[47] M. E. Riley, *Sandia Report SAND95-0775.UC-401*, 1995.

[48] V. A. Godyak and N. Sternberg, *Phys. Rev. A*, vol. 42, p. 2299, 1990.

[49] R. Farouki and M. Dalvie, *J. Appl. Phys.*, vol. 68, p. 6106, 1990.

[50] Y. Wang, *Appl. Phys. Lett.*, vol. 66, p. 2329, 1995.

[51] S. M. Rossnagel and J. Hopwood, *J. Vac. Sci. Technol. B*, vol. 12, p. 449, 1994.

[52] S. M. Rossnagel and J. Hopwood, *Appl. Phys. Lett.*, vol. 63, p. 3285, 1993.

[53] M. Yamashita, *J. Vac. Sci. Technol. A*, vol. 7, p. 151, 1989.

[54] J. Hopwood and F. Qian, *J. Appl. Phys.*, vol. 78, p. 758, 1995.

[55] M. A. Lieberman and A. J. Lichtenberg, Principles of Plasma Discharges and Materials Processing, John Wiley and sons, inc., New York, 1994.

[56] A. Kersch, W. Morokoff, C. Werner D. Restaino, and B. Vollmer, *IEDM 92*, p. 181, 1992.

[57] T. Heberlein, G. Krautheim, and W. Wuttke, *Vacuum*, vol. 42, p. 47, 1991.

[58] R. A. Gottscho C. W. Jurgensen and D. J. Vitkavage, *J. Vac. Sci. Technol. B*, vol. 10, p. 2133, 1992.

[59] A. M. Voshchenkov, *J. Vac. Sci. Technol. A*, vol. 11, p. 1211, 1993.

[60] J. C. Arnold, D. C. Gray and H. H. Sawin, *J. Vac. Sci. Technol. B*, vol. 11, p. 2071, 1993.

[61] A. D. Bailey III, M. C. M. van de Sanden, J. A. Gregus and R. A. Gottscho, *J. Vac. Sci. Technol. B*, vol. 13, p. 92, 1995.

[62] A. D. Bailey III and R. A. Gottscho, *Jpn. J. Appl. Phys.*, vol. 34, p. 2083, 1995.

[63] M. F. Doemling, N. R. Rueger and G. S. Oehrlein, *Appl. Phys. Lett.*, vol. 68, p. 10, 1996.

[64] R. J. Xie, J. D. Kava and M. Siegel, *J. Vac. Sci. Technol. A*, vol. 14, p. 1067, 1996.

[65] C. Hedlund, H.-O. Blom, and S. Berg, *J. Vac. Sci. Technol. A*, vol. 12, p. 1962, 1994.

[66] T. S. Cale, J.-H. Park, T. H. Gandy, G. B. Raupp and M. K. Jain, *Chem. Eng. Comm.*, vol. 119, p. 197, 1993.

[67] M. K. Gobbert, C. A. Ringhofer and T. S. Cale, *J. Electrochem. Soc.*, vol. 143, p. 2624, 1996.

2. HYBRID PLASMA EQUIPMENT MODEL

2.1. Introduction

The Hybrid Plasma Equipment Model (HPEM) is a two-dimensional plasma equipment model which has been developed at the University of Illinois.[1-8] The HPEM is capable of modeling complex geometry, a variety of heating sources, and a variety of gas chemistries. The HPEM is a modular code in which a variety of modules can be used or ignored in order to capture the appropriate physics needed to model the equipment desired. An overview of the HPEM is given here to so that the innovations of this thesis work can be understood in the context of the entire code and so that the results presented can be interpreted with an understanding of the assumptions and models used. The HPEM consists of three main sections: the electromagnetic module (EMM), the electron energy distribution function module (EEDFM), and a fluid-chemical kinetics simulation (FKS). The inductively coupled electromagnetic fields and magneto static fields are computed in the EMM, which is discussed in Section 2.2. These fields are used in the EEDFM to generate the electron temperature and electron impact reaction coefficients as a function of position by either an electron Monte Carlo simulation (EMCS) or by solution of the fluid electron energy equation coupled with a solution of the Boltzmann equation; these modules are discussed in Section 2.3. Values computed in the EEDFM are transferred to the FKS, discussed in Section 2.4, in which the plasma species densities and the capacitive electrostatic fields are computed. The densities, conductivity and fields obtained from the FKS are then transferred to the EMM and EEDFM. These three modules are solved successively until a converged solution is obtained.

Within the HPEM there have been numerous modifications which I have made, but which do no warrant individual sections. These include corrections in the implementation of some equations, modifications to the dc self-bias calculation, and the

implementation of current continuity in nonplasma regions, among others. In addition, there are the modifications made for purposes of optimization of algorithms to increase speed of execution, conserve memory usage, and/or increase readability.

2.2. The Electromagnetics Module

The electromagnetics module solves for the frequency-domain electromagnetic fields as well as the electrostatic fields. The solution for the electromagnetic fields requires the knowledge of the plasma conductivity, which is obtained from the other modules. The EMM provides time-harmonic azimuthal electric fields and the static magnetic fields generated by permanent magnets or by equivalent dc loops, that is, currents which change on time scales which are long compared to the time in which the plasma reaches quasi-equilibrium.

The electromagnetics solution for the inductively coupled fields is solved by considering the time harmonic wave equation for electric field, assuming azimuthal symmetry, given by

$$-\nabla \cdot \frac{1}{m} \nabla E_f = w^2 e E_f - iw J_f \tag{2.1}$$

where m is the permeability, e is the permittivity, w is the driving frequency, and the current J_f is the sum of the driving current J_o and the conduction current. The conduction current is assumed to be of the form $J_f = s E_f$. At pressures where the electrons are sufficiently collisional, the conductivity of the plasma is

$$s = \frac{q_e^2 n_e}{m_e} \frac{1}{n_{me} + iw} \tag{2.2}$$

where q is the charge, n_e is the electron density, m is the mass, and n_m is the momentum transfer collision frequency. In Eq. (2.2), the contribution of the ions to the conductivity is ignored because the mobility of the electrons is much greater than that of the ions. In addition, it is possible to make corrections on the conduction current by computing the induced current in the EMCS module.[8]

Boundary conditions for the azimuthal electric field require that E_f=0 on the metal walls, which are assumed to be perfect conductors. Within the coils, the skin depth for penetration of the electric field is smaller than typical mesh sizes, and so the current to the coil is applied only over the surface of the coil within one skin depth. Within the coil, the wave is totally reflected so that on the interior surface of the skin depth, the boundary condition becomes:

$$\frac{\partial E_f}{\partial \mathbf{n}} = 0 \tag{2.3}$$

where **n** is the normal to the interior surface.

Eqs. (2.1-2.3) are discretized with spatial variation allowed for m, e, and, s within the reactor volume. This equation is then separated into real and imaginary components, and the pair of equations is solved simultaneously using the method of successive over relaxation until the solution is converged with a value of $|\Delta E|/|E|$ less than 10^{-6} at all points, where ΔE is the pointwise difference in the values between the current value of E and the value ten iterations before.

The static magnetic fields are solved in the radial and vertical directions assuming azimuthal symmetry. Under these conditions, the magnetic field can be represented as a vector potential **A** which has only a single component in the $\hat{f}$ direction. The magnets

were represented by “filling” a specified material in the numerical mesh with arrays of small current loops (current density **j**) oriented in the appropriate direction to provide the desired orientation of the magnetic field. The current loops provide source terms when solving for vector potential **A** which, by differentiation, yields the static magnetic fields

$$\nabla \times \frac{1}{m} \nabla \times \mathbf{A} = \mathbf{j}, \quad \mathbf{B} = \nabla \times \mathbf{A} \tag{2.4}$$

where m is the local permeability. The boundary condition applied on the vector potential at a distance of twice the reactor radius and height is that **A**=0. This approximates the far field solution by making $\mathbf{B} \cdot \mathbf{n} = 0$ on the outer surface. The vector potential is solved as a boundary-value problem using the method of successive over relaxation, with the same convergence criteria as the electric field.

The coil, its power supply and its matching network are represented are represented by solving an equivalent circuit model for the coil and matchbox to provide coil currents and voltages. The coil currents are used as the driving current boundary conditions in the EMM, and the voltages are used as boundary conditions in the solution of Poisson's equation in the FKS. The circuit model varies the matchbox capacitor values (parallel and series) to minimize the reflected power from the plasma. At the same time, the generator voltage is adjusted to deliver the desired inductively coupled power to the plasma.[6]

2.3. The Electron-Energy Distribution Function Module

In the electron-energy module, the power deposition into the electrons, as well as the electron impact sources, is modeled and the electron transport properties are computed. These can be solved in two different ways in the HPEM. The first method is

to solve the electron energy equation with electron transport properties as a function of temperature computed by solving the zero-dimensional Boltzmann equation. The second method is to run a Monte Carlo simulation, in which electron pseudoparticles are moved in the computed fields and have collisions with the other plasma species. Statistics are gathered to generate the electron energy distribution function (eedf) as a function of position.

2.3.1. The Electron-Energy Equation Method

The electron-energy equation method first solves the zero-dimensional Boltzmann equation numerically for a range of values of electric field divided by total gas density (E/N), in order to create a table of values which correlate E/N with an eedf. This is then used as a lookup table which gives electron mobility, thermal conductivity, energy-loss rate due to collisions, and electron-impact rate coefficients as a function of electron temperature, defined as $\frac{3}{2}\langle e \rangle$ where $\langle e \rangle$ is the average energy computed from the eedf.

With the eedfs known as a function of temperature, the steady state electron energy equation is solved as follows:

$$\nabla k \nabla T_e + \nabla \cdot \left(\Gamma T_e \right) = P_{heating} - P_{loss} \tag{2.5}$$

where T_e is the electron temperature, k is the thermal conductivity, Γ is the electron flux, $P_{heating}$ is the power deposition rate and P_{loss} is the energy-loss rate by collisions. The electron flux Γ is computed in the FKS, and the power deposition rate $P_{heating}$ is computed from the time-averaged value of $sE \cdot E$, where the conductivity s is computed in the FKS and the electric field is both the inductive field computed in the EMM and the capacitively coupled field computed in the FKS. Eq. (2.5) is discretized and solved by

successive over relaxation, with the transport coefficients updated based on the local electron temperature.

2.3.2. The Electron Monte Carlo Method

The electron Monte Carlo simulation (EMCS) tracks the trajectory of electron pseudoparticles by moving them in the computed electric and magnetic fields as a function of time. A group of electrons is initialized from a Maxwellian distribution and randomly distributed within the rf period, with starting locations randomly determined within the reactor volume weighted by the electron density computed in the FKS. The electron-energy range is divided into discrete energy bins for collision determination and for statistic collection purposes. The collision frequency n_i within an energy bin is computed by summing all possible collision within the energy range

$$u_i = \left(\frac{2e_i}{m_e} \right)^{1/2} \sum_{j,k} s_{ijk} N_j \tag{2.6}$$

where e_i is the average energy within the bin, s_{ijk} is the cross section at energy i, for species j and collision process k, and N_j is the number density of species j. The time to next collision is randomly determined using the maximum collision frequency for all energy bins. Then, at the time of collision, the reaction which occurs is randomly determined from all processes possible in that energy bin, with a null reaction making up the difference between the actual collision frequency and the maximum collision frequency.

Particles are moved using the Lorentz equation,

$$\frac{d\mathbf{v}}{dt} = \frac{q_e}{m_e}(\mathbf{E} + \mathbf{v} \times \mathbf{B}) \tag{2.7}$$

where **v** is the velocity, and

$$\frac{d\mathbf{r}}{dt} = \mathbf{v} \tag{2.8}$$

where **r** is the position. Eqs. (2.7-2.8) are updated using a second-order predictor corrector scheme. Electric fields are both the inductive fields computed in the EMM and the time-dependent static fields computed in the FKS. Time steps are chosen to be less than both 1% of the rf period and 1% of the cyclotron frequency, and small enough that the particles do not cross more than one-half computational cell in one time step. Several hundred to a few thousand particles are integrated in time for many rf cycles, typically greater than 100 rf cycles.

At the end of the EMCS, the electron temperature, collision frequency and electron-impact rate coefficients are computed as a function of position. The electron temperature is defined by convention to be $\frac{2}{3}\langle e \rangle$. The electron-impact rate coefficient for electron impact process *i*, k_i, is computed by convolving the eedf with the cross section for the process:

$$k_i = \int_0^\infty \left(\frac{2e}{m_e}\right)^{1/2} s_i \, f de \tag{2.9}$$

where s_i is the energy dependent cross section for process i, and f is the eedf. Eq. (2.9) is computed by summation over the energy bins which have been used to collect the statistics.

2.4. The Fluid-Chemical Kinetics Simulation

The fluid-chemical kinetics simulation solves the fluid transport equations including chemical reactions and Poisson's equation or an ambipolar field solution for the electrostatic potential. To solve these equations, the electron transport properties and the chemical reaction rates are obtained from the EEDFM. Ion and neutral species transport properties are taken from the transport property database within the code or are computed using the known Lenard-Jones parameters and a general mobility formula. The FKS provides the density and fluxes of the plasma species as well as the time-dependent electrostatic fields.

The plasma species densities N_i are computed by solving the continuity equation

$$\frac{\P N_i}{\P t} = -\nabla \cdot \Gamma_i + S_i \tag{2.10}$$

where G_i is the flux and S_i is the source rate for species i. The flux can be computed in two ways for heavy bodies: either by a drift diffusion model or by solving the momentum equation. Electron flux is always computed using the drift diffusion model to allow for an implicit or semi-implicit solution of the electrostatic potential, which is discussed later.

The drift diffusion equation for species flux is

$$\Gamma_i = m_i q_i N_i \mathbf{E} - D_i \nabla N_i \tag{2.11}$$

where m_i is the mobility, q_i is the species charge, and D_i is the diffusion coefficient for species i. When the static magnetic field is nonzero, diffusivities and mobilities for all charged species are resolved into components parallel and perpendicular to the local magnetic field. This is accomplished by defining radial and axial mobilities where, for example,

$$m_r = m_o \frac{1+\left(qB_r / mn_m\right)^2}{1+\left(qB / mn_m\right)^2} \tag{2.12}$$

where m_r is the mobility for radial transport, m_o is the isotropic mobility, B_r is the radial component of the magnetic field, B is total magnitude of the field, and n_m is the momentum-transfer collision frequency.

For heavy bodies, ions and neutrals, there is the option to solve for the species flux G_i using the momentum equation

$$\frac{\P\Gamma_i}{\P t} = -\frac{1}{m_i}\nabla\left(N_i T_i\right) - \nabla\cdot\left(N_i \mathbf{v}_i \mathbf{v}_i\right) + \frac{q_i}{m_i} N_i \mathbf{E} - \sum_j \frac{m_j}{m_i + m_j} N_i N_j \left(\mathbf{v}_i - \mathbf{v}_j\right) n_{ij} \tag{2.13}$$

where $\mathbf{v}_i$ is the species velocity given by $\mathbf{\Gamma}_i/N_i$, T_i is the species temperature in eV, and n_{ij} is the collison frequency between species i and species j. The last term in Eq. (2.13) is summed over all heavy bodies, and results in a drag force. Slip or no-slip boundary conditions can be specified for the tangential components of flux.

For both the momentum equations and for the drift-diffusion equation, boundary conditions for the normal component of the flux for feed stock gases have a fixed flux

value at inlet regions. At the outlet region, the total flux is fixed, with the value for each species dependent on the local value of that species density.

The continuity and the momentum equation, when used, are discretized with a simple first-order time differencing. However, the solution of these equations requires the knowledge of the electrostatic fields. The computation of the time dependent electrostatic fields can be done in one of two ways in the HPEM. The first option is the solution of Poisson's equation; the second option is the solution of a quasi-neutrality condition.

The time step taken in the charged-particle update requires that the fields do not reverse in a single time step. This is known as the dielectric relaxation time, or it can be interpreted as the Courant limit in the current continuity equation. To relax this time-step restriction, the Poisson equation is solved implicitly such that

$$\nabla \cdot e\nabla f^{t+\Delta t} = -r^{t+\Delta t} \tag{2.14}$$

where f^{t+Dt} is the electrostatic potential at time t+Δt, e is the permittivity of the material and equal to e_0 in the plasma region, and r^{t+Dt} is the charge density at time t+Δt. Therefore, the electric fields used in the update of charged-particle flux are at the same time as the new fluxes, and the dielectric relaxation time-step restriction is relaxed. The new charge density at t+Δt is

$$r^{t+\Delta t} = r^{t} + \Delta t \left.\frac{\partial r}{\partial t}\right|^{t+\Delta t}; \qquad \left.\frac{\partial r}{\partial t}\right|^{t+\Delta t} = -\nabla \cdot \mathbf{j} \tag{2.15}$$

where the current density **j** in the plasma region is the sum of all the charged species fluxes times their charge; and in the other regions it is conductivity times electric field. When the drift-diffusion equation is used, then Eqs. (2.14-2.15) can be rearranged as

$$\nabla\cdot\left(\left(e-\Delta ts+\Delta te\sum_i q_i^2 m_i N_i^t\right)\nabla f^{t+\Delta t}\right)=-r^t+\Delta te\nabla\cdot\left(\sum_i q_i D_i\nabla N_i^t-\sum_j q_j\Gamma_j^t\right) \quad (2.16)$$

where s is the material conductivity and is nonzero only outside of the plasma region, e is the elemental charge, q_i is the charge state of the species i, N_i^t is the density of species i at time t, D_i is the diffusion coefficient for species i, and Γ_i^t is the flux for species j at time t. The summations over i are taken only for those species using the drift diffusion model, which the electrons always use, and the summation over j is taken only over species using the momentum equation. Eq. (2.16) is now a modified form of the Poisson equation, and is solved using successive over relaxation.

The second option for computation of the time dependent fields is to use the quasi-neutrality condition. Under this assumption, the electron density n_e is computed assuming that the plasma is quasi neutral at all points, so that

$$n_e=\sum_i q_i N_i \quad (2.17)$$

where N_i is the density of ion species i. The steady-state electron equation can then be solved to determine the electrostatic potential. The steady state drift diffusion equations are then summed and the electron source function is replaced as shown:

$$-\nabla\cdot\left(m_e n_e\nabla f+D_e\nabla n_e\right)=S_e=S_{ext}+\sum_i q_i S_i=\sum_i q_i\nabla\cdot\left(q_i m_i N_i\nabla f-D_i\nabla N_i\right) \quad (2.18)$$

where S_e is the electron source function and is equal to S_{ext}, which is the external electron source such as electron beams, and the sum of the ion sources times their charge state. Eq. (2.18) can be rearranged to give an equation for the electrostatic potential:

$$\nabla \cdot \sum_j \left(q_j^2 m_j N_j \right) \nabla f = \nabla \cdot \sum_j \left(q_j D_j \nabla N_j \right) + \sum_j q_j S_j \qquad (2.19)$$

where the summation over j is now taken over all charged species, including electrons. Eq. (2.19) is discretized and solved by successive over relaxation. By solving the electrons as a steady-state equation, the dielectric time-step restriction is removed, and the continuity equations are restricted only by the Courant limit.

2.5. Typical Results for an ICP Etching Reactor

To demonstrate the kind of information generated by the HPEM, some results are presented in this section. The geometry used in this case is the generic LAM TCP geometry described in chapter 1 and shown in Fig. 1.1. The ICP reactor uses a flat spiral 4-turn coil set on top of a quartz window. The wafer-to-window distance is 7.5 cm. The wafer diameter is 20 cm and is surrounded by an alumina focus ring. The wafer is treated as a uniform disk with a conductivity of 0.05 $(\Omega\text{–cm})^{-1}$. The coils are driven at 13.56 MHz. The gas is Ar at 10 mTorr with an inlet flow rate of 100 sccm. The coils deliver 400 W of inductively coupled power to the plasma. The wafer is biased at 13.56 MHz with 200 W of power deposition.

The two-dimensional electron density and plasma potential are shown in Fig. 2.2. The electron density is relatively uniform in the region above the wafer, which is desirable for uniformity in processing. The plasma potential is relatively flat and is

typical of high-density low-pressure processing plasmas, where the bulk is quasi-neutral and the electrons are repelled near the surface by a thin sheath.

The power deposition and electron source are shown in Fig. 2.3. The power deposition is highest directly below the window where the inductively coupled field is largest. In addition, there is also capacitively coupled power deposition above the wafer and near the gas inlet ring support. Typically, the capacitive field is not used as a primary heating source in this system, but instead provides a dc self bias on the wafer which accelerates the ions as they move to the surface. The electron source is largest below the window, although it is shifted to larger radius than the peak of the power deposition. This phenomenon can occur in low-pressure systems where the mean free path for electrons is large so that the electrons which are heated in one region can move to another region before undergoing an inelastic collision. The electron source is lowest in the center of the plasma, since the heating source is primarily on the edges of the plasma due to the small skin depth of a high-density plasma.

The flow pattern at an instant in time is shown in Fig. 2.4. A flow rate of 100 sccm is relatively high for a pressure of 10 mTorr. One consequence is that for the time where the flow pattern is shown, wave behavior is seen in the flow, due to the compressibility of the gas. In addition to this, the overall flow pattern is seen to go from the inlet nozzle below the quartz window to the pump port at the outer radius.

In addition to the information shown here, other two-dimensional information can be seen, such as source rates for all electron-impact reactions, electron-collision frequency and temperature, and density and fluxes for all chemical species being tracked. Fluxes and sheath information to the wafer surface is also given in one-dimensional format as a function of position.

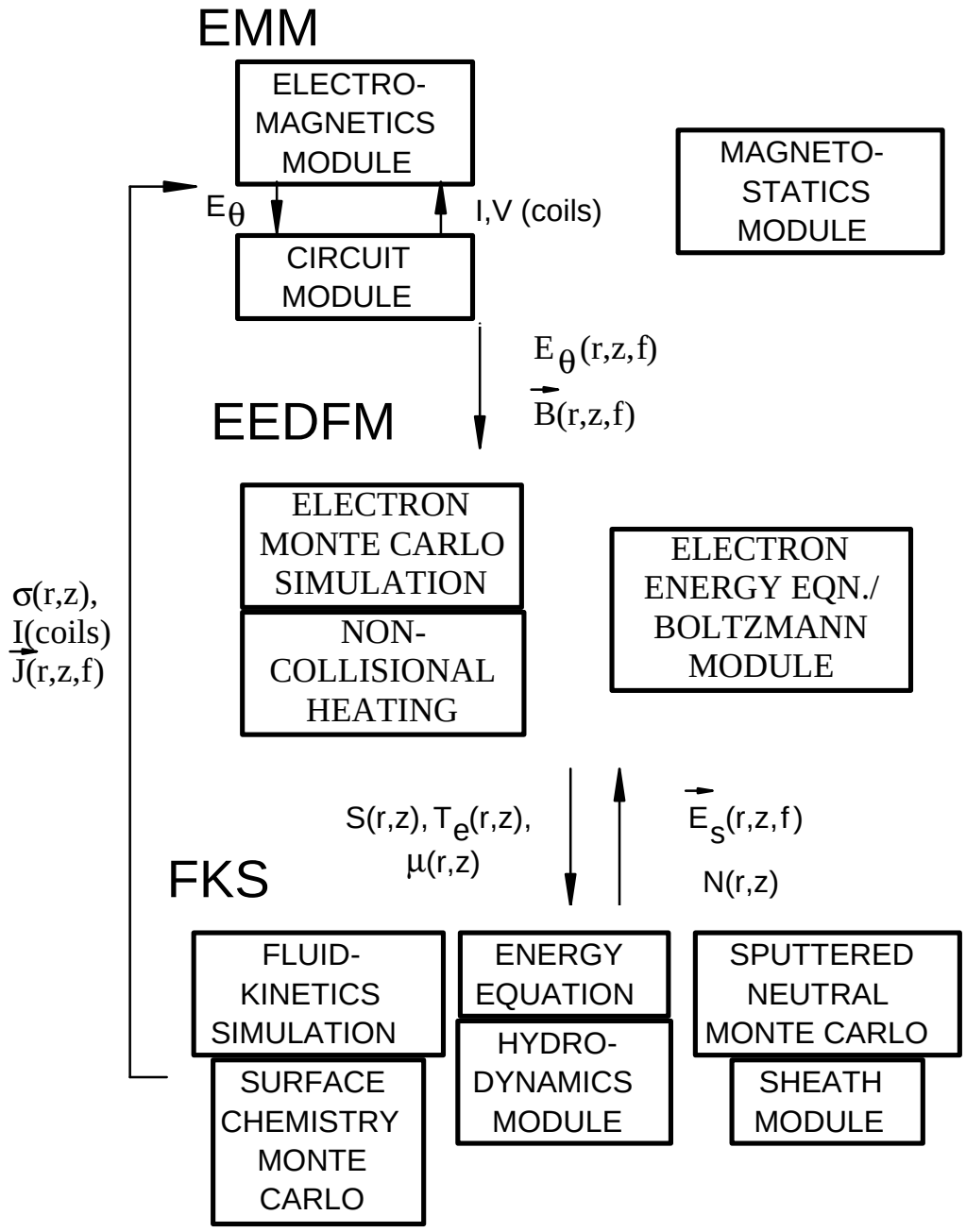

Fig. 2.1. Organization of the HPEM. The HPEM consists of three main modules: the electromagnetics module, the electron-energy distribution function module, and the fluid-kinetics simulation. Information is transferred between modules and each is solved successively until convergence is reached. Within each module are several physics modules which can be selected to represent the needed physics for a given reactor.

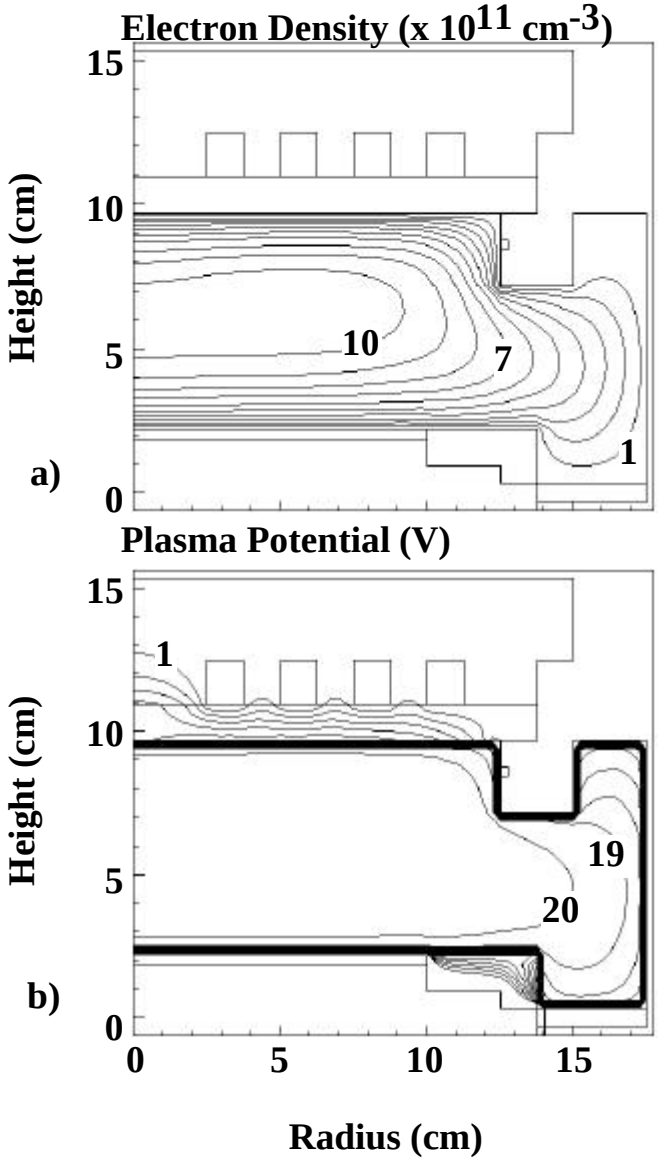

Fig. 2.2. Electron density and plasma potential in an ICP reactor. The electron density and plasma potential are relatively uniform over the wafer surface.

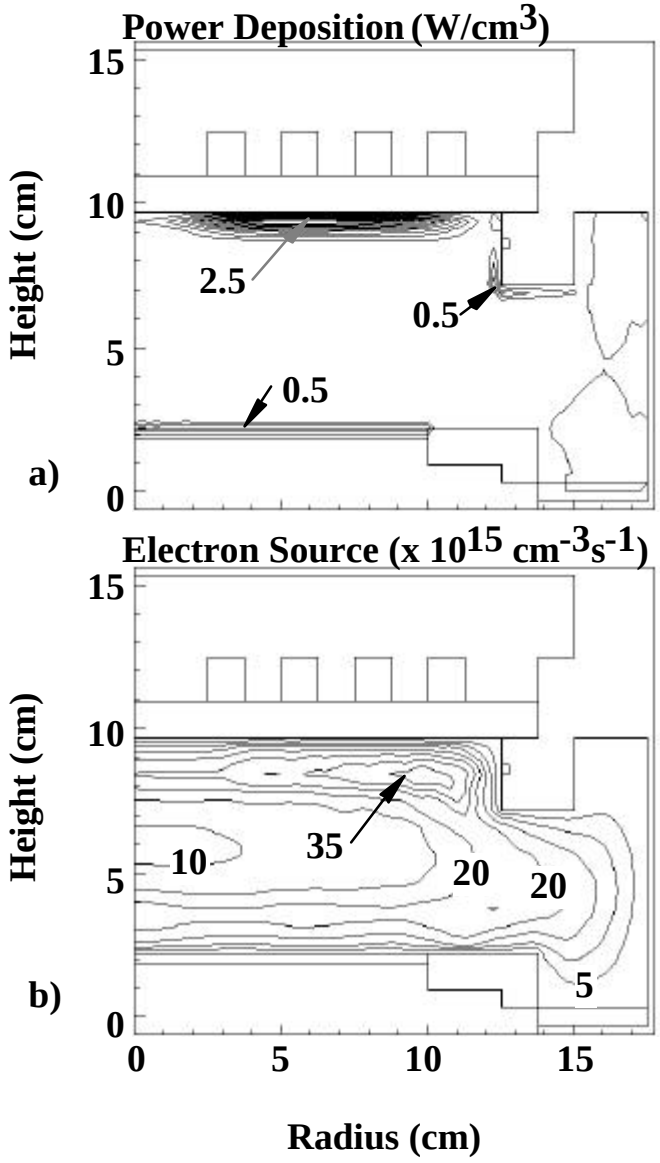

Fig. 2.3. Power deposition and the electron source in an ICP reactor. The power deposition occurs primarily below the window, with capacitive heating above the wafer and near the gas inlet ring. The electron source is also peaked below the window, but shifted to larger radius and has a minimum in the center of the plasma.

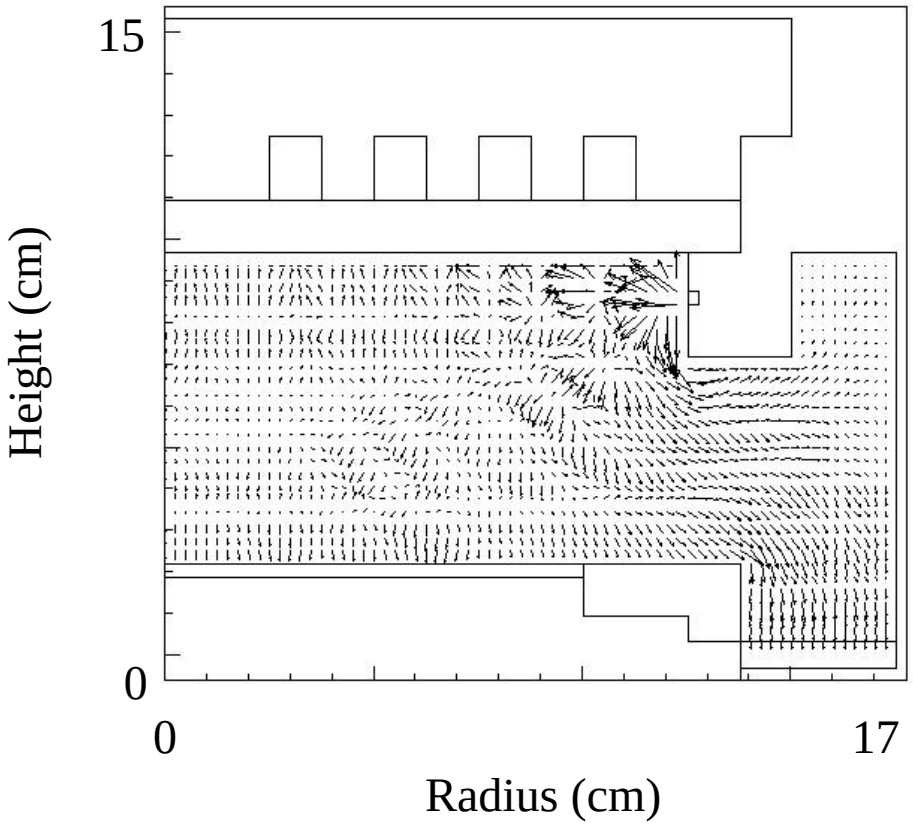

Fig. 2.4. Flow in an ICP reactor at a moment in time. Flow proceeds from the gas inlet nozzle to the pump port at the outer radius. The high flow rate causes wave behavior to develop in the plasma region.

2.6. References

[1] T. J. Sommerer and M. J. Kushner, *J. Vac. Sci. Tecnol. A*, vol. 71, p. 1654, 1992.

[2] P. L. G. Ventzek, T. J. Sommerer, R. J. Hoekstra and M. J. Kushner, *Appl. Phys. Lett.*, vol. 63, p. 605, 1993.

[3] P. L. G. Ventzek, R. J. Hoekstra and M. J. Kushner, *J. Vac. Sci. Technol. B*, vol. 12, p. 461, 1993.

[4] P. L. G. Ventzek, M. Grapperhaus and M. J. Kushner, *J. Vac. Sci. Tecnol. B*, vol. 16, p. 3118, 1994

[5] W. Z. Collison and M. J. Kushner,. *Appl. Phys. Lett.*, vol. 68, p. 903, 1996.

[6] M. J. Kushner, W. Z. Collison, M. J. Grapperhaus, J. P. Holland and M. S. Barnes, *J. Appl. Phys.*, vol. 80, p. 1337, 1996.

[7] M. J. Grapperhaus and M. J. Kushner, *J. Appl. Phys.*, vol. 81, p. 569, 1997.

[8] S. Rauf and M. J. Kushner, *J. Appl. Phys.*, vol. 81, p. 5966, 1997.

3. THE PLASMA SHEATH MODEL

3.1. Introduction

Near the boundaries in a plasma, charge separation occurs on scales which are on the order of the Debye length. This means that grid sizes used in the bulk of the plasma, typically a few mm, cannot resolve the behavior near the walls. To accurately represent the boundary conditions, a model which represents the small scales in the sheath region is needed. A sheath model (SM) has been developed which is integrated within the HPEM. In Section 3.2, the SM and its integration into the HPEM is described. In Section 3.3, validation of the dc portion of the sheath model is discussed. Plasma properties obtained with and without the SM will be compared and described in Section 3.4. Plasmas will be examined having inductively coupled powers from 200 to 800 W and rf bias powers from 50 to 400 W for Ar and Ar/Cl_2 gas mixtures. It was found that the sheath voltage wave form remained nearly sinusoidal and that the plasma density, and consequently the ion flux to the surface, scaled primarily with inductively coupled power.

3.2. Description of the Model

The SM is implemented in the HPEM in the following manner. The plasma properties in the last computational plasma cell adjacent to a wall in the reactor are schematically shown in Fig. 3.1. Particle densities and potentials are solved for at the vertice points (and on surfaces) denoted by $k \pm \ell$, where k is the mesh point on the surface of the wall. Quantities at the sheath edge are denoted by a subscript "o" and quantities at the surface of the wall are denoted by a subscript "s." The sheath is assumed to be one-dimensional with a thickness l smaller than the grid resolution defined by the cell width Dx. Using a finite difference approximation, the electric field above the sheath E_0 is given by

$$E_0 = -\frac{V_0 - V_{k-1}}{\Delta x} \tag{3.1}$$

where V_0 is the potential at the sheath edge and V_{k-1} is the potential at the last node in the plasma. Because typically $l << Dx$, then $\Delta x - l \approx \Delta x$. The electric field at the surface E_s is then given by Gauss' law:

$$E_s = E_0 + \frac{Q}{e_0} \tag{3.2}$$

where Q is the charge density (coulombs/cm^2) contained in the sheath.

The time-rate of change of the sheath charge density Q can be obtained from the charged-particle currents into and out of the sheath:

$$\frac{dQ}{dt} = \left(j_{e_0} - j_{e_s}\right) + \sum_i \left(j_{i_0} - j_{i_s}\right) \tag{3.3}$$

where j_e is the electron current and j_i is the ion current from ion species i. In the results presented here, it is assumed that there are no negative ion species in the sheath region, since for our conditions, negative ions are well isolated from the sheath nearer the center of the plasma where the plasma potential is most positive.[1] The model will, however, handle negative particles should they penetrate the sheath, as long as their contribution to the space charge within the sheath is negligible. It is also assumed that $j_{i_0} \approx j_{i_s}$, which is a consequence of the steady-state ion continuity equation. This expression is exact when

the ions see only the time averaged potential, or when the ion transit time is much shorter than the time scales of interest, in this case the rf period. Within the sheath, the electrons are assumed to have a Boltzmann distribution:

$$\mathrm{n_e}(x) = n_{e_0} \exp\left(\frac{q(\mathrm{V}(x) - V_0)}{kT_e}\right) \tag{3.4}$$

where k is Boltzmann's constant, T_e is the electron temperature and V(x) is the local potential. The electron current reaching the surface is

$$j_{e_s} = j_{e_0} \exp\left(\frac{q\Delta V}{kT_e}\right) \tag{3.5}$$

where $\Delta V = V_s - V_0$ is the voltage drop across the sheath. The electron temperature in the sheath is assumed to be the same as at the sheath edge, and is provided by the HPEM. At each location along the wall, E_0, n_{e_0}, j_{e_0}, and j_{i_0}, are also provided by the HPEM.

The sheath charge density Q can now be tracked as a function of time, provided that the sheath-voltage drop can be related to the plasma properties and Q. This is the point where the one-dimensional model of the sheath is incorporated into the equipment model. Any model which properly represents the physics of the sheath and can relate the defined plasma properties and Q to the voltage drop can now be applied. The model used here is based on the unified sheath model of Riley.[2] The inclusion of multiple ion species is an extension.

The ions are assumed to move in a damped potential $\overline{\mathrm{V}}$. The ion continuity and energy equations are then used to determine the ion density in the sheath:

$$\mathrm{n_i}(x) = n_{i_0}\left(1 - \frac{2q\,\overline{\mathrm{V}}(x)}{M_i u_{i_0}^2}\right)^{-\frac{1}{2}} \tag{3.6}$$

where u_{i_0} is the larger of either the Bohm speed or the ion speed leaving the last plasma cell in the HPEM. The damped potential $\overline{\mathrm{V}}$ is computed from

$$\frac{d\,\overline{\mathrm{V}}}{dt} = \frac{\mathrm{V} - \overline{\mathrm{V}}}{t_r} \tag{3.7}$$

where t_r is the ion relaxation time, approximated by the sheath thickness, divided by the density-averaged ion velocity entering the sheath. This formulation may slightly underestimate the transit time but is a reasonable approximation.

Using the charged species distributions (Eqs. (3.4) and (3.6)), Poisson's equation,

$$\frac{d\,\mathrm{E}}{dx} = \frac{q}{e_0}\left(\sum_i \mathrm{n_i} - \mathrm{n_e}\right) \tag{3.8}$$

is integrated across the sheath to yield the sheath voltage drop. In order to analytically integrate this equation, a relationship between the damped potential and the instantaneous potential must be known. Following the unified sheath model of Riley, the damped potential is assumed to have the same spatial distribution as the instantaneous voltage so that

$$\overline{\mathrm{V}}(x,t) \approx \mathrm{f}(t)\,\mathrm{V}(x,t)\,. \tag{3.9}$$

The final expression for the first integral of the Poisson equation is then given by

$$\frac{1}{2}\left(E_s^2 - E_0^2\right) = \frac{1}{e_0}\left\{\sum_i n_{i_0} M_i u_{i_0}^2 \left(\frac{\Delta V}{\Delta \overline{V}}\right)\left[\left(1 - \frac{2q\Delta\overline{V}}{M_i u_{i_0}^2}\right)^{\frac{1}{2}} - 1\right] + n_{e_0} kT_e \left[\exp\left(\frac{q\Delta V}{kT_e}\right) - 1\right]\right\} \tag{3.10}$$

Recall that E_s is related to E_0 and Q by Eq. (3.2). Therefore, Eqs. (3.2) and (3.10) provide implicit relations between the sheath charge, the plasma properties and the voltage drop, which are solved by numerical iteration.

The sheath-voltage drop is obtained at each wall location and at each time step during an rf cycle in the HPEM. The sheath properties are communicated back to the FKS by using ΔV as a jump condition in solving Poisson's equation. This is accomplished by assuming that the sheath thickness is much smaller than the grid spacing. In this case, by examining Fig. 3.1, the finite difference form of Poisson's equation at the last node above the sheath is

$$\frac{1}{\Delta x}\left[\left(\frac{V_0 - V_{k-1}}{\Delta x}\right) - \left(\frac{V_{k-1} - V_{k-2}}{\Delta x}\right)\right] = -\frac{r_{k-1}}{e_0}\,. \tag{3.11}$$

Recalling that $V_0 = V_s - \Delta V$ yields a modified finite-difference form for Poisson's equation:

$$\frac{1}{\Delta x}\left[\left(\frac{V_s - V_{k-1}}{\Delta x}\right) - \left(\frac{V_{k-1} - V_{k-2}}{\Delta x}\right)\right] = -\frac{r_{k-1}}{e_0} + \frac{\Delta V}{(\Delta x)^2}. \qquad (3.12)$$

If the wall is a conductor, then V_S is specified as a boundary condition. If the wall is a dielectric, then, using Eq. (3.2), the finite difference form of Poisson's equation at the wall is

$$\frac{1}{\Delta x}\left[e_r\left(\frac{V_1 - V_s}{\Delta x}\right) - \left(\frac{V_s - V_{k-1}}{\Delta x}\right)\right] = -\frac{r_s}{e_0} - \frac{Q}{e_0 \Delta x} - \frac{\Delta V}{(\Delta x)^2} \qquad (3.13)$$

In this way, Poisson's equation is solved in the same manner as when the analytic sheath is not used, except that the additional terms on the RHS of Eqs. (3.12) - (3.13) are required in the last plasma cell and on dielectric walls respectively.

In plasma models in which the sheath is not resolved, its effective thickness is at best the width of one numerical cell. The sheath will oscillate through this thickness during an rf cycle, which exaggerates its average speed by as much as the ratio $\Delta x/l$. This exaggeration may cause artificially large stochastic heating of electrons since that heating rate is proportional to the sheath velocity. In the HPEM, the electron-energy distribution is obtained in the EMCS, which uses the time and spatially dependent electromagnetic fields (from the EMM) and electrostatic fields (from the FKS) to advance electron trajectories. To properly account for electron heating at the rf sheath, the results of the SM must be incorporated into the EMCS. This is accomplished in the following manner.

In the EMCS the sheath is also treated as being thin so that the transit time of the electrons across the sheath will be shorter than the time scale on which the sheath potential changes. The sheath thickness at a given time is approximated by the

instantaneous sheath charge Q divided by the ion charge density at the sheath edge. This approximation will tend to underestimate the sheath thickness slightly, but is employed for practical purposes, since a numerical integration of the sheath charge distribution across the sheath at each surface point and at each time step would be too costly. An electron which reaches the sheath is checked to see if it has a sufficiently large perpendicular component of velocity towards the wall to overcome the sheath potential and reach the wall. If so, the electron is collected. Electrons which cannot overcome the sheath potential are reflected. In these cases, the electron velocity perpendicular to the wall is incremented by the sheath velocity. The sheath velocity is computed by a finite difference of the sheath thickness with respect to time, so that when the sheath is expanding, electrons leave with greater energy, and when the sheath is collapsing, electrons leave with less energy. In this manner stochastic electron heating by the rf sheath is properly taken into account.

3.3. Validation

Before applying the SM to rf-biased reactors, the dc characteristics of the SM were validated by comparing computed results for plasma potential, ion density and electron temperature with electric probe measurements performed by Miller et al.[3] The measurements were made in the Inductively Coupled-Gaseous Electronics Conference Reference Cell (IC-GECRC) for plasmas sustained in argon. A schematic of the IC-GECRC reactor geometry is shown in Fig. 3.2 and contains of a five turn spiral coil above a quartz window. The experimental technique and the IC-GECRC are described in detail in Ref. 3. Comparisons to experiments were performed at a pressure of 10 mTorr and power deposition up to 250 W.

The center line electron density, peak plasma potential and electron temperature are shown in Fig. 3.3 as a function of power deposition with and without using the sheath

model in the HPEM. The electron density, with and without the SM, and the reactor configuration, are shown in Fig. 3.4. In general, the cases using the SM agree better with the experiments. The plasma potential is both more positive and flatter as a function of axial position when using the SM. This result is an electron density which peaks on the centerline as observed experimentally. In many cases the predicted plasma density without using the SM peaks off axis where the electron source function is the highest (see Fig. 3.4.). This trend was also observed in the cases with an applied rf bias and will be discussed in the next section. The electron temperature without the SM is somewhat higher than with the SM due to the lower plasma potential. This results in larger electron losses, which requires a higher electron temperature (and electron source) to balance.

3.4. Sheath Properties in ICP Etching Reactors

The demonstration geometry is the generic LAM TCP geometry described in Chapter 1 and shown in Fig. 1.1. This geometry is described in more detail in Collison and Kushner.[4] The ICP reactor uses a flat spiral 4-turn coil set on top of a quartz window. The wafer-to-window distance is 7.5 cm. The wafer diameter is 20 cm and is surrounded by an alumina focus ring. The wafer is treated as a uniform disk with a conductivity of 0.05 $(\Omega\text{–cm})^{-1}$. The coils are driven at 13.56 MHz. The gas is Ar at 10 mTorr with an inlet flow rate of 100 sccm. The coils deliver 400 W of inductively coupled power to the plasma. The wafer is biased at 13.56 MHz with 200 W of power deposition (32 V bias voltage amplitude).

To demonstrate the effect of the SM on plasma parameters when using rf biases, cases were also run without the SM having the same bias power, and without the SM having the same applied voltage. The electron densities for these cases and for the standard case are shown in Fig. 3.5. The ionization is maximum in a torus at approximately half the radius located a few cm below the dielectric window.[5] It is in this

region that the power deposition is maximum due to the finite skin depth of the inductively coupled electric field into the plasma. The electrons produced in this region diffuse under ambipolar forces to the walls. The electron density for the case without the SM but with the same bias voltage on the substrate (Fig. 3.5(a)) has a profile which is sharply peaked near the source region with a maximum value of 4.6×10^{11} cm^{-3}. The plasma potential is also peaked off axis. When using the SM (Fig. 3.5(b)), a larger fraction of the ambipolar potential is dropped across the sheath as compared to the bulk. As a result, the plasma potential is flatter in the bulk. The rate of loss of electrons to the wall and through the sheath from a mean-free path away is reduced because the sheath potential is higher. The electron density with the SM has a maximum value of 1.1×10^{12} cm^{-3}, both higher and more uniform than in the absence of the sheath model, due to the redistributed plasma potential. The general experimental observation for these conditions is that there is not a large off axis maximum in electron density. These same trends were observed in the simulations of IC-GECRC discussed in Section 3.3. The SM therefore appears to provide boundary conditions in the FKS which generate more physical solutions. The case without the SM, but with the same rf bias power as with the SM (Fig. 3.5(c)), has the same peak electron density as the case without the SM and with the same bias power. The bias voltage for this case is somewhat larger (124 V) to obtain the same bias power as the case with the SM because the ion flux to the wafer is smaller. As a result, the electron density is somewhat more uniform. For these conditions I have empirically found that plasma uniformity improves with increasing bias voltage.

The cycle-averaged plasma potential as a function of height at r = 0 is shown in Fig. 3.6 for the same conditions as in Fig. 3.5. Examining the cases with and without the SM and which have the same applied bias voltage, it is seen that the total voltage drop between the bulk plasma and the powered electrode is nearly the same, 23-25 V. This correspondence is a consequence of the fact that the ion and electron currents to the

surface must be equal because the wafer has a low conductivity and it is capacitively coupled to the power source. The dc bias, however, is smaller (less negative) for the case with the SM. This is a direct consequence of the plasma density being larger with the SM. It has been experimentally observed that for the same bias rf voltage amplitude, the dc bias decreases (becomes less negative) with increasing coil power and plasma density. These trends are discussed in more detail in Ventzek et al.[5] Comparing the cases with and without the sheath model at the same deposited power is more difficult, because a larger applied voltage (124 V) is required to obtain the same bias power without the SM. This results from the fact that the ion flux is higher when the SM is used, and therefore a smaller applied bias voltage is required to obtain the same power deposition. The larger rf bias voltage produces a larger (more negative) dc bias.

The cycle-averaged ion flux to the wafer, the cycle-averaged and peak sheath voltage, and the ion-power density as a function of radius across the wafer are shown in Fig. 3.7 for the conditions of Fig. 3.5 with the SM. For this reactor configuration, the sheath voltage is fairly uniform across the wafer with a time-averaged value of 19 V and a peak value of about 34 V. The ion flux is also fairly uniform, although it is 10% larger near the center of the wafer, 6.4×10^{16} cm^{-2} s^{-1} compared to 5.8×10^{16} cm^{-2} s^{-1} at the outer edge. The ion-power density to the surface follows the ion flux ranging between 0.31 and 0.34 W/cm^2. Ions gain energy crossing the sheath potential, which is relatively uniform as a function of radius. The radial dependence of the ion power flux to the wafer will therefore simply follow with radial dependence of the ion flux. This is the desired mode of operation.

The sheath voltage and sheath thickness above the wafer at the half radius location are shown in Fig. 3.8 as a function of rf phase for the conditions of Fig. 3.7. The sheath voltage is defined with respect to the plasma potential, and is therefore negative. As the applied voltage becomes more positive, the plasma potential increases, and therefore the

sheath potential at unbiased surfaces increases to maintain the electropositive nature of the plasma. This forces electrons toward the powered electrode, reducing *Q* in the sheath, which in turn reduces the magnitude of the sheath potential on the powered electrode. As the applied voltage decreases, the plasma potential decreases. Since it must also float above the grounded electrode, the electrons are forced away from the powered electrode, increasing both *Q* and the magnitude of the sheath potential above the wafer. Since only moderate voltages are applied, in this case an amplitude of 32 V rf, the sheath voltage remains nearly sinusoidal, and is nearly in phase with the driving voltage. The sheath voltage lags the applied voltage by approximately 45° due to the large capacitance of the sheath. The sheath thickness ranges from a minimum of 20 μm to a maximum of 57 *m*m and for the most part follows the magnitude of the sheath voltage. Its deviation from sinusoidal results from modulation of the charged-particle densities at the edge of the sheath during the rf phase.

One of the important motivations for using an inductively coupled plasma source with substrate biasing is to be able to separately control the magnitude, uniformity and energy of the ion flux to the wafer. The peak flux to the wafer and the uniformity across the wafer for a variety of operating conditions in Argon are shown in Fig. 3.9. The non-uniformity in the ion flux is defined as $(Max - Min)/\frac{1}{2}(Max + Min) \times 100$ %. With 400 W of ICP power, the magnitude of the ion flux to the surface does not vary greatly as the rf bias power is increased by increasing the bias voltage (Fig. 3.9(a)). The ion flux remains near 6×10^{16} cm^{-2} s^{-1}. The nonuniformity decreases from 20% to 3% when increasing the substrate power and rf bias voltage. I have found that larger rf biases produce more uniform ion fluxes when bias power becomes comparable with ICP power and the discharge begins to look like a capacitive discharge. For moderate rf-bias power, the nonuniformity is relatively insensitive to the rf-bias power.[6] The small increase in average ion flux obtained when applying the bias is more a consequence of the improved

uniformity than an absolute increase in flux. The effects of varying ICP power on ion flux and nonuniformity are shown in Fig. 3.9(b). The results are somewhat different depending upon whether the bias voltage or power is held constant. The uniformity improves with increasing ICP power when the voltage is held fixed, due in part to the fact that as plasma density increases as well as the fact that the bias power increases and remains comparable to the ICP power. This leads to an increase in the capacitively coupled power. A more interesting result is obtained when the capacitively coupled power deposition is held constant while the inductive power deposition is increased. In this case, the applied rf-bias voltage required to obtain the same bias power decreases, which can cause a decrease in uniformity.

The sheath model can also be applied to plasmas having multiple ion species. As an illustration, the model was run for an Ar/Cl_2 plasma with an inlet flow rate of 50 sccm for each gas. The inductively coupled power deposition was 200 W, and a 100 V rf was applied to the substrate. The electron density for this case is shown in Fig. 3.10 and has a peak plasma density of 4.6×10^{11} cm^{-3}. The Ar/Cl_2 plasma is peaked off-axis, where the electron source is located, and is less uniform than the pure Ar case due to the increased collisionality of the gas mixture and the large Cl^- density.

Shown in Fig. 3.11 are the sheath thickness and voltage as a function of rf phase for the Ar/Cl_2 case. The results are qualitatively the same as for the Ar-only case (Fig. 3.8). For similar operating conditions, electronegative gases have thinner sheaths; however, in this example the sheath is thicker due to lower plasma density and the larger sheath potential and power in the Ar/Cl_2 case. The sheath thickness is also less sinusoidal appearing somewhat more resistive compared to the Ar-only case, a consequence of perturbation of the electron flux entering the sheath produced by the presence of the negative ions.

The average ion flux to the wafer for the Ar/Cl_2 case is shown in Fig. 3.12. Results are shown for an rf bias of 100 V as a function of ICP power and for 400 W ICP power as a function of the bias voltage. With 400 W of ICP power, the magnitude of the ion flux to the surface rises slightly as the voltage is increased, reaching a value near 6×10^{16} cm^{-2} s^{-1} at larger voltages. This trend results primarily from an improvement in plasma uniformity. When the applied bias voltage is held constant, the magnitude of the ion flux increases as the ICP power increases, as expected, since the plasma density depends primarily on the inductively coupled power. From these results it is seen that the ion flux to the wafer is a function of both the rf bias and the inductively coupled power, with a stronger dependence on the latter.

3.5. Summary

Properly representing the rf sheath in models of high-plasma-density tools is important to correctly predict the plasma density and potential. In implementing a semi-analytic sheath model into a two-dimensional model for rf biased ICP reactors, it was found that predictions for the ion fluxes, power deposition and the overall electrical characteristics of the plasma were affected. For example, incorporating the SM generally results in more uniform plasmas of higher electron density. In the cases investigated for plasma properties without an rf bias, agreement with experiment was more satisfactory than without the SM. We found that the sheath potential above the wafer was generally quite uniform as a function of radius, and so the radial dependence of the ion power flux depended primarily on the ion flux. We also found that the uniformity of the ion flux to the wafer generally improved with increasing rf bias, a consequence of flattening the time-averaged plasma potential.

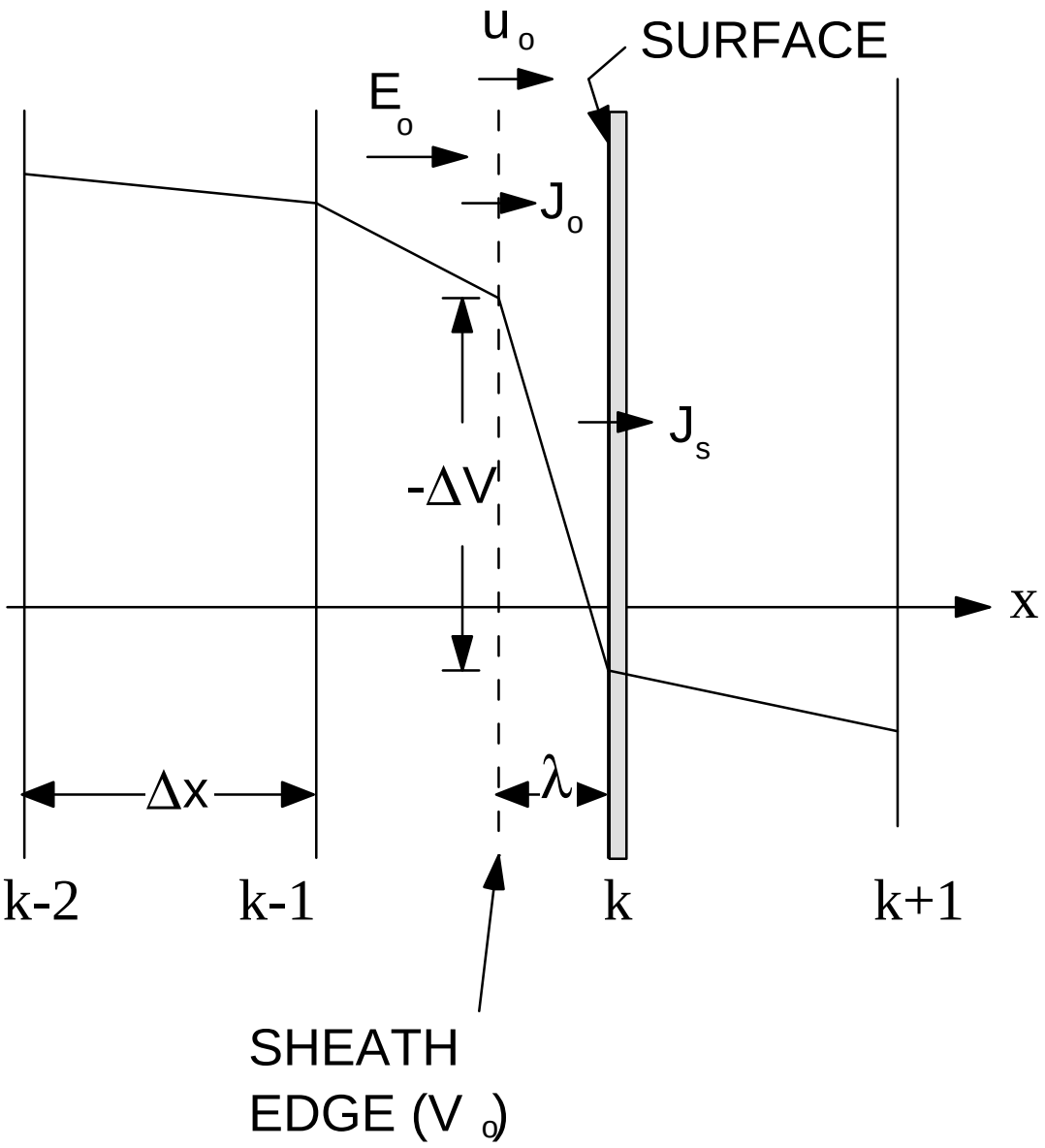

Fig. 3.1. Schematic of the sheath model geometry. Values at the sheath edge are denoted by the subscript ìoî and values at the surface of the wall by a subscript ìs.î

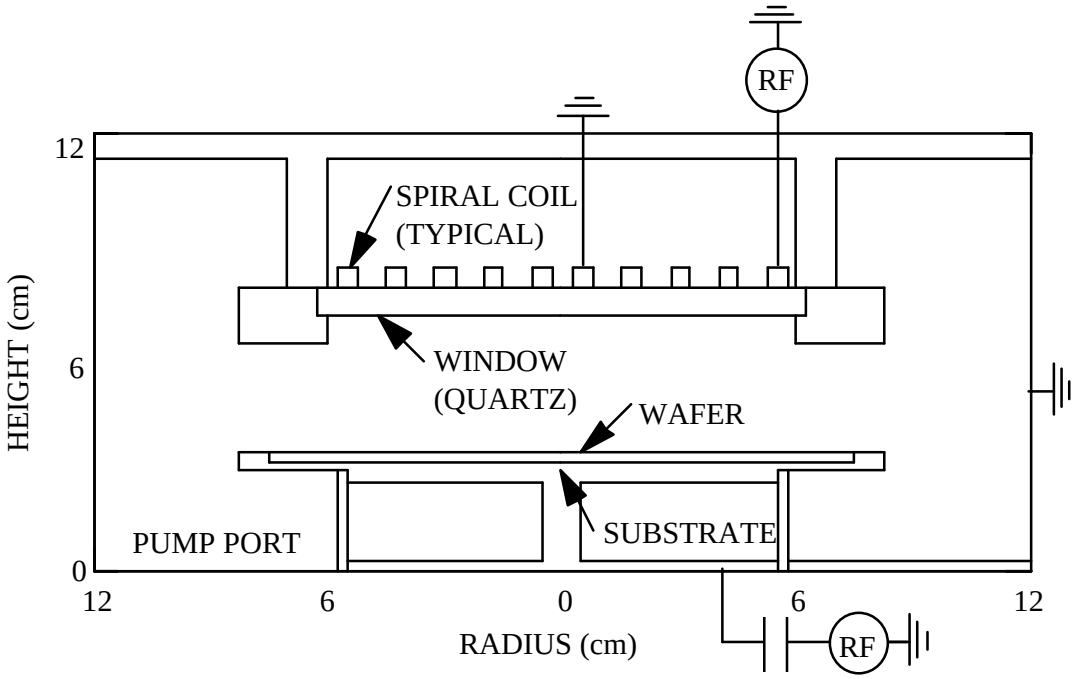

Fig. 3.2. Schematic of the IC-GECRC reactor used for comparison of the HPEM model with experimental measurements.

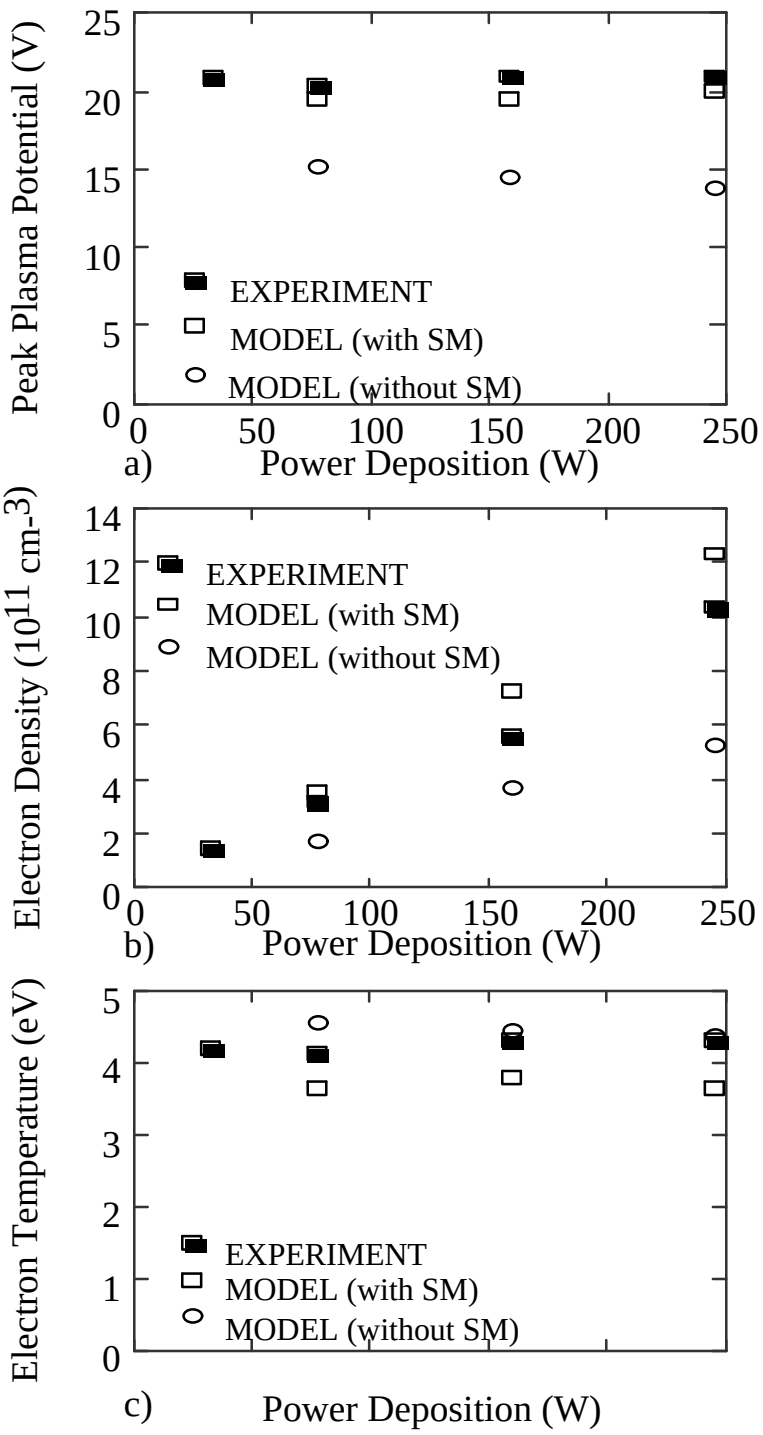

Fig. 3.3. Comparison of predicted plasma potential, electron density and temperature with experiments (see Ref. 19). The gas is 10 mTorr Ar in the IC-GECRC. In general, the model using the SM agrees better with experiments.

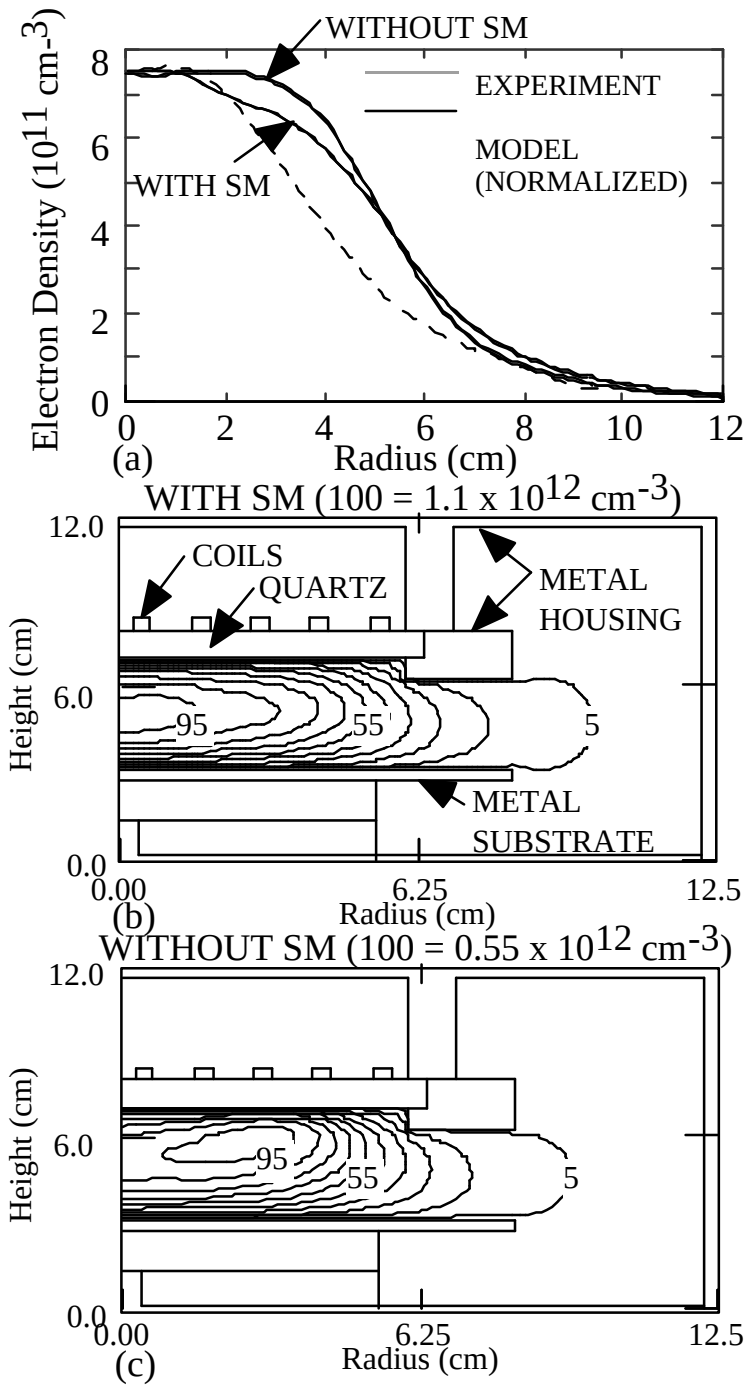

Fig. 3.4. Comparison of predicted electron density (10 mTorr Ar, 245 W) with experiments (see Ref. 19). (a) [e] as a function of radius at midplane. The model results are normalized to the experiment. (b) Predicted [e] with the SM. (c) Predicted [e] without the SM. When using the SM, the electron density peaks on axis. Contours are labeled with the percent of the maximum value shown at the top of the figure.

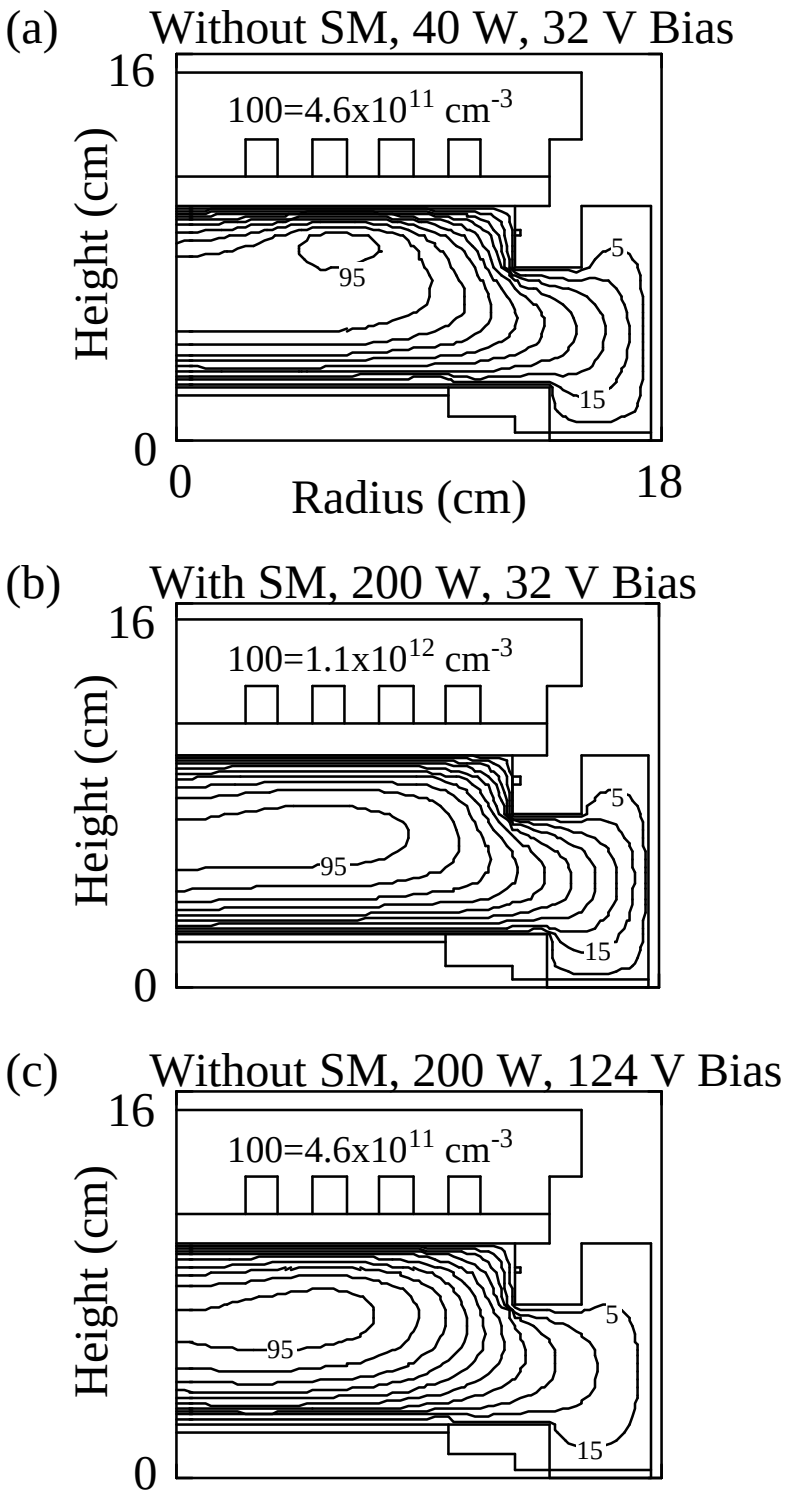

Fig. 3.5. Electron density for an inductively coupled Ar plasma at 10 mTorr and 400 W ICP power, (a) without the SM and 32 V rf bias voltage, (b) with the SM and 200 W rf bias power, and (c) without the SM and 200 W rf bias power. The contours are labeled with the percentage of the maximum value shown at the top of each figure.

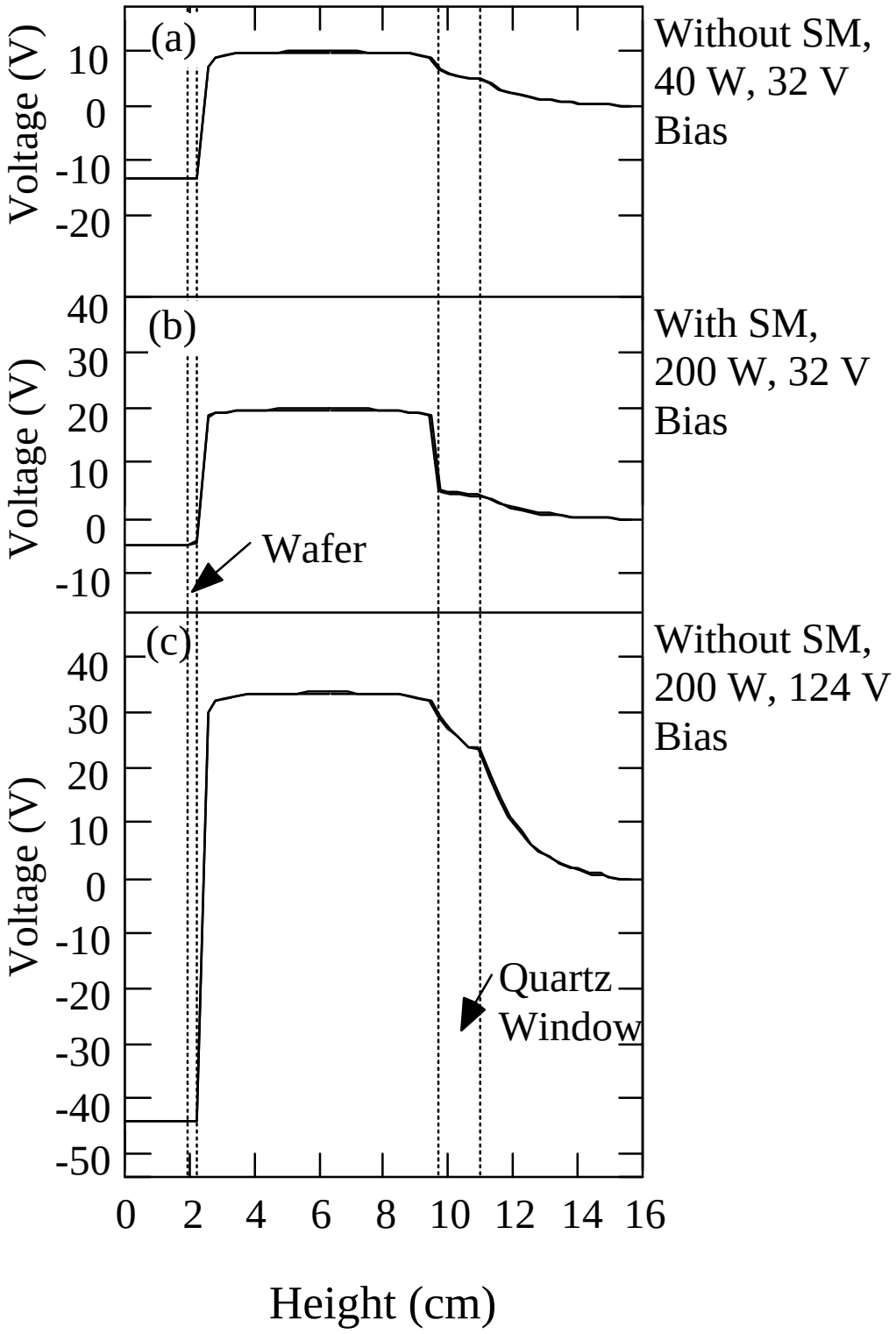

Fig. 3.6. Time-averaged electric potential at the r = 0 axis as a function of height (a) without the SM and 32 V rf-bias voltage, (b) with the SM and 200 W rf-bias power, and (c) without the SM and 200 W rf capacitive power.

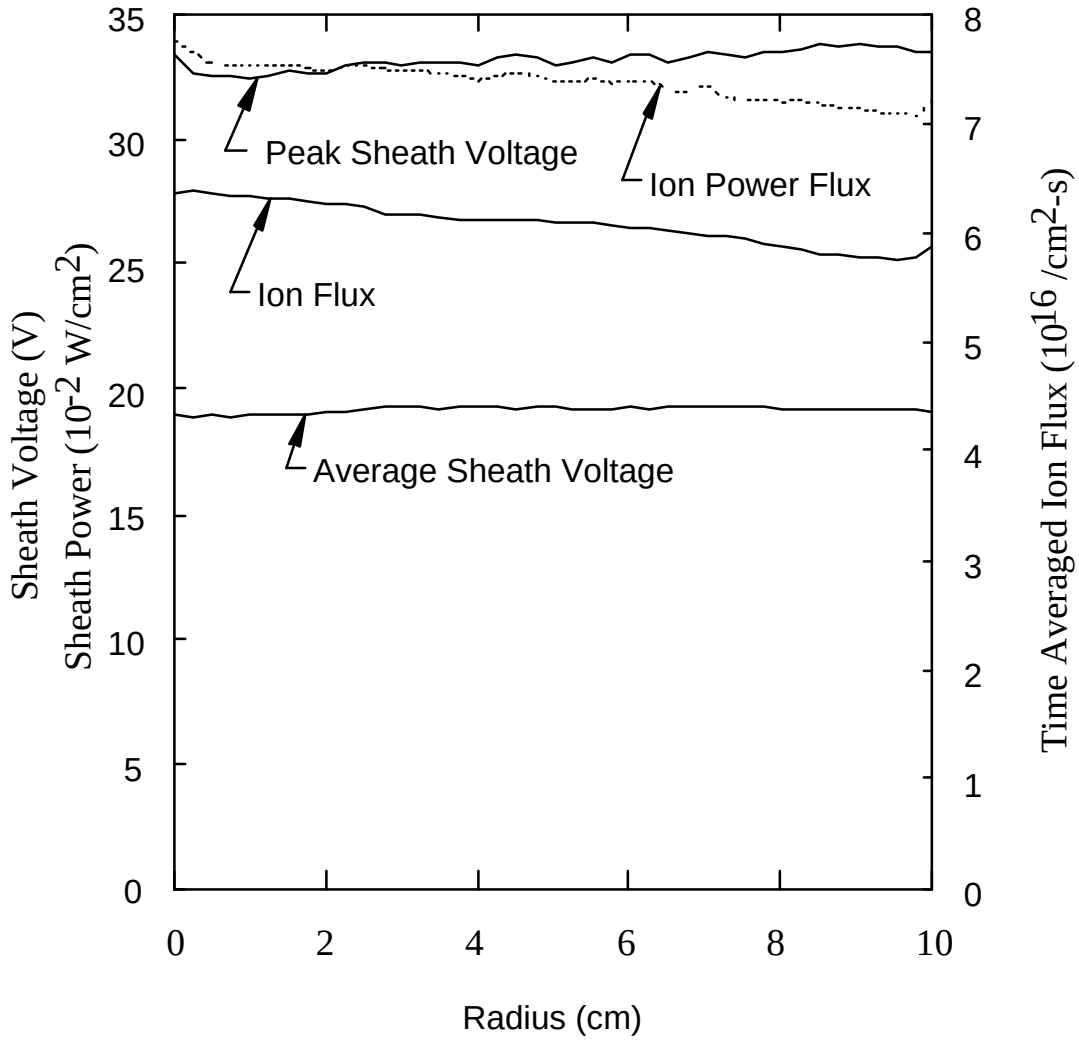

Fig. 3.7. Time averaged ion flux to the wafer, peak and time averaged magnitude of the sheath voltage, and ion power flux as a function of radius across the wafer. The sheath potential is quite uniform across the wafer. As a result, the ion power scales with the ion flux.

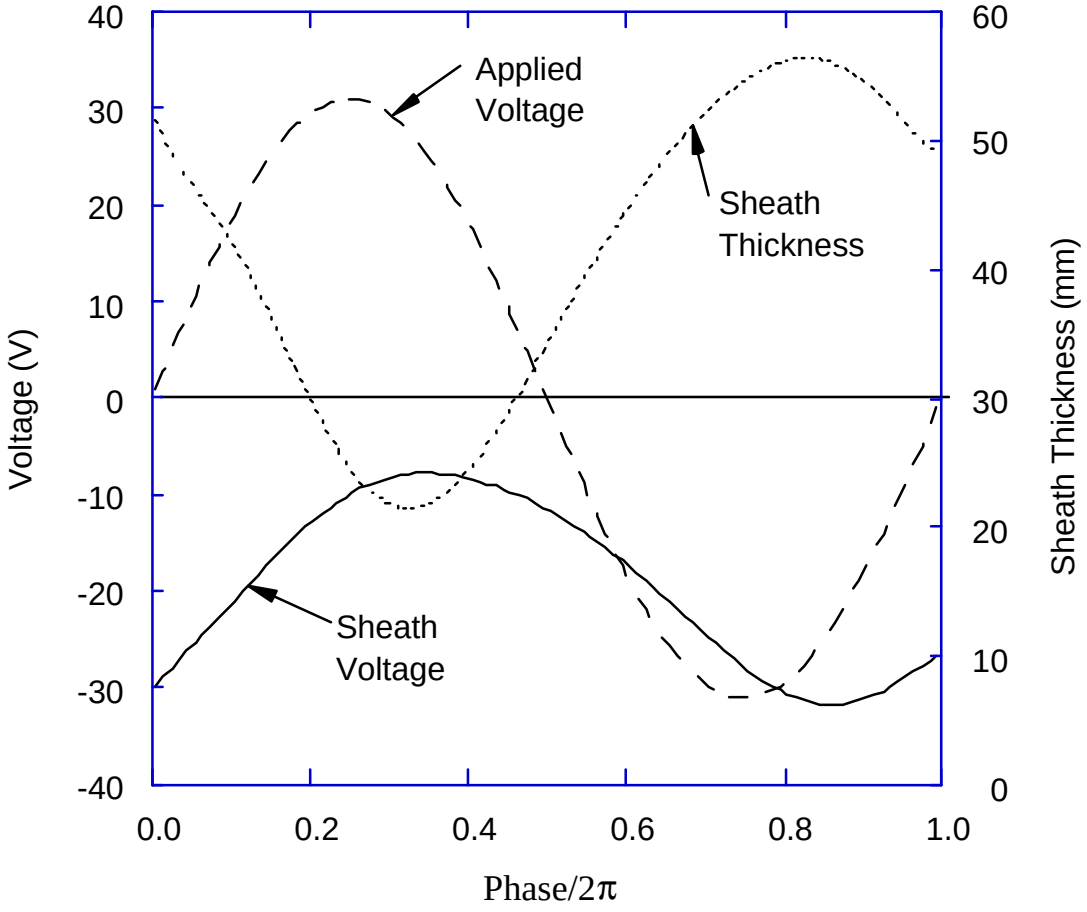

Fig. 3.8. Sheath voltage and thickness above the wafer at the half radius location (r = 5 cm) as a function of rf phase. The applied voltage waveform is included for comparison.

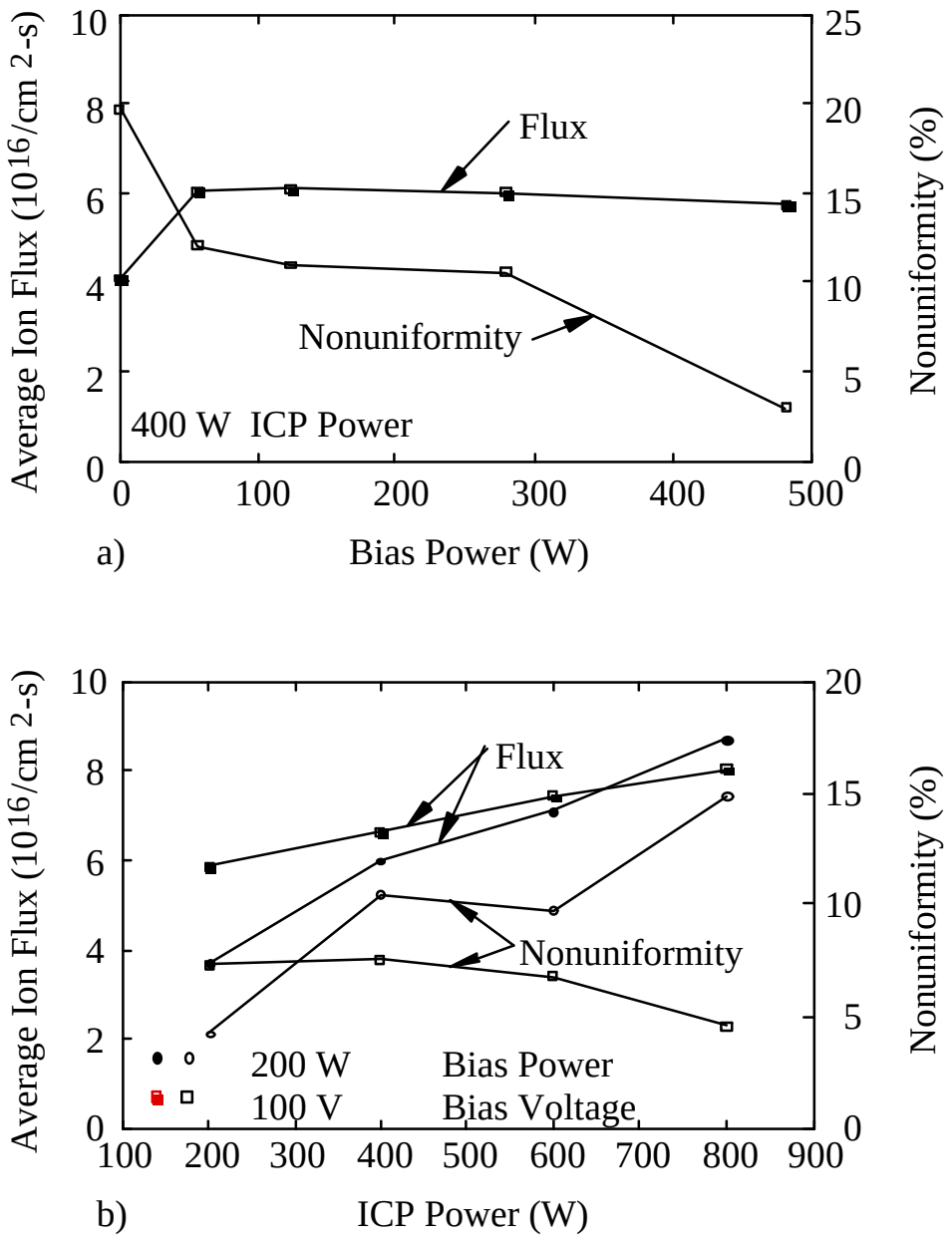

Fig. 3.9. Mean value of the time averaged ion flux to the wafer and the nonuniformity of the ion flux, defined as $(Max - Min)/\frac{1}{2}(Max + Min)$. (a) 400 W ICP power as a function of rf bias power. (b) 200 W rf capacitive power (open symbols) and 100 V rf applied voltage (solid symbols) as a function of ICP power. In general ion-flux uniformity improves with increasing bias voltage.

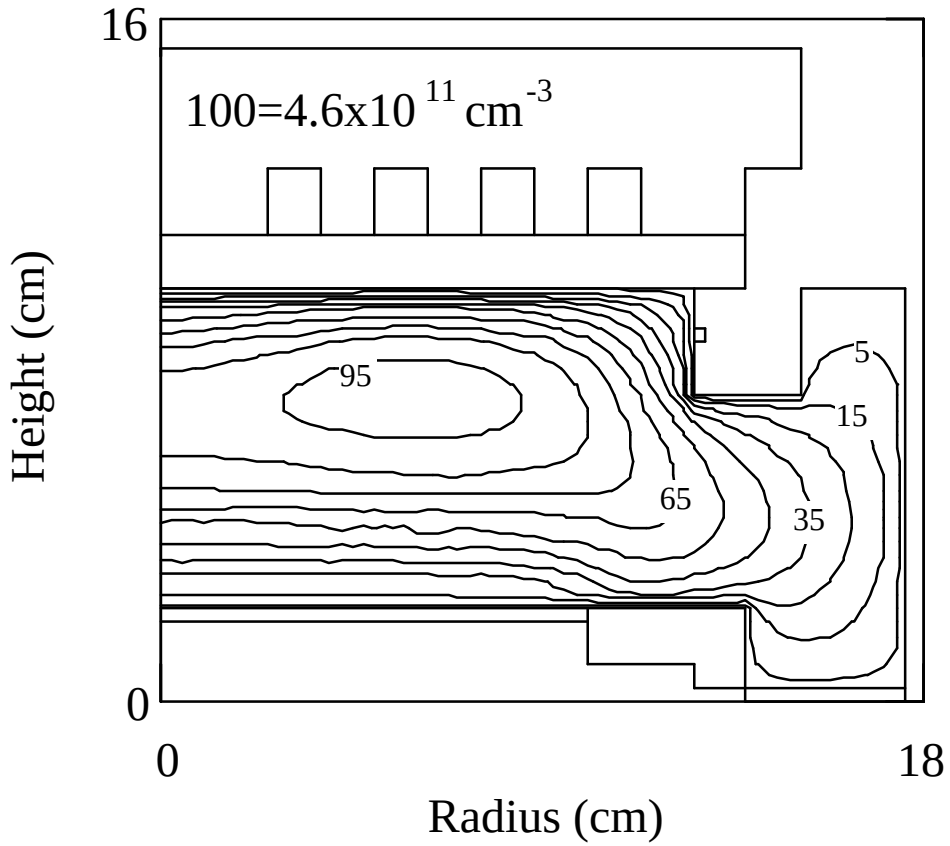

Fig. 3.10. Electron density for an Ar/Cl_2 discharge at 10 mTorr with 400 W ICP power and 100 V rf applied voltage on the substrate. The plasma is less uniform than the argon-only case due to the increased collisionality of the Ar/Cl_2 gas mixture. The contours are labeled with the percentage of the maximum value shown at the top of the figure.

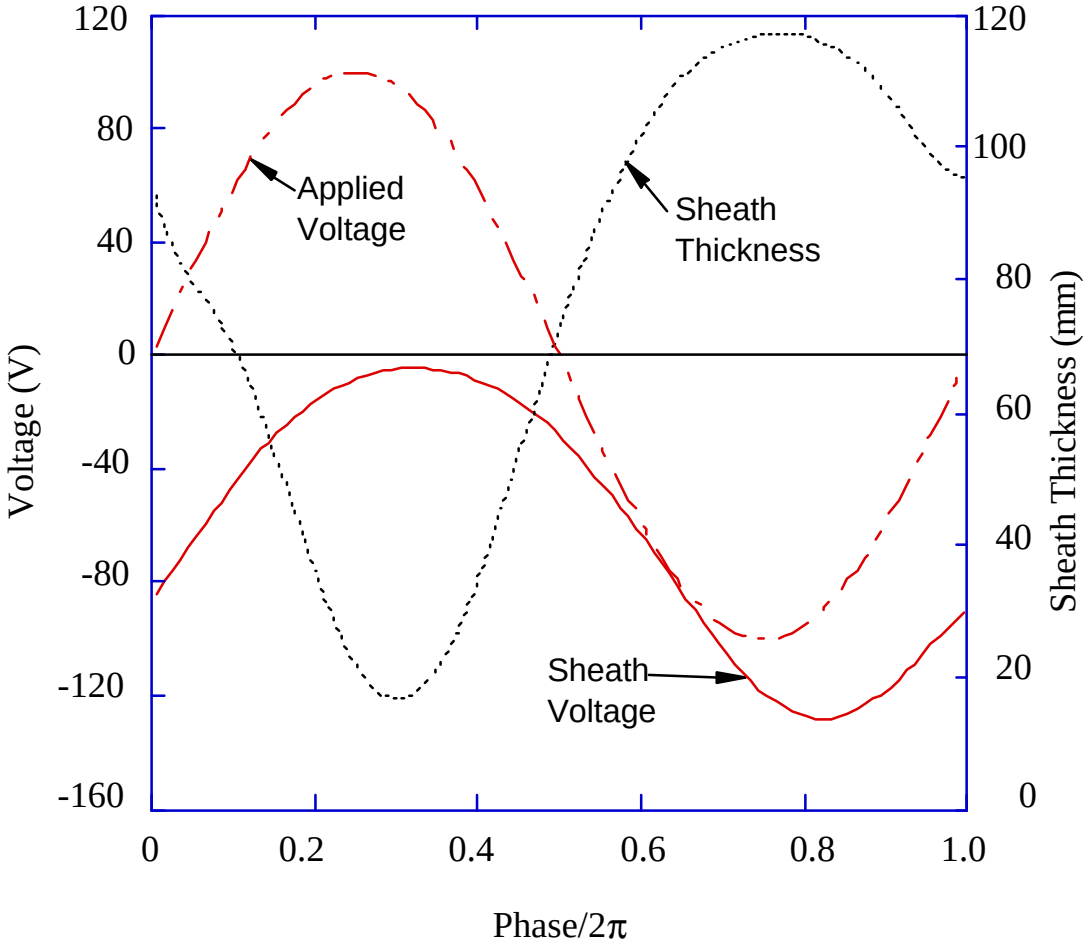

Fig. 3.11. Sheath voltage and thickness above the wafer at the half radius location (r = 5 cm) as a function of rf phase for the Ar/Cl_2 discharge. The applied voltage wave form is included for comparison. The sheath thickness is less sinusoidal compared to the argon-only case.

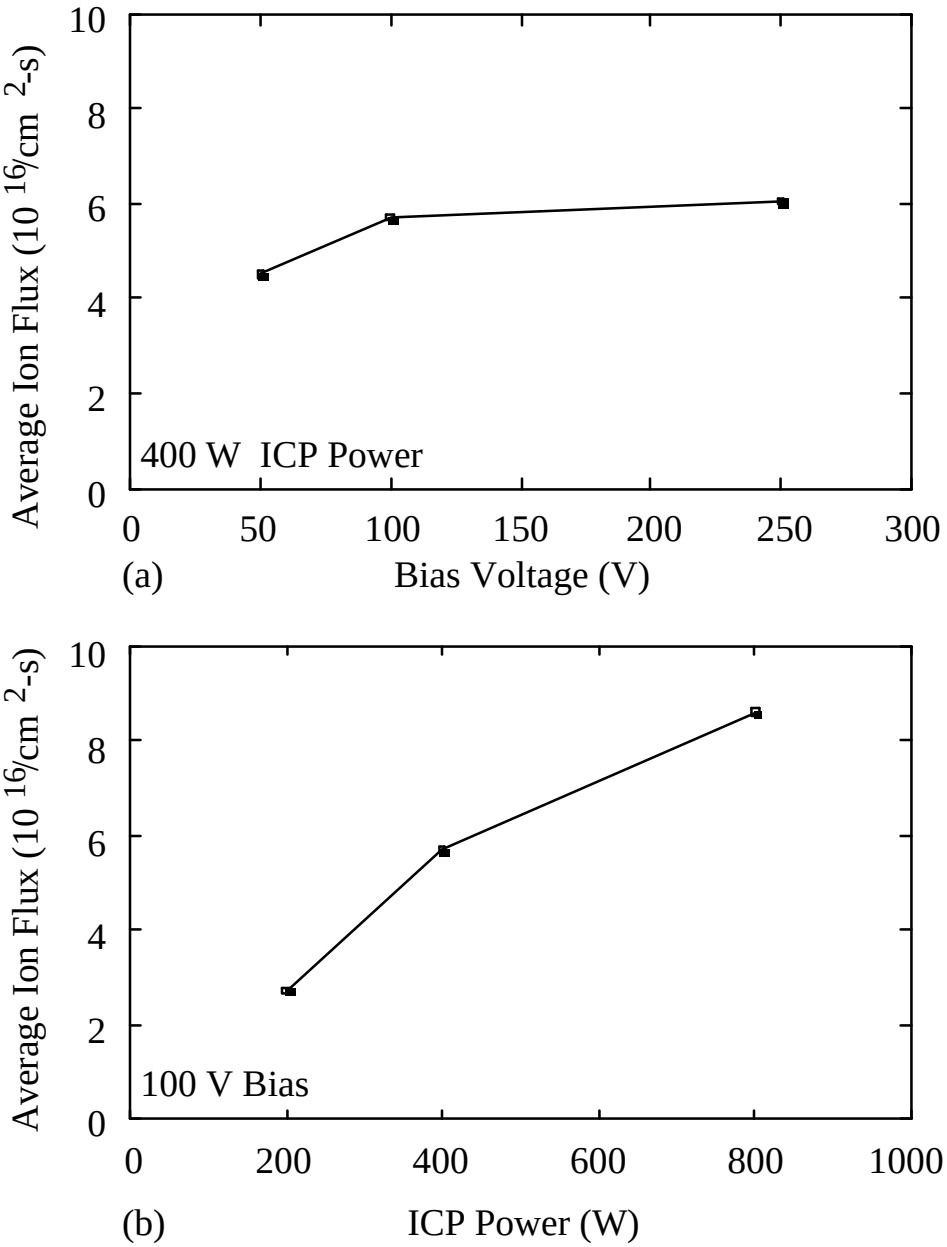

Fig. 3.12. Mean value of the time averaged ion flux to the wafer for the Ar/Cl_2 discharge for (a) 400 W ICP power as a function of bias voltage, and (b) 100 V rf bias voltage as a function of ICP power. Compare to Fig. 3.9.

3.6 References

[1] A. J. Lichtenberg V. Vahedi, and M. A. Lieberman, *J. Appl Phys.* **75**, 2339, (1994).

[2] M. E. Riley, *Sandia Report SAND95-0775.UC-401*, (1995).

[3] P. A. Miller, G. A. Hebner, K. E. Greenberg, P. D. Pochan and B. P. Aragon, *J. Res. Nat. Inst. Stds. Tech.* **100**, 427 (1995).

[4] W. Z. Collison and M. J. Kushner, *Appl. Phys. Lett.* **68**, 903, (1996).

[5] P. L. G. Ventzek, M. J. Grapperhaus and M. J. Kushner, *J. Vac. Sci. Technol.* B **12**, 3118 (1994).

[6] R. Hill, *J. Vac. Sci. Technol.* B **14**, 547 (1996).

4. IONIZED METAL DEPOSITION

4.1. Introduction

Ionized metal physical vapor deposition (IMPVD) provides a means to deposit metalization layers with an anisotropic metal flux so that high aspect-ratio features can be filed without the formation of voids. Modifications have been made to the HPEM to model IMPVD systems, including sputtering from surface, electron motion in magnetic fields, and slowing of sputtered atoms to thermal speeds in the plasma volume. The deposition rate of metal on the substrate is found to be reduced as pressure increases due to the increase in diffusive losses. It is also seen that the sputtering of the auxiliary coils can be a significant issue in IMPVD systems, which must be addressed in a realistic tool design. The model is described in Section 4.2, followed by a discussion of the results for a magnetron sputter source with an rf inductive coil post ionization reactor in Section 4.3. A summary of the work is made in Section 4.4.

4.2. Description of the Model

To address the unique conditions of IMPVD systems, improvements to the HPEM have been made for neutral-particle transport, electron transport and for defining static magnetic fields. The improvement in neutral-particle transport is the addition of a neutral atom slowing down Monte Carlo simulation (NMCS) to account for the long mean free path transport of hot atoms sputtered from the magnetron target. The improvement in electron transport included resolving electron trajectories in regions of high magnetic field and adding secondary electron emission.

In high magnetic field regions near the magnetron source (B > 1-3 kG) the cyclotron frequency is large (> 3-10 GHz). Resolving the orbits of electrons around the magnetic fields lines in the EMCS using a simple time stepping routine requires that the

time step be a small fraction of the cyclotron period. Doing so leads to unacceptably large computing time. The gyrokinetic approximation, where only the guiding center motion of the electron is followed for conditions where the Larmor radius is small compared to other dimensions, unfortunately cannot be employed here. The gradient in the magnetic field is large (10s kG/cm) and electrons transition between being highly magnetized near the sputter source to being weakly magnetized near the substrate. There is a corresponding increase in their Larmor radius which violates the gyrokinetic approximation. To avoid using a restrictively small time step in the EMCS, the time stepping technique has been modified. Following the method described in Birdsall and Langdon,[1] the Lorentz equation is rearranged by defining intermediate velocities $\mathbf{v}^-$ and $\mathbf{v}^+$:

$$\mathbf{v}_{t-\Delta t/2} = \mathbf{v}^- - \frac{q\mathbf{E}_\perp}{m}\frac{\Delta t}{2} \tag{4.1}$$

$$\mathbf{v}_{t+\Delta t/2} = \mathbf{v}^+ + \frac{q\mathbf{E}_\perp}{m}\frac{\Delta t}{2} \tag{4.2}$$

where $\mathbf{E}_\perp$ is the component of the electric field perpendicular to the magnetic field. Velocities $\mathbf{v}^-$ and $\mathbf{v}^+$ are before and after the magnetic field rotation. Putting these expressions into the finite difference Lorentz equation yields

$$\frac{\mathbf{v}^+ - \mathbf{v}^-}{\Delta t} = \frac{q}{2m}\left(\mathbf{v}^+ + \mathbf{v}^-\right) \times \mathbf{B} \tag{4.3}$$

which can be solved using geometric considerations. This gives an explicit solution method for updating the implicit Lorentz equation. This modification increases the

allowable time step in the EMCS by a factor of approximately 20 over a direct finite differencing in time.

When using dc biases for either the target or substrate, secondary emission of electrons is an important and necessary source of electrons. The secondary emission of electrons from surfaces was therefore included in the EMCS. The procedure followed is to launch electrons from the surface of an electrode (or other specified surface) at a rate determined by the local ion current to the surface and a secondary electron emission coefficient. When using the semi-analytic sheath model, in which the sheath is thin compared to electron mean free paths, electrons are assumed to traverse the sheath without collision. The electron pseudoparticles are therefore launched perpendicular to the surface with an energy equal to the local sheath potential. When not using the sheath model, electrons are launched with a small energy (typically 4 eV) and a Lambertian angular distribution. The trajectories of the secondary electrons and their progeny are tracked using the same algorithms as in the EMCS for bulk electrons (or an injected electron beam)[2] until they slow below a specified energy, typically 3.6 eV (90% of initial energy), thereby joining the bulk electrons. The spatially dependent rate of electrons slowing into the bulk is then included as a source term for electrons in the FKS. The electron energy distribution for the secondary electrons is separately computed and used to generate source functions for electron impact excitation and ionization. These source functions are then used in the FKS.

Metal atoms sputtered from the magnetron target have an initial energy of a few eV and have a mean free path as long as a few cm. These characteristics make a fluid description for their transport questionable. In addition, the disparate energy distribution of the sputtered atoms compared to the bulk metal atoms requires that the influx of metal atoms be represented as a separate group. Therefore, a kinetic Monte Carlo approach, the NMCS, was used to track sputtered metal atoms from the surface until they either slow

down to thermal speeds or strike a surface (assuming a unity sticking coefficient). This allows the kinetic effects of the neutrals to be represented during the initial slowing of the sputtered neutrals, while allowing the use of the more efficient fluid equations for the thermal diffusion process.

Sputtered atoms are assumed to be emitted from the surface of the target with a cosine angular distribution. Since the sputter erosion track is not resolved, the magnetron surface is assumed to be planar. The emitted atoms are given an energy specified by Thompson's law[3] which, for incident ions of several hundred eV, can be approximated with a simple cascade distribution,

$$p(E) = \frac{2E_b}{E^2\left(1 + E_b/E\right)^3} \tag{4.4}$$

where $p(E)$ is the relative probability of emitting an atom of energy E and E_b is the surface binding energy, which typically ranges from 1-4 eV.[4]

In the NMCS, Monte Carlo particles are launched from each point along the magnetron target surface with energies and directions selected from these distributions. The trajectories of the atoms are then tracked as they move through the plasma region and undergo collisions with the plasma species. Only momentum transfer collisions with the background gas atoms are considered. Collisions are modeled as hard sphere collisions in the center of mass reference frame. The collision cross section is computed based on the Lennard-Jones radius of the atoms. For energetic neutrals, this results in forward peaked scattering. The trajectories are followed until they slow to thermal speeds, or until they strike a surface. The ending location of the particles is tallied to generate a Green's function G(r,r') designating the spatial distribution of atoms slowing to thermal speeds at a location r within the plasma volume originating from location r' on the target.

The sputtering rate at each location along the target is determined by the local ion flux to the surface. In addition, charge-exchange reactions near the target surface produce fast neutrals, which can also sputter target atoms. To account for sputtering by fast neutrals, all charge-exchange reactions of ions directed towards the surface which occurs in the mesh cell adjacent to the target are assumed to generate hot neutrals which contribute to sputtering. This approximation was made based on the fact that these ions have already traversed a large fraction of the presheath. Therefore, the fast neutral flux produced by charge exchange is computed by multiplying the incident ion flux times the neutral atom density, the charge exchange cross section, and the width of the last cell. The total sputter rate is, then, the ion flux to the surface plus the fast neutral flux times the sputter yield. The sputter yield is assumed to be constant across the target for a given incident ion and material composition. The sputter rate which has been computed is then convolved with the Green's function for slowing down generated in the NMCS to determine the spatially dependent source rates of sputtered atoms entering the fluid. One can show that in virtually all plasmas of interest (pressures of 10-40 mTorr, electron densities 10^{11} - 10^{12} cm^{-3}), the probability that a sputtered atom undergoes excitation or ionization prior to thermalizing is small, and so these processes are ignored in the NMCS.

Electron-impact cross sections and ion mobilities for the metal systems of interest are not well characterized. For example, few electron-impact cross sections are available for Al and Ti, which are of particular interest in the semiconductor industry. The knowledge base for Cu is fairly well characterized because of past interest in copper vapor lasers.[5,6] The lack of a complete cross section set and gas phase rate coefficients for Al and Ti presents difficulty in modeling, and therefore a Cu IMPVD system has been modeled with the intention of characterizing the general behavior of IMPVD systems.

The complexity of the atomic structure of the Cu atom requires some simplifications in order to reduce the magnitude of computations needed. Therefore,

within the FKS, the excited states of copper are lumped into an effective excited state denoted as Cu^*, which has the characteristics of $Cu[^2D_{5/2}]$. The higher excited states were not explicitly tracked within the FKS because of their relatively short radiative decay time[5] and their low rate of excitation compared to the $Cu[^2D_{5/2}]$ level. This was done to eliminate the necessity of tracking several excited states of Cu, while maintaining the important processes. Several runs were performed with and without the higher excited states in the FKS and the results were essentially the same. Within the EMCS, however, electron-impact excitations from the ground state ($^2S_{1/2}$,) to the metastable states ($^2D_{5/2}$, $^2D_{3/2}$), resonance states ($^2P_{1/2}$, and $^2P_{3/2}$), and a pseudostate representing higher levels, and from the metastable $Cu^*[^2D_{5/2}]$ to the resonance states ($^2P_{1/2}$, and $^2P_{5/2}$) and pseudostate, are included for the purposes of determining the electron energy distribution functions. Cross sections are essentially the same as those used in Ref. 6, except that the ionization cross section from the ground state was from curve fits by R. J. Carman,[7] based on published data of Sheibner, et al.[8] and on unpublished raw data of Sheibner and Hazi.[9] The electron-impact cross sections used are shown in Fig. 4.1. Heavy-body reaction rates were obtained from Ref. 6, and a summary of the Ar/Cu reactions used is shown in Table 4.1.[6,7,10-15]

4.3. Plasma Behavior in an Ionized Metal Sputter Deposition Reactor

The geometry used in our simulations was discussed in Chapter 1 (Fig. 1.3) and is based on the experimental geometries of Yamashita[16] and of Rossnagel and Hopwood.[17,18] It consists of a 20 cm diameter dc magnetron sputter source with an applied voltage of -250 V on the target. Due to the limitations of our two-dimensional simulation, only a circular magnet configuration can be modeled. The circular sputter track is defined using cusp magnet rings above the sputter target. The chamber height is 9 cm. A two-turn solenoid, powered at 13.56 MHz, is immersed in the plasma and

deposits 1 kW of inductively coupled power. The purpose of the solenoid is to ionize the sputtered metal atoms. The substrate is biased at -20 V dc to accelerate ions toward the surface. Due to the biasing of the coils (described below), ions can obtain sufficient energy to sputter the coils which are assumed to be made of copper. Therefore, sputtering of copper atoms occurs from both the target and the coils. The Ar fill pressure is varied from 15 to 45 mTorr. The sputter parameters used were E_b = 3.5 eV and a sputter yield = 2.0.

Since the coils are immersed directly in the plasma, they function equivalently to electrodes in an RIE system with respect to biasing of the plasma potential and heating the plasma, and so their electrical coupling to the plasma must be considered. As a result, the rf cycle in the FKS is resolved. The details of this coupling depend on the configuration of the driving circuitry of the coils, a topic which is beyond the scope of the present study. The amplitude of the rf potential on the coils has, therefore, simply been specified to be 100 V, which is acknowledged to be a lower limit. In addition, there is assumed be a single blocking capacitor in series with the power supply upon which a dc bias is collected. Since the area ratio (coil to wall) is very large, the dc bias typically is nearly the rf amplitude.

The electron density and Cu^+ density are shown in Fig. 4.2, for 35 mTorr Ar fill pressure. The electron density has a peak value of 1.4 x 10^{12} cm^{-3}, which is somewhat higher than that obtained in similarly sized and powered inductively coupled etching reactors, and is likely due to the low ionization potential of Cu (7.49 eV). Although the primary ionization source for the electrons is near the coils where the inductive power deposition peaks, the large aspect ratio and lack of volumetric sources of electron loss (such as attachment or dissociative recombination) leads to the electron density peaking on axis. The peak ionization source near the coils is 6 x 10^{16} $cm^{-3}s^{-1}$ for a power deposition of 1300 W, whereas that near the magnetron is 5 x 10^{15} $cm^{-3}s^{-1}$ for a power

deposition of 1700 W. The lower ionization source near the magnetron indicates that the majority of the power goes into ion acceleration. Contributions to the ionization source from secondary emission are displaced into the bulk. This device functions as an externally sustained discharge where ionization, and hence current to the target, is largely determined by the inductive coil heating. At the operating pressure of 35 mTorr, the electron collisionality is much higher than at a few mTorr where traditional sputter magnetrons operate. This collisionality somewhat compromises the trapping of electrons in the closed track of the magnetron, and produces a diffusive charged density profile, rather than a well confined source beneath the sputter target (although some scalloping of the electron density in the cusps of the magnetron can be seen). The Cu^+ density has a peak value of 3.5×10^{11} cm^{-3}, approximately 25% of the total ion density, and its profile is centered on axis, following the electron density.

The source of sputtered Cu atoms and the total Cu neutral atom density are shown in Fig. 4.3. The Cu atom source is the rate at which atoms sputtered from the surface slow down into the thermal group, making the transition from kinetic transport to fluid transport. The sputter source is peaked near the radial edge of the plasma zone, a consequence of the high rate of sputtering from the coils. The peak value of the sputter source is 1.5×10^{16} $cm^{-3}s^{-1}$. This high rate of sputtering is sustained by the large amount of power deposition from the rf coils, producing a high ion flux back to the coils. The total Cu neutral density, which includes ground-state and excited-state Cu atoms, is shown in Fig. 4.3b. The peak value for the neutral Cu is 2.0×10^{12} cm^{-3} and is peaked off-axis below the magnets. The off-axis peak is caused by the high sputtering rate from the coils as well as by the off-axis sputtering source from the target. Due to the fact that the lowest excited states of Cu are metastable yet have a large excitation rate due to their low threshold energy (1.4 eV), a large fraction of the Cu atoms are excited, in this case approximately 25%.

The fluxes of Cu species to the wafer surface for 35 mTorr Ar fill pressure are shown in Fig. 4.4a, including sputtering from the coil and assuming that all Cu species have a unity sticking coefficient. The unthermalized flux is the flux of sputtered atoms which have traversed the reactor from the target to the substrate without undergoing sufficient collisions to slow to thermal speeds. The unthermalized flux is strongly peaked at the outer edge of the wafer because of the high rate of sputtering from the nearby coils and the off-axis circular sputter track from the target. The Cu neutral flux has much less variation although it is slightly peaked at ≈7.5 cm from the axis. The more uniform thermal Cu flux compared to the unthermalized flux is due to the diffusivity of Cu atoms in the plasma. The ion flux is relatively uniform at small radii, but tapers off at larger radii. From experience with designing conventional ICP plasma sources, one can recoup some of this uniformity by a combination of operating with a somewhat squatter aspect ratio, whose value is a sensitive function of pressure, and by changing the position of the rf coils. The flux of the Cu^* is relatively uniform across the wafer and approximately 13% of the total. The total deposition flux of Cu is the sum of the fluxes of all neutral (thermal and hot) and ionized Cu species. The total flux increases at larger radii because of the unthermalized neutral component, although the flux of the other components is decreasing.

Approximately 50% of the Cu flux is ionized near the center of the wafer. This fraction decreases at larger radii due to the increase in the unthermalized component of the neutral flux produced by the proximity of the coils. To prevent this trend, one must either minimize sputtering from the coil, place the coils sufficiently far from the wafer that the sputtered atom flux has an opportunity to thermalize and be ionized prior to striking the substrate, or place the coils outside the chamber.

The same conditions were simulated with the exception that it is specified that there be no sputtering from the coils. The electron density and Cu^+ densities for this case

are shown in Fig 4.5. The Cu^+ density has a peak value of 1.1 x 10^{11} cm^{-3}, which is significantly smaller and more strongly peaked on-axis than in the case with coil sputtering. This trend is due to a decrease in neutral copper density, especially near the coils. The electron density has a peak value of 1.2 x 10^{12} cm^{-3}, slightly smaller than that when including coil sputtering; however, it is more spatially uniform due to a more uniform ionization rate. Although Cu is more easily ionized than Ar, it also has a larger rate of momentum transfer and inelastic energy loss. The higher Cu density which results from including sputtering from the coils therefore “damps” the electron temperature, localizing the higher temperature near the coils.

The copper sputter source and neutral density are shown in Fig. 4.6 for the case where no sputtering is allowed from the coils. The sputter source has a peak value of 5.5 x 10^{15} $cm^{-3}s^{-1}$, which is smaller than the case where sputtering is allowed from the coils. (The total sputter rate for a fixed sputter yield, which has been assumed in this model, depends only on the total flux of ions to the surface. In the case where sputtering from the coils is allowed, the contributions from the coils actually exceed the contributions from the target.) The peak in the sputter source is located below the magnetron target, although it is not located directly beneath the magnets. This condition results from the relatively uniform sputter source from the target, combined with the short mean free path of the neutrals in a cylindrical geometry, leading to a source rate peaked on-axis. Since our simulation is only two-dimensional, the magnetron tracks are at best nested circular loops. Sputtering is therefore directly proportional to the ion flux incident onto the target. In many commercial magnetrons, the "racetrack" cuts across radii, thereby "mixing" incident ion fluxes from different radii. The total neutral Cu density in the plasma has a peak value of 4.6 x 10^{11} cm^{-3}. The Cu density for this case is significantly lower and more sharply peaked on-`axis than when sputtering from the coils

is allowed, thereby emphasizing the importance of considering this source of metal atoms in reactor design.

The deposition fluxes as a function of radius are shown in Fig. 4.4b when no sputtering is allowed from the coils. As expected, all incident fluxes fall off at larger radii, because there is no secondary source of sputtered Cu from the coils. The overall deposition flux without sputtering from the coils is significantly lower than when sputtering from the coils is allowed, which in turn leads to a slightly higher percentage of the flux which is ionized, approximately 60% on axis. This results from less cooling of the electrons in the plasma when the Cu density is low. The unthermalized flux in this case is only a small fraction of the total flux to the surface, which indicates that the combination of reactor height and pressure for this case provides for sufficient thermalization of the sputtered atoms in the plasma volume, provided that the sputter target is the primary source of copper in the system.

The variations of the Cu ionized fraction and total deposition flux with fill pressure and target voltage are shown in Fig. 4.7. To offset the influence of sputtering from the coils, values are averaged over the inner 4 cm radius of the wafer, as shown by the vertical line in Fig. 4.4. As the pressure increases, the mean free path of the atoms decreases. The fraction of sputtered atoms which slow down into the plasma increases, allowing more of them to be ionized before reaching the wafer. The ionized fraction increases from approximately 29% at 15 mTorr to approximately 47% at 45 mTorr. At the same time, increasing pressure has the effect of dispersing the atoms due to diffusion, which results in a lower deposition rate, because more of the sputtered atoms are lost to other surfaces in the reactor. The deposition flux decreases from approximately 5.5 x 10^{16} cm^{-2} s^{-1} (3900 Å/min) at 15 mTorr to approximately 1.5 x 10^{16} cm^{-2} s^{-1} (1100 Å/min) at 45 mTorr. This implies a trade-off between ionized fraction and deposition rate, which for this geometry and operating conditions would be between 25 and 35 mTorr.

Experiments by Yamashita with a 5 cm gap between the target and the substrate, at 10 mTorr and 800 W dc target power have a deposition rate of 11,200 Å/min for Cu deposition.[16]

The variations of Cu deposition flux and the ionized fraction with target voltage is shown in Fig. 4.7(b). In these cases, the sputter yield was assumed to remain constant, so that the main effect of increasing the target voltage is to increase the rate of plasma generation near the magnetron surface due to secondary electron emission. The deposition flux does not change appreciably between the -100 V and the -250 V cases, which implies that at this point the ion flux to the target is controlled primarily by the plasma generated by the rf coils. As the voltage is increased to -350 V, the deposition rate experiences a small increase due to a slightly larger rate of ionization by secondary electrons leading to larger rates of Cu sputtering, although the ionized fraction remains near 50%.

By moving the coils farther away from the substrate, it is expected that uniformity of the Cu flux will improve by reducing the unthermalized Cu flux resulting from coil sputtering. This is shown in Fig. 4.8. Cu fluxes are shown when the coils have been raised 1.5 cm towards the target compared to the standard case. The Cu^+ flux is nearly the same as seen in the standard case (Fig. 4.4(a)). The main difference between this case and the standard case is that the neutral fluxes are smaller. The unthermalized flux is substantially reduced, especially at the outer radius, with a peak value of approximately 1.2×10^{16} cm^{-2} s^{-1} (850 Å/min) at the outer radius compared to approximately 2.8×10^{16} cm^{-2} s^{-1} (2000 Å/min) in the standard case. The other neutral fluxes are also smaller resulting in a total deposition flux which is smaller and somewhat more uniform. Since the coils have been moved closer to the top of the reactor, diffusion losses of sputtered Cu atoms are larger. Since the ionized flux is nearly the same, these conditions lead to a higher ionized percentage, approximately 62% on the axis.

4.4. Summary

A two-dimensional model for ionized metal physical vapor deposition has been developed and has been applied to the investigation and design of devices for Cu deposition. For a modified magnetron sputter source, pressure plays an important part in determining the transport of sputtered atoms. At low pressure, the sputtered atoms traverse the reactor with few collisions before reaching the wafer, while at higher pressure, the transport becomes diffusive, which allows for ionization for the metal atoms. However, the increase in pressure creates a diffusive loss mechanism for atoms to the walls, which reduces the deposition rate. Sputtering from the coils, which is caused by the high plasma density generated near the coils from both the inductive heating and capacitive ion acceleration into the coils, is seen to be a significant source of metal atoms. The sputtering from the coils not only limits the lifetime of the coils, but can lead to nonuniformities in the deposition flux, thereby underscoring the need for careful choice of coil location for optimized operation.

Table 4.1. Ar/Cu chemistry.

Reaction[a]	Rate Coefficient ($cm^3\ s^{-1}$)	Reference
$e + Ar \rightarrow Ar + e$	[b]	10
$e + Ar \rightarrow Ar[4s] + e$	[b]	11
$e + Ar \rightarrow Ar[4p] + e$	[b]	11
$e + Ar \rightarrow Ar^+ + e + e$	[b]	12
$e + Ar[4s] \rightarrow Ar^+ + e + e$	[b]	13
$e + Ar^+ \rightarrow Ar^+ + e$	[b]	14
$e + Cu \rightarrow Cu + e$	[b]	6
$e + Cu \rightarrow Cu[^2D_{5/2}] + e$	[b]	6
$e + Cu \rightarrow Cu[^2D_{3/2}] + e$	[b]	6
$e + Cu \rightarrow Cu[^2P_{1/2}] + e$	[b]	6
$e + Cu \rightarrow Cu[^2P_{3/2}] + e$	[b]	6
$e + Cu \rightarrow Cu[pseudostate] + e$	[b]	6
$e + Cu \rightarrow Cu^+ + e + e$	[b]	7
$e + Cu[^2D_{5/2}] \rightarrow Cu[^2D_{5/2}] + e$	[b]	6
$e + Cu[^2D_{5/2}] \rightarrow Cu[^2P_{1/2}] + e$	[b]	6
$e + Cu[^2D_{5/2}] \rightarrow Cu[^2P_{3/2}] + e$	[b]	6
$e + Cu[^2D_{5/2}] \rightarrow Cu[pseudostate] + e$	[b]	6
$e + Cu[^2D_{5/2}] \rightarrow Cu^+ + e + e$	[b]	6
$Ar^* + Ar^* \rightarrow Ar^+ + Ar + e$	$5x10^{-10}$	15
$Cu^* + Cu \rightarrow Cu + Cu$	$1x10^{-12}$	[c]
$Cu^* + Cu^* \rightarrow Cu^* + Cu$	$1x10^{-12}$	[c]
$Ar^* + Cu \rightarrow Ar + Cu^+ + e$	$5x10^{-11}$	[c]
$Ar^* + Cu^* \rightarrow Ar + Cu^+ + e$	$5x10^{-11}$	[c]
$Ar^+ + Cu \rightarrow Ar + Cu^+ + e$	$5x10^{-10}$	[c]
$Ar^+ + Cu^* \rightarrow Ar + Cu^+ + e$	$5x10^{-10}$	[c]
$Cu^+ + Cu \rightarrow Cu + Cu^+$	$6x10^{-10}$	[c]
$Ar^+ + Ar \rightarrow Ar + Ar^+$	$1x10^{-9}$	[c]

[a] In the FKS, all excitations of Ar are lumped into Ar^*, which is effectively Ar[4s], and all excitations of Cu are lumped into Cu^*, which is effectively $Cu[^2D_{5/2}]$.
[b] Rate coefficients are calculated from electron energy distribution obtained in the EMCS.
[c] Estimated.

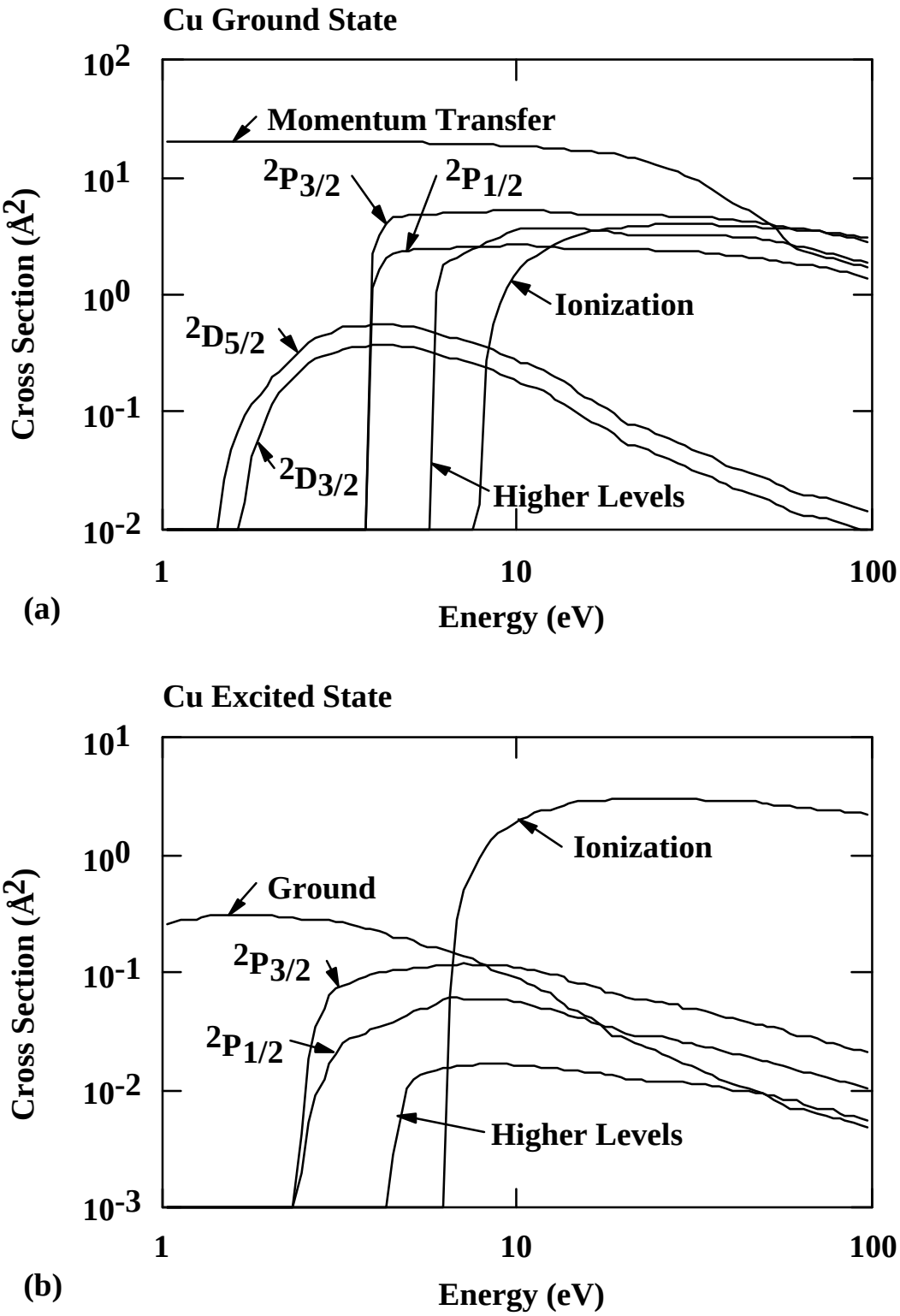

Fig. 4.1. Cu electron impact cross sections. (a) Excitations from the ground state. (b) Excitations from the effective excited state Cu[$^2D_{5/2}$], our effective Cu*.

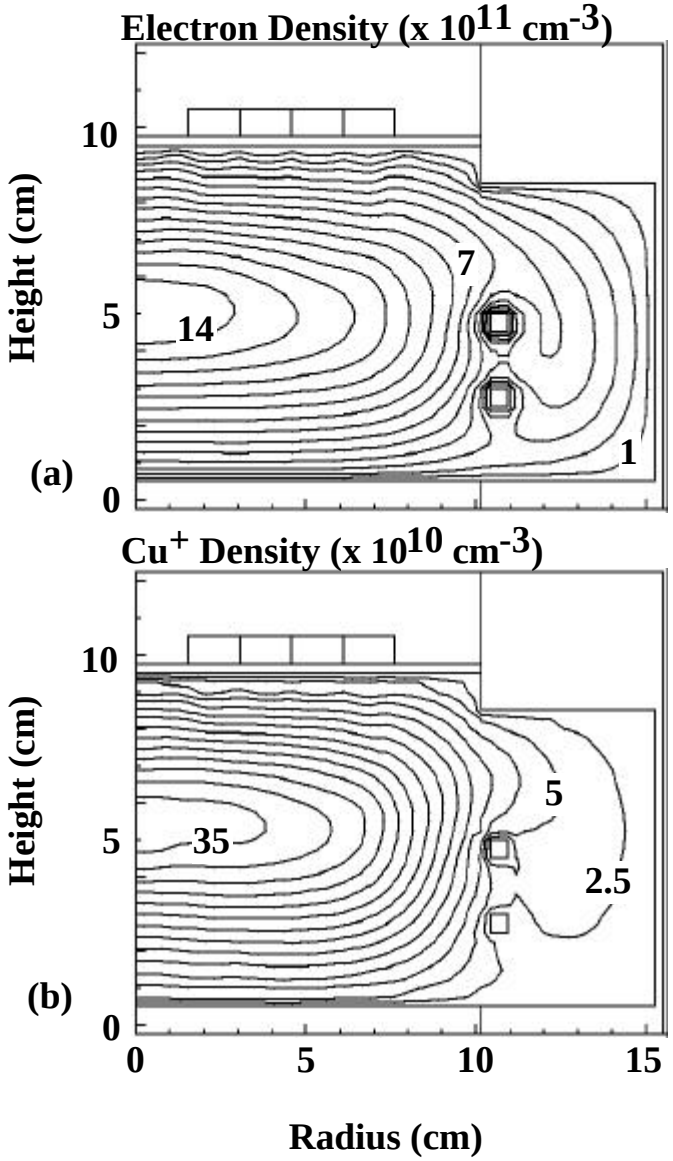

Fig. 4.2. Electron and Cu^+ ion density contours for an IMPVD at 35 mTorr, with -250 V on the sputter target, 1 kW inductive power, and -20 V applied to the substrate. (a) Electron density. Contours values are x 10^{11} cm^{-3}. (b) Cu^+ ion density. Contours values are x 10^{10} cm^{-3}. The Cu^+ density is nearly 25% of the total ion density.

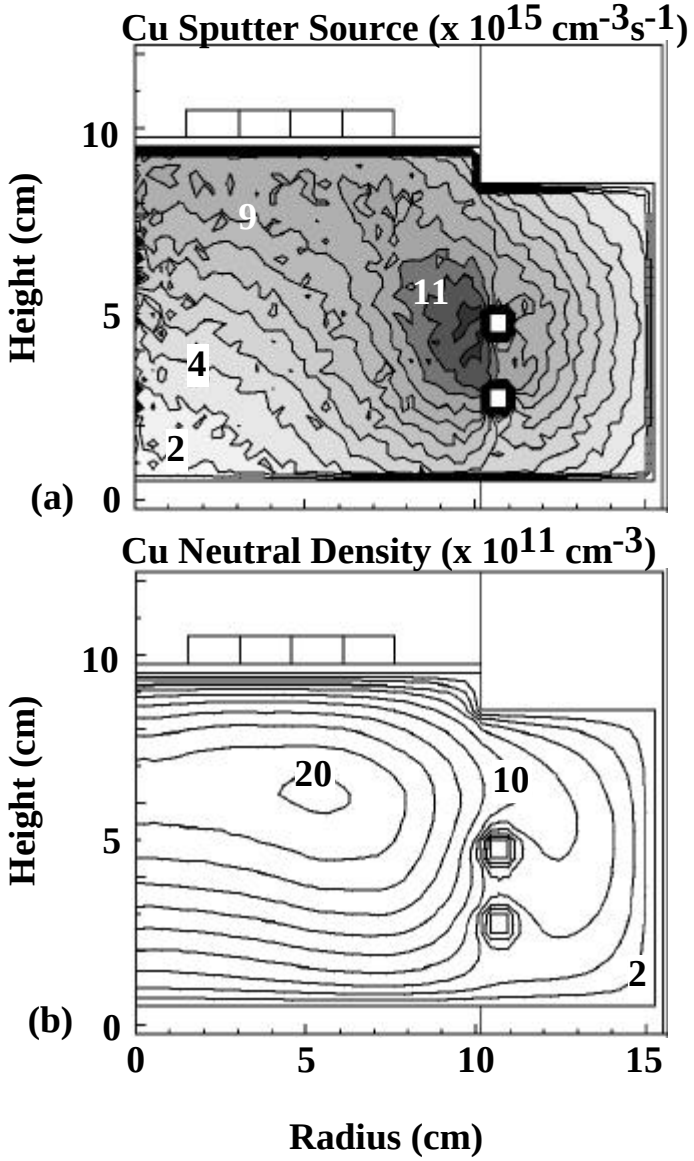

Fig. 4.3. Neutral copper properties. (a) Source of sputtered atoms which have slowed to thermal speed. Contours values are x 10^{15} $cm^{-3}s^{-1}$. (b) Cu neutral density, including both ground state and excited state atoms. Contours values are x 10^{11} cm^{-3}. The Cu density peaks off axis due to coil sputtering.

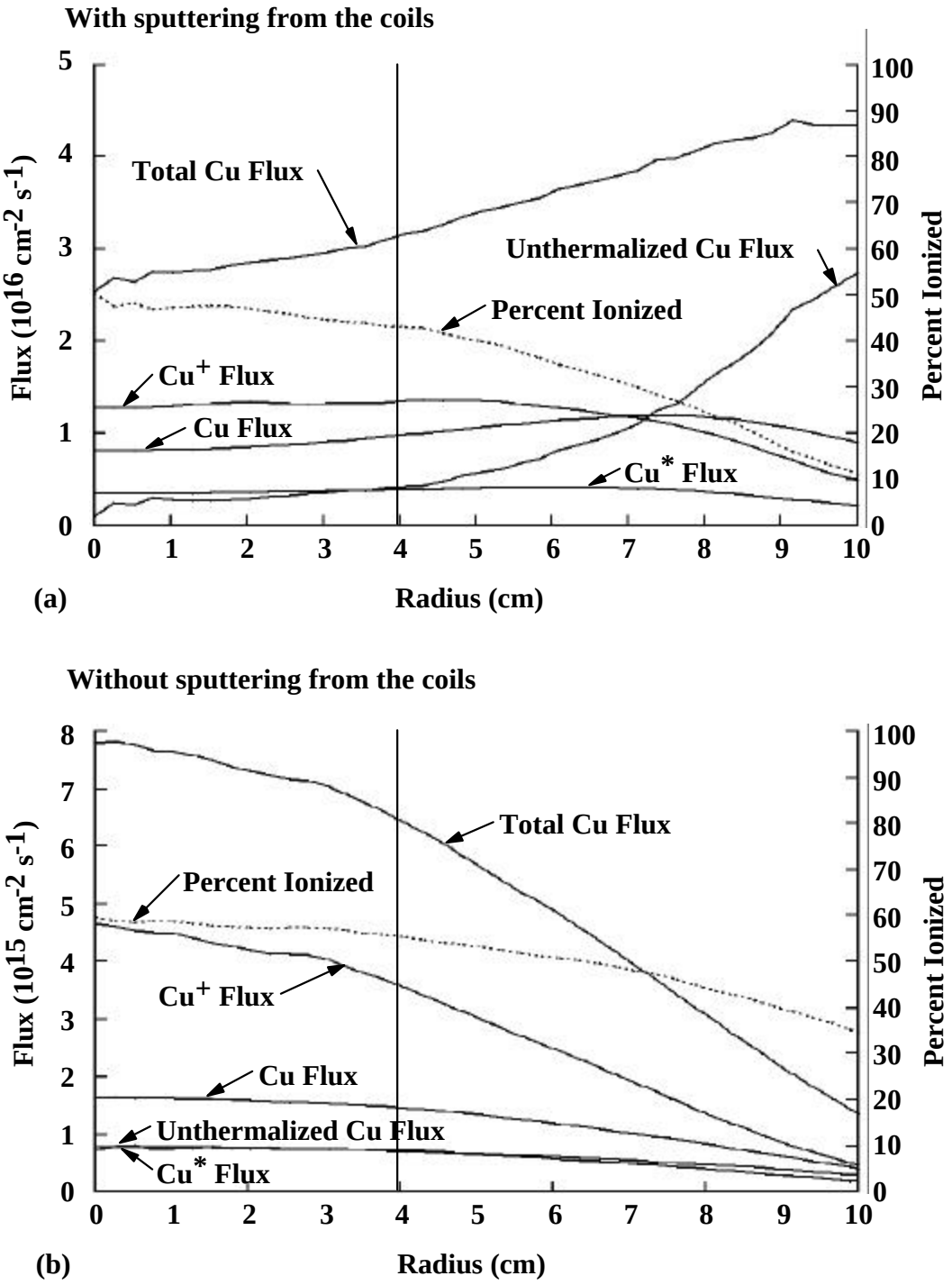

Fig. 4.4. Cu deposition flux to the substrate and fraction ionized. The neutral flux consists of contributions from Cu ground state, Cu^*, and the unthermalized sputter flux. (a) Fluxes with sputtering from the coils. (b) Fluxes without sputtering from the coils. Coil sputtering produces an off-axis maximum in the Cu atom flux.

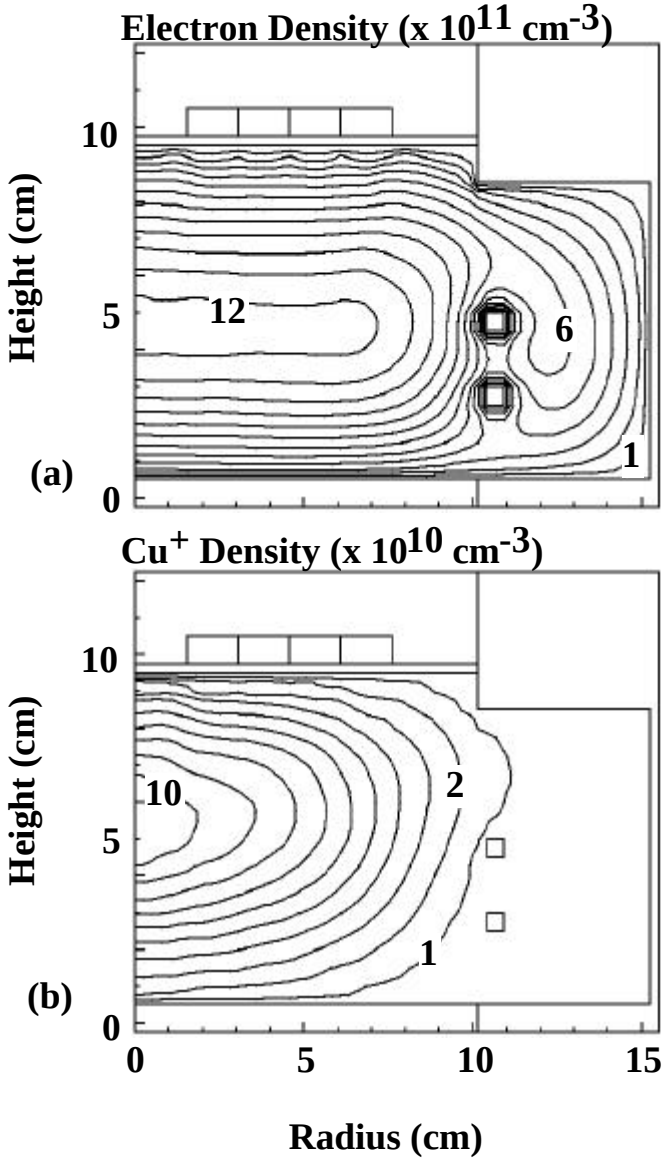

Fig. 4.5. Electron and Cu^+ ion density without sputtering from the coils. (a) Electron density. Contours values are x 10^{11} cm^{-3}. (b) Cu^+ ion density. Contours values are x 10^{10} cm^{-3}.

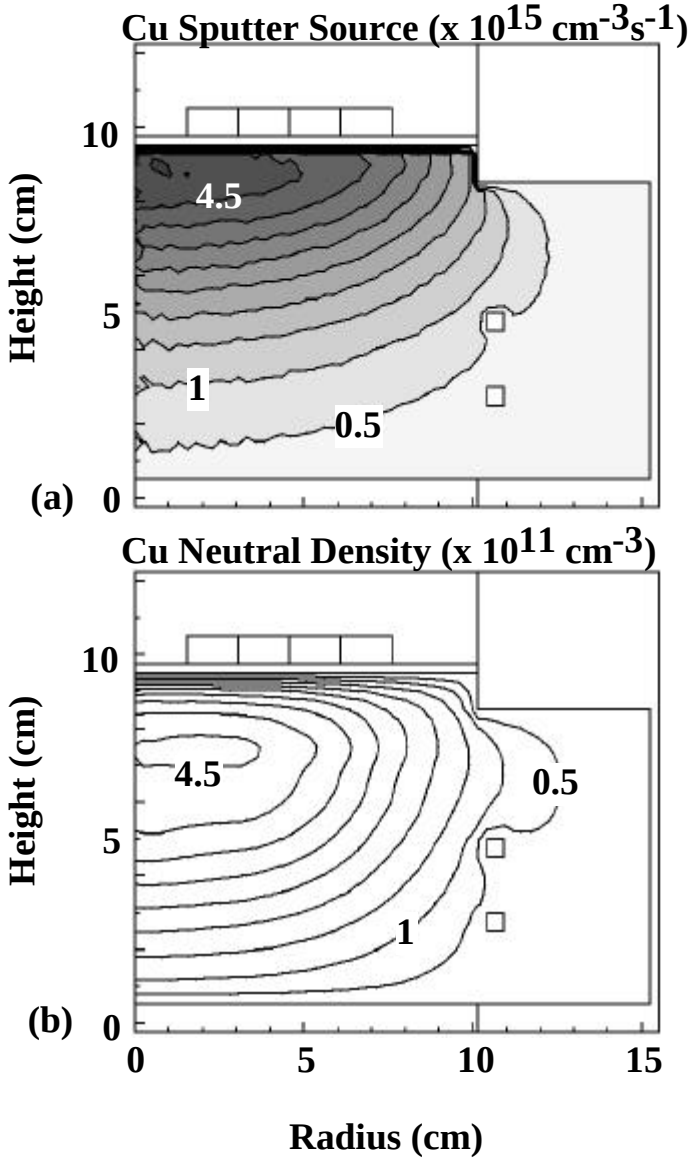

Fig. 4.6. Cu sputter source and density without sputtering from the coils. (a) Source of sputtered atoms which have slowed to thermal speed. Contours values are x 10^{15} $cm^{-3}s^{-1}$. (b) Cu neutral density, including both ground state and excited state atoms. Contours values are x 10^{11} cm^{-3}. The absence of a source of copper from the coils results in an on axis maximum in Cu density.

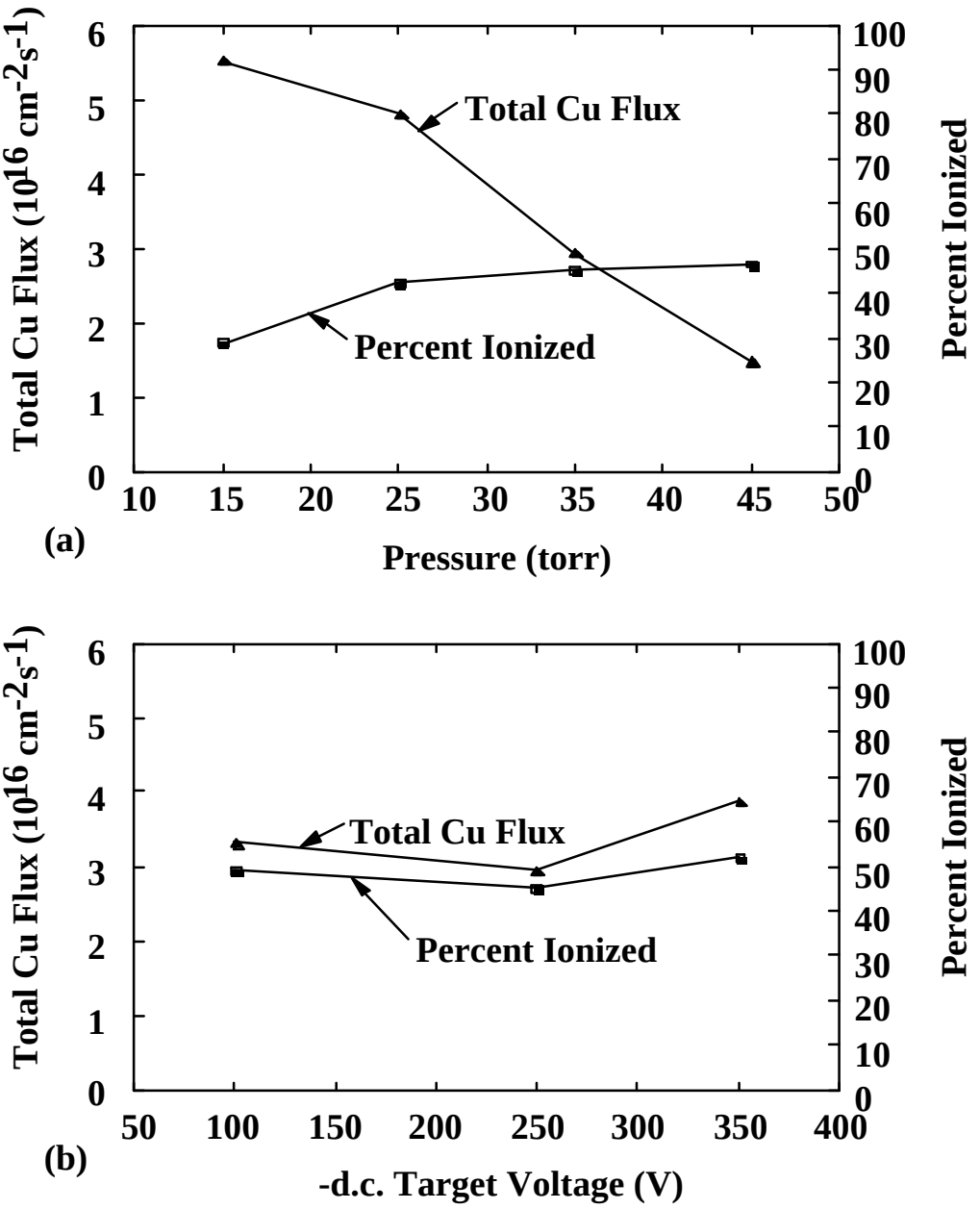

Fig. 4.7. Cu deposition flux and fraction ionized. (a) As a function of pressure and (b) as a function of dc voltage on the target. Increasing pressure reduces the Cu flux but increases the fraction ionized.

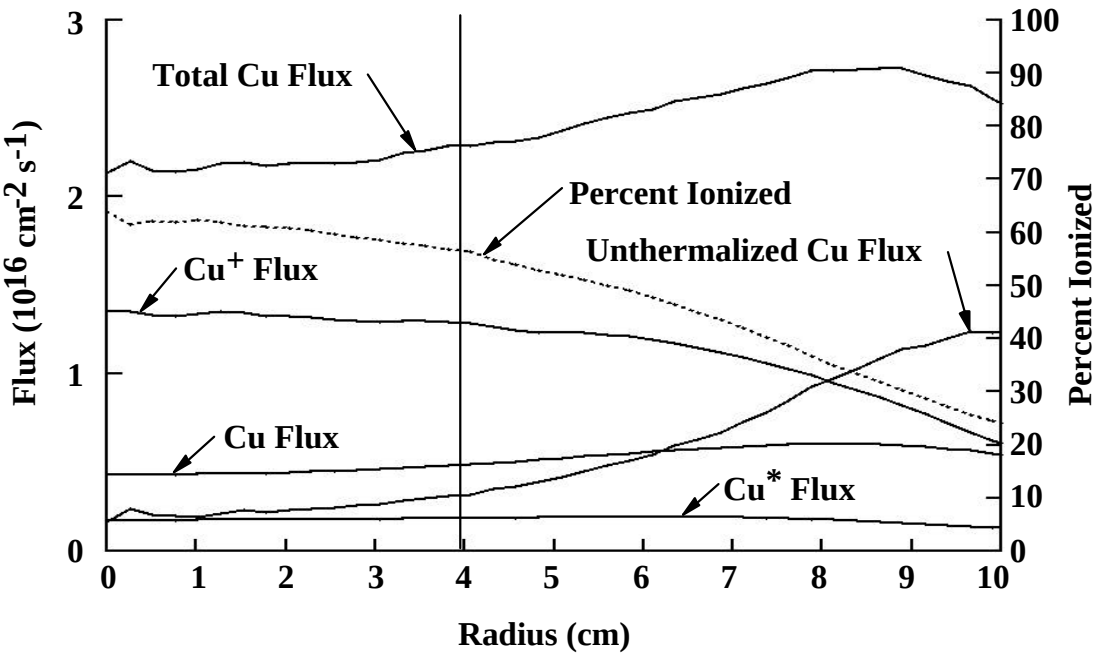

Fig. 4.8. Deposition fluxes and fraction ionized when the coils are raised 1.5 cm toward the sputter target.

4.5 References

[1] C. K. Birdsall and A. B. Langdon, Plasma Physics Via Computer Simulation, McGraw-Hill Book Company, New York, 1985.

[2] M. J. Kushner, W. Z. Collison and D. N. Ruzic, *J. Vac. Sci. Technol. A*, vol. 14, p. 2094, 1996.

[3] T. Heberlein, G. Krautheim, and W. Wuttke, *Vacuum*, vol. 42, p. 47, 1991.

[4] M. A. Lieberman and A. J. Lichtenberg, Principles of Plasma Discharges and Materials Processing, John Wiley and sons, inc., New York, 1994.

[5] R. J. Carman, D. J. W. Brown and J. A. Piper, *IEEE J. Quantum Electron.*, vol. 30, p. 1876, 1994.

[6] M. J. Kushner and B. E. Warner, *J. Appl. Phys.*, vol. 54, p. 2970, 1983.

[7] R. J. Carman (private communication).

[8] K. F. Sheibner, A. U. Hazi, and R. J. W. Henry, *Phys. Rev. A*, vol. 35, p. 4869, 1987.

[9] K. F. Sheibner and A. U. Hazi (private communication).

[10] M. Hayashi, Nagoya Institute of Technology Report No. IPPJ-AM-19, 1991.

[11] K. Tachibana, *Phys. Rev. A*, vol. 34, p. 1007, 1987.

[12] D. Rapp and P. Englander-Golden, *J. Chem. Phys.*, vol. 43, p. 1464, 1965.

[13] R. H. McFarland and J. D. Kinney, *Phys. Rev.*, vol. 137, p. A1058, 1965.

[14] M. Mitchner and C. Kruger, Partially Ionized Gases, Wiley, New York, 1973, chap. 2.

[15] P. K. Leichner and R. J. Ericson, *Phys. Rev. A*, vol. 9, p. 251, 1974.

[16] M. Yamashita, *J. Vac. Sci. Technol. A*, vol. 7, p. 151, 1989.

[17] S. M. Rossnagel and J. Hopwood, *Appl. Phys. Lett.*, vol. 63, p. 3285, 1993.

[18] S. M. Rossnagel and J. Hopwood, *J. Vac. Sci. Technol. B*, vol. 12, p. 449, 1994.

5. MESOSCALE SURFACE CHEMISTRY IN PLASMA ETCHING EQUIPMENT

5.1. Introduction

The surface chemistry in plasma processing reactors plays an important role in the behavior of the entire plasma. Surface topography on the wafer being processed, which determines the chemical behavior of the surface, varies on spatial scales which are much smaller than the reactor dimensions. To account for the surface effects on the plasma behavior, a mesoscale Monte Carlo simulation (MSMCS) has been developed which joins the die scale surface chemistry with the plasma scale in the HPEM. The presence of etch products in the plasma is seen to perturb the bulk plasma. The presence of photoresist redeposition is seen to have a minor, but important, effect on the etch rate. At low pressure, the etch rate is increased, although the probability of a given ion causing an etch is decreased. In Section 5.2, the model is described. Results for a chlorine etch of polysilicon is discussed in Section 5.3, where variations in plasma operating conditions, surface features and changes in surface chemistry are examined, as well as their impact on the plasma behavior examined. A summary is made in Section 5.4.

5.2. The Mesoscale Monte Carlo Simulation

In the FKS, surface chemistry is included by reactive sticking coefficients. In this case, the flux to the wall is modified by the probability that a species incident on the surface will react. The fraction of the incident flux which reacts is then returned as the new species. Previously in the HPEM, the surface reactive sticking coefficients were specified in the input files before the case was run. With the addition of the MSMCS, the reactive sticking coefficients used in the FKS are generated by running a die-scale Monte Carlo simulation. Thus the plasma conditions determine the reactive sticking coefficients self consistently.

The MCMCS launches pseudo particles to the surface, and tracks their transport near the surface before striking and after reacting. The surface is resolved in two dimensions and can contain different regions in which the surface chemistry is different, such as an area which consists entirely of exposed silicon, or photoresist, or varying combinations of the two. Nonvolatile surface species coverage is tracked so that multi-step chemistry can be represented, such as an etch process where Si is chlorinated and then removed from the surface by ion bombardment.

The MSMCS uses the incident fluxes determined in the FKS to launch particles toward the surface. The weight of a pseudoparticle is the number of atoms incident on the surface, and therefore the relative weight of any given species is determined by the magnitude of the flux to the surface. The absolute weight of a particle is chosen such that any single pseudoparticle will not change the surface coverage in a surface cell by more than a specified percentage, typically less than 1%. Because the particles are weighted based on their incident flux, an equal probability is used when choosing the particle's species. The velocity of the incident particle is randomly chosen using a drifting Maxwellian distribution where the drift velocity is the fluid velocity of that species as computed in the FKS.

Near the surface, particle motion is tracked for neutral species, both incident and after leaving the surface. Ion species are assumed to travel directly to the surface. Because the electric field near the surface is very strong, even if a charged particle has a collision it will not be reflected; and since anisotropy is not considered on the scales of interest for this model, deflection can be ignored. By ignoring ion collisions in the sheath, asymmetric charge exchange will be neglected; however, symmetric charge exchange will not be significantly affected because hot neutrals behave chemically like ions at the surface.

Neutral particle motion is tracked by computing the particle's distance to the next collision based on its mean free path. Particles which collide in the near surface region are assumed to have a hard sphere collision with a randomly chosen gas species. The collision partner is chosen based on the neutral atom densities in the cell above the surface as computed in the FKS. The velocity of the collision partner is randomly generated using a Maxwellian distribution at the local gas temperature. Collisions are assumed to be perfectly elastic. After the new velocity is computed, a new distance to the next collision is chosen and the process is repeated.

When a particle strikes the surface, its position on the two-dimensional grid is determined. The cell stuck by the particle determines which reactions are possible. To reduce the number of particles needed in the simulation, especially when there is a low probability reaction, all possible reactions for that species in that cell are computed and particles are released for all products. The weight of the product particle i, W_i is computed for a reaction j by

$$W_i = f_{ij} W_{incident} C_k p_j \tag{5.1}$$

where $W_{incident}$ is the incident particle weight, C_k is the surface coverage for reactant surface species k, p_j is the probability for the reaction j and, f_{ij} is the stoichiometric factor for species i. As an illustration, consider the reaction where incident species A strikes the surface on which there is a fractional coverage of surface species B. One reaction for A + B is shown below which produces a new surface species C and two gas phase species D and E, where E has a stoichiometric factor of two. This reaction has a probability *prob* and is summarized as

$$A_{(g)} + B_{(s)} \xrightarrow{prob} C_{(s)} + D_{(g)} + 2E_{(g)}\,. \tag{5.2}$$

Because of this reaction, two new pseudo particles are launched with weights:

$$\begin{aligned} W_D &= W_A C_B prob \\ W_E &= 2W_A C_B prob. \end{aligned} \tag{5.3}$$

In addition, the fractional coverage of species B is reduced and species C increased by

$$\Delta C_{B/C} = \pm W_A C_B prob / W_{cell} \tag{5.4}$$

where W_{cell} is the number of atoms in the surface cell.

When an incident particle is launched, its weight is recorded. Then, it and all of the particles produced by it, are tracked until all of them return to the bulk plasma or stick to the surface. When a particle returns to the bulk plasma, its weight is recorded. At the end of the MSMCS, the reactive sticking coefficients for the FKS are computed. The total sticking probability for species *i*, S_i, is,

$$S_i = 1 - W_{out_{ii}} / W_{in_i} \tag{5.4}$$

where $W_{out_{ii}}$ is the total weight of particles of species *i* which return to the bulk plasma as a result of launching species *i*, and W_{in_i} is the total weight of all particles of species *i* launched during the simulation. The fraction of species *i* which returns from the surface as species *j*, F_{ij}, is,

$$F_{ij} = W_{out_{ij}} / W_{in_i} \tag{5.4}$$

where $W_{out_{ij}}$ is the total weight of particles of species *j* which return to the bulk plasma as a result of launching species *i*.

5.3. Surface Chemistry Modeling of Polysilicon Etching

The MSMCS has been used to examine the etching of polysilicon with chlorine in the Inductively Coupled-Gaseous Electronics Conference Reference Cell (IC-GECRC). This reactor was discussed in Section 3.3 and additional details are contained in Ref. 1. (see Fig. 3.2). The gas used in this study is a 50/50 mixture of Ar/Cl_2. Pressure is 10 mTorr, power is 100 W ICP and the flow rate is 10 sccm. A test pattern for the wafer die is shown in Fig. 5.1 and consists of one large region and two smaller regions where the polysilicon is partially (10%) exposed. The remaining area is entirely covered with photoresist.

The etching process consists of two steps. In the first step, the silicon near the surface is chlorinated, and then the $SiCl_2$ is removed from the surface by ion bombardment. In addition to etching reactions, sputtering, redeposition and resputtering of photoresist are allowed. Redeposition of photoresist is tracked on all surface species and must be removed, in this chemistry by ion bombardment, before further chemical processes may proceed. In addition to these surface reactions, surface recombination of Cl as well as quenching of excited states and ions at the surface are included. The major reaction mechanisms, their standard reaction probabilities and their regions of applicability are summarized in Table 5.1. This is a simplified surface chemistry and addresses the kinetics through the choice of reaction probabilities. On other surfaces, the

photoresist was assumed to stick with a probability of 1.0 and the etch product, $SiCl_2$, was assumed to stick with a probability of 0.3.

To compare the effect of surface product densities on the plasma properties, the HPEM was run both with the MSMCS and with no surface chemistry. The electron densities for these cases are shown in Fig. 5.2. In both cases it is seen that the density is nearly centered on axis, with a slight tendency to increase off axis near the inductive heating source. This effect is more prominent in the case with no surface chemistry, where the electron density is higher. The electron density for the case with no surface chemistry (Fig. 5.2(a)) has a peak density of 1.2×10^{11} cm^{-3} and is more uniform in radius than the case with surface chemistry (Fig. 5.2(b)), which has a peak density of 1.0×10^{11} cm^{-3}. The presence of surface reaction products creates additional energy loss mechanisms for the electrons, leading to a slightly reduced electron density for the same power as the case with no surface chemistry.

The surface product densities in the plasma are shown in Fig. 5.3. Since the photoresist is assumed to stick with unit probability on all surfaces, the profile in the plasma is diffusive with the density peaked above the wafer surface where the sputtered photoresist is produced as shown in Fig. 5.3(a). The $SiCl_2$ etch product profile, shown in Fig. 5.3(b), is more uniformly distributed in the central region of the reactor than the photoresist, because the loss rate to the surfaces is much lower in this case, with the wall sticking coefficient is taken to be 0.3. Although this sticking coefficient is relatively small, a large portion of the etch product is lost to the walls before it reaches the pump port. The loss of these products to the walls is essentially the condition which would occur in a clean chamber. After several wafers have been processed, the sputtered photoresist and etch product deposited on the walls will be at a high enough level that re-emission of these products back into the plasma will occur, although a net deposition could still be occurring. Conversely, due to the variation in operations between steady-

state plasma conditions, the walls could be a net source of either particle during a particular phase of operation.

For the clean chamber case, the exposed area of the wafer was varied between 0 and 90% of the patterned area, where 90% of the patterned area corresponds to 0.11% of the total surface area. Within this range, the etch probability, defined as the probability that an ion striking the surface will cause an etch, is shown in Fig. 5.4. It is seen that the etch probability varies linearly with the exposed area. This implies that the amount of exposed, chlorinated silicon is the same for each of these cases. Examination of the fractional coverage of the silicon shows that >95% of the exposed silicon is chlorinated, although roughly 20% of the chlorinated silicon is covered by redeposited photoresist. The high level of chlorination is caused by the fact that the chlorine in the plasma is nearly completely dissociated, and therefore there is much more chlorine available than ions. This causes the etch process to be ion driven, so that the etch rate is dependent primarily on the ion flux, which is uniform across the die.

The fluxes to the wafer for the base case are shown in Fig. 5.5. The ion fluxes to the wafer are peaked off-axis, corresponding to the off-axis peak in the ion density seen in the plasma (Fig. 5.2). Since the sputtering of photoresist off the surface is caused by ion bombardment, the density of sputtered photoresist in the plasma is peaked above the wafer where the ion flux to the surface is largest. This leads to the redeposition flux being peaked off-axis as well, following the ion flux. The Cl flux to the surface is much larger and more uniform than the ion fluxes and the photoresist redeposition flux; because the Cl is much less reactive at the surfaces, its density is more uniformly distributed in the plasma. The fall off at larger radius is caused by the fact that the Cl is diffusing out of the central region toward the pump port where the plasma density is low. In the outer region near the pump port, there is little dissociation and the Cl density falls since recombination at the walls is replenished only by diffusion of Cl from the central region.

The reactive sticking coefficients and return fractions are computed by the MSMCS at a single location on the radius of the wafer; but within the FKS, the values computed are used for the entire wafer surface, so it is expected that there will be some variation of reaction probabilities depending on the radius at which the representative die is located. To examine the impact of this effect, several cases were run in which the radius at which the die was located was varied. The etch probability and the ion flux to the die for these cases are shown in Fig. 5.6. The effective etch probability varies weakly with the position of the representative die and follows the opposite trend of the ion flux. By geometric considerations, assuming 100% chlorination of the silicon and no redeposited photoresist, the maximum etch probability for this case is 0.006, which is approached at the outer radius where the ion flux is the lowest. Etch probability should not be confused with the etch rate, which is the product of the etch probability and the ion flux. For variations with the die location, the main effect is to vary the ion flux to the die, since Cl flux is relatively uniform and very large compared to ion flux (Fig. 5.5). The increase in the effective etch probability with a decrease in ion flux is understood to occur due to two effects. The first effect is that with a lower ion flux and, consequently, a lower etch rate there is a slight increase in the level of chlorination of the silicon surface. The second effect is the redeposition of sputtered photoresist, which has a local flux that somewhat follows the ion flux to the surface. These two effects explain the variation of the etch probability seen in Fig. 5.6.

The reaction probabilities for the sputtering of photoresist and redeposited photoresist can vary in different cases, since the chemical makeup of the photoresist varies for different processes. In addition, even when the photoresist makeup is known, the probability that it and its redeposition will sputter is not well known. Because of this, the effects of variation of the reaction probabilities for the sputtering of photoresist and redeposited photoresist were varied. The etch probabilities for these cases are shown in

Fig. 5.7. The etch probabilities do not vary greatly under these conditions. When the probability of photoresist sputtering is increased while holding the probability of redeposition sputtering constant, the etch probability decreases because the coverage of the etchable area by redeposited photoresist increases. Conversely, the etch probability increases as the sputtering probability of redeposited photoresist increases, since the coverage of the etchable area decreases. If both variables are equal to each other and varied at the same time, the net effect is to decrease the etch probability as the sputtering probability increases, although the changes are even smaller than the effect of varying only one at a time. This is caused by the fact that as the total amount of sputtered photoresist in the plasma volume increases, a larger fraction of the ion flux to the surface must be used in clearing the redeposited photoresist off the surface before etching can occur.

In all the cases so far, the photoresist was assumed to stick to the walls with unit probability. This roughly corresponds to a clean reactor, where resputtering of photoresist off the walls is negligible. In actual operation, the deposition of sputtered photoresist on the walls may never reach an equilibrium condition, since there may be a net deposition throughout the entire operating cycle until the chamber is cleaned. To examine the effects of resputtering from the walls, the code was run with varying probabilities that an ion will sputter photoresist from the walls. The results are shown in Fig. 5.8. The resputter probability from the walls dramatically impacts the etch rate, because an increase in resputtering will increase the load of photoresist material in the plasma, reducing the etch probability from 0.0047 for a "clean" chamber to 0.0024 when the resputter probability is 0.5. In addition, one case was run in which the photoresist was assumed to be in equilibrium with the walls, such that there was no net deposition on the chamber walls, and this is shown as the dotted line in Fig. 5.8. The case yields an etch probability of 0.0023. In most cases, some portions of the wall where there is sufficient

ion flux may come into equilibrium, primarily in the plasma region, although other portions will have a net deposition. In addition, there may be cases in which there is a net source of photoresist from the walls. When there are different processes run in the same chamber, one process may deposit material, which subsequently is sputtered off in a later process, although this condition has not been addressed.

A second test structure, shown in Fig. 5.9, has also been used to look for spatial variations due to loading effects. This structure is intended to cause a reduction in etch rate in the smaller structures near the large open field compared to the structures farther from the open field, similar to the experiment of Hedlund et al.[2] However, since they were using a SF_6 etching chemistry, the loading effect may be more prominent since fluorine has a significant thermal etch component and is less restricted by the ion flux. Because of this, fluorine chemistries are more likely to be in the radical starved regime where the etch rate is determined by the radical flux rather than the ion flux. The operating conditions used for the new test structure were a 50/50 mix of Ar/Cl_2 in the IC-GECRC reactor with 200 W ICP power and a flow rate of 20 sccm at 100 mTorr. The open field is taken to be completely exposed Si, the smaller patterned regions are assumed to be 10% exposed Si; with the rest of the area covered by photoresist and the unpatterned regions completely covered by photoresist. It is found that at these operating conditions, all of the surfaces are almost fully chlorinated. Since the ion flux is assumed to be uniform over the entire region, the local etch rate will depend only on the local level of chlorination, which leads to the result that there is no variation with position found.

The second test geometry was also used for a variety of pressures from 10 mTorr to 200 mTorr. The etch probability for these cases is shown in Fig. 5.10. These results show that the effective etch probability for an ion striking the surface decreases as the pressure decreases. For this geometry the maximum etch probability is 0.1, determined from the geometry and assumed surface reaction probabilities, which explains the

flattening of the curve as the pressure increases from 100 to 200 mTorr. The low-pressure behavior for the etch probability results from a situation similar to the results seen as the test structure was moved to different radius as shown in Fig. 5.6. As the pressure is reduced, the plasma density will increase because, for a given power, the higher pressure cases will achieve equilibrium between the ionization and loss rate of electrons at a lower electron density. This means that the ion flux to the surface will increase with decreasing pressure. A higher ion flux to the surface leads to a situation similar to that shown in Fig. 5.6 in which as the ion flux increases, the etch probability will decrease. In this case, the change is primarily due to the increase in photoresist sputtering and redeposition when the pressure is decreased, causing the ion flux to increase. At the lowest pressures there is also a slight decrease in surface chlorination, but it is not enough to account for the change in etch probability.

5.4. Summary

Surface chemistry and bulk plasma are a coupled system. Surface chemistry products released from the surface can impact the properties of the plasma such as the plasma density. The plasma in turn creates the surface chemistry, including redeposition of species released from the surface. The surface chemistry itself can be altered depending on the mechanics of the reactions at the surface. However, since the mechanics of these processes can vary for different systems and are often not well understood, the ability to perform sensitivity studies is important. In addition, the chemistry at other surfaces in the reactor also plays a role in the chemistry occurring on the wafer surface, and can change with time causing process drift. Variations in pressure cause changes in the surface chemistry by altering the ratio of ions and neutrals to the surface. Under the assumptions used in this model, no variation with position was seen for different regions on the surface. Despite this, modeling of the interactions between

the surface and the bulk plasma provides insights into the operations of an etching tool under more realistic conditions by providing improved boundary conditions to the plasma simulation.

Table 5.1. Reaction chemistry for chlorine etch of polysilicon, with default reaction probabilities and the region of applicability. The mask region is assumed to be covered at all times by a layer of photoresist, while the exposed region is the region of exposed Si, possibly covered with a layer of chlorinated Si or redeposited photoresist.

Reaction	Probability	Region
$Cl_{(g)} \rightarrow Cl_{2(g)}$	0.005	All
$Ion_{(g)} + Photoresist_{(s)} \rightarrow Neutralized\ ion_{(g)} + Photoresit_{(g)}$	0.5	Mask only
$Ion_{(g)} + Redeposited\ Photoresist_{(s)} \rightarrow Neutralized\ ion_{(g)} + Photoresit_{(g)}$	0.5	Exposed only
$Ion_{(g)} + SiCl_{2(s)} \rightarrow Neutralized\ ion_{(g)} + SiCl_{2(g)}$	0.5	Exposed only
$Cl^{+}_{x(g)} + Si_{(s)} \rightarrow \frac{x}{2} SiCl_{2(s)}$	1.0	Exposed only
$Cl_{(g)} + Si_{(s)} \rightarrow \frac{1}{2} SiCl_{2(s)}$	0.2	Exposed only

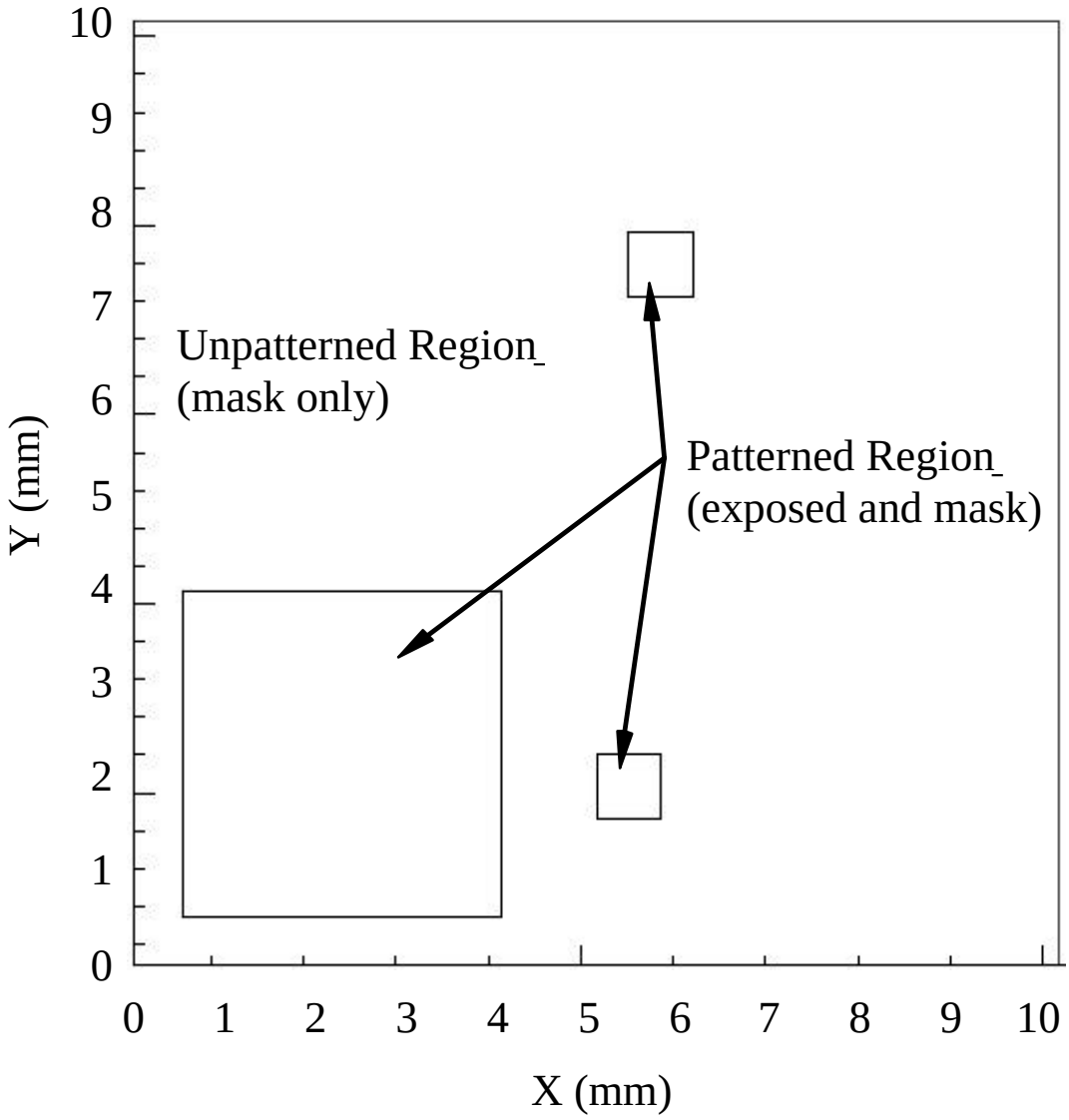

Fig. 5.1. Test structure for a surface die. The patterned areas have 10% exposed Si with the remainder covered in photoresist. The unpatterned areas are completely covered in photoresist.

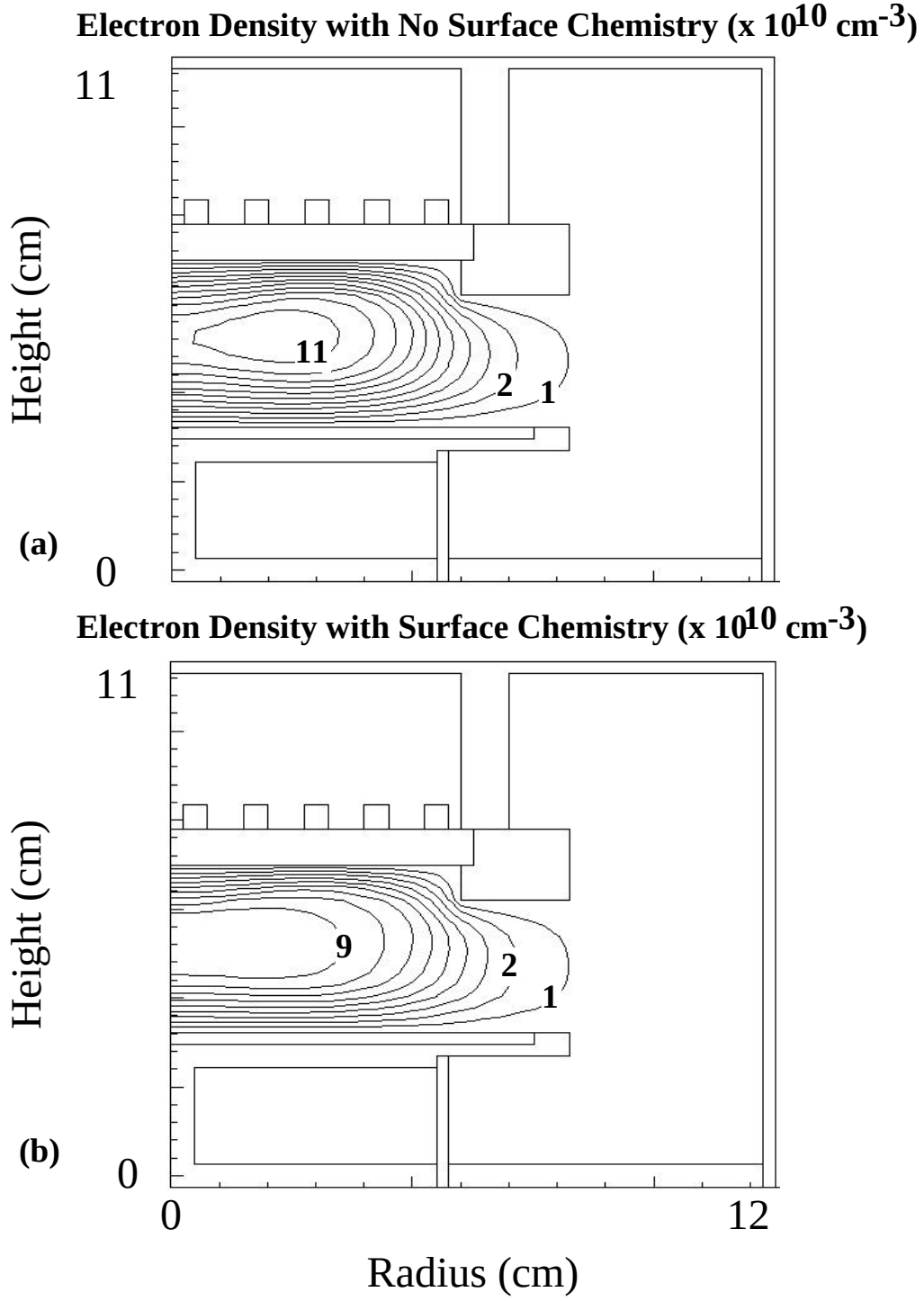

Fig. 5.2. Electron for a 10 mTorr, 10 sccm, 50/50 Ar/Cl_2 mixture with 100 W inductively coupled power, (a) with no surface chemistry, (b) with the MSMCS using the polysilicon etch chemistry. The introduction of surface products into the bulk plasma reduces the electron density.

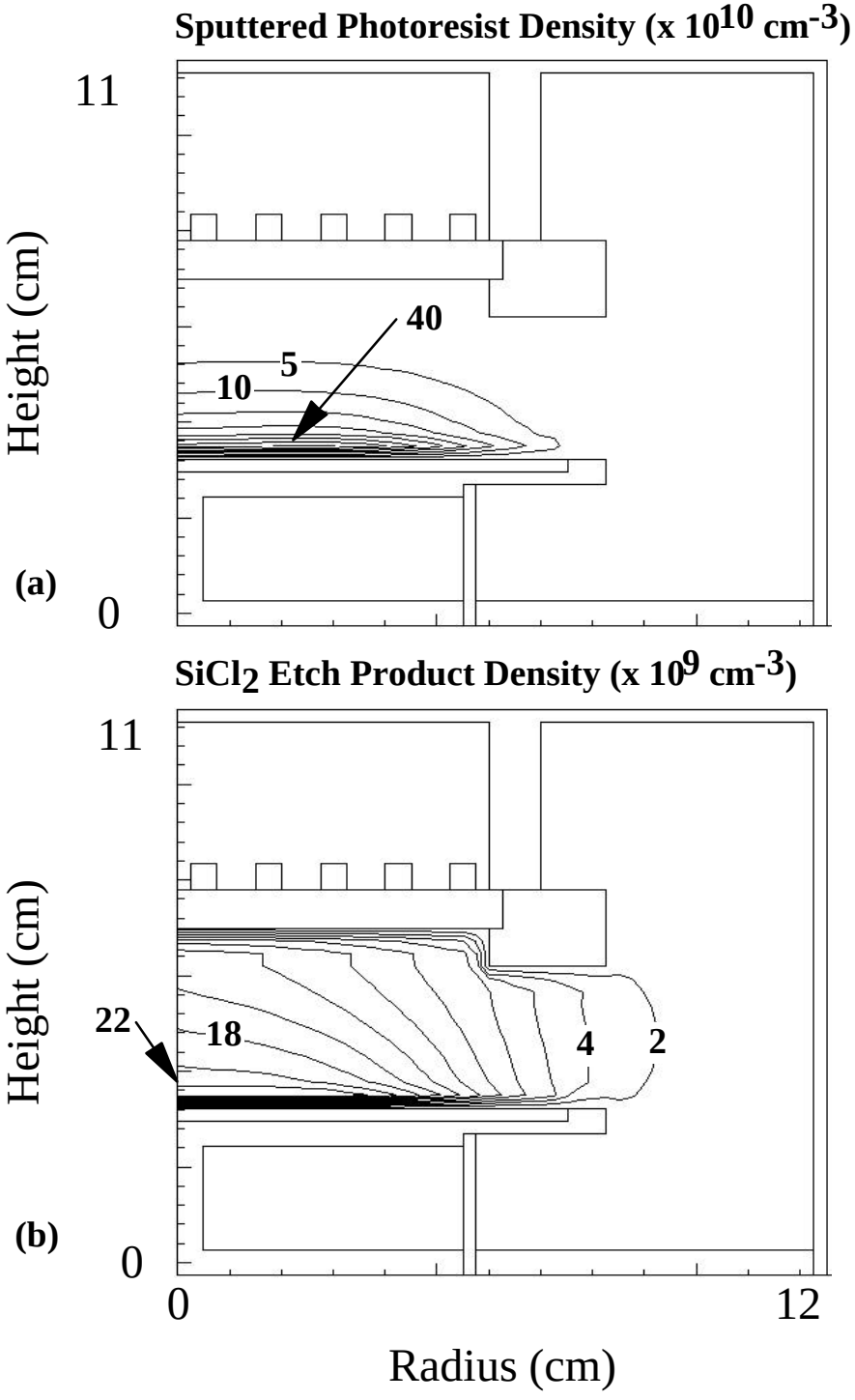

Fig. 5.3. Surface product densities in the reactor volume. (a) Sputtered photoresist density. (b) Etch product, $SiCl_2$, density. The products are produced at the wafer surface and have diffusive profiles.

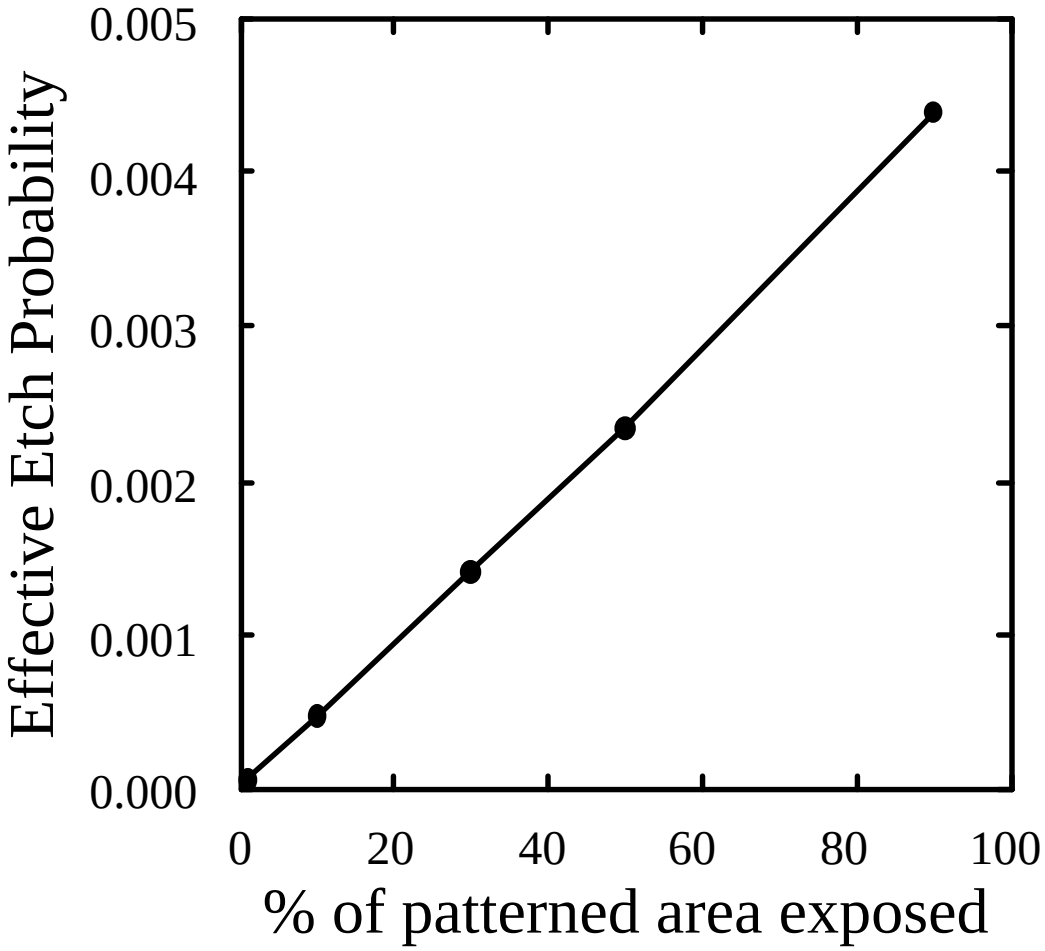

Fig. 5.4. Etch probability verses the percentage of the patterned area which is exposed for etching where the patterned area is 12% of the total area. The etch probability varies in a nearly linear fashion with the exposed area since the etch process in this case is ion driven.

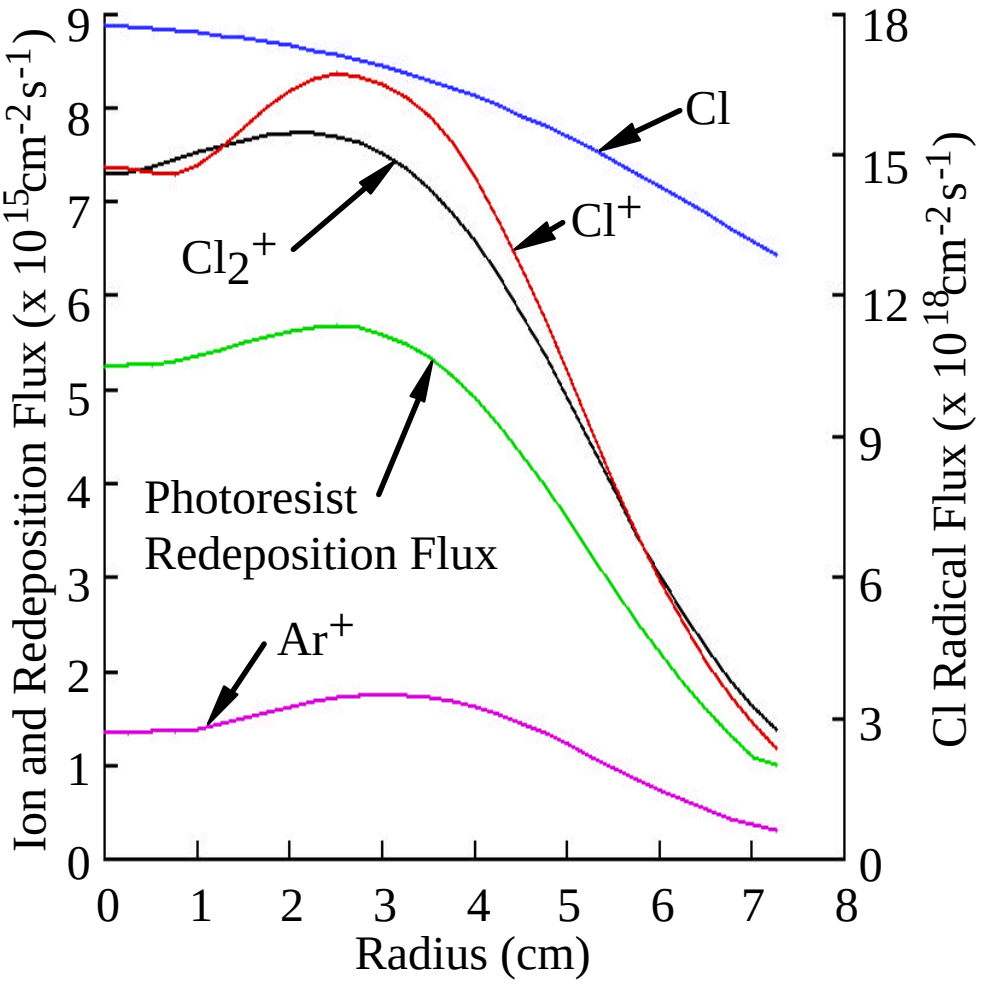

Fig. 5.5. Ion, photoresist redeposition and Chlorine radical fluxes to the wafer surface for the standard case as a function radius. Charged particle fluxes are peaked off axis. This leads to a sputtered photoresist flux which is peaked off axis. Cl atom flux is more uniform, but falls off at the edge of the plasma.

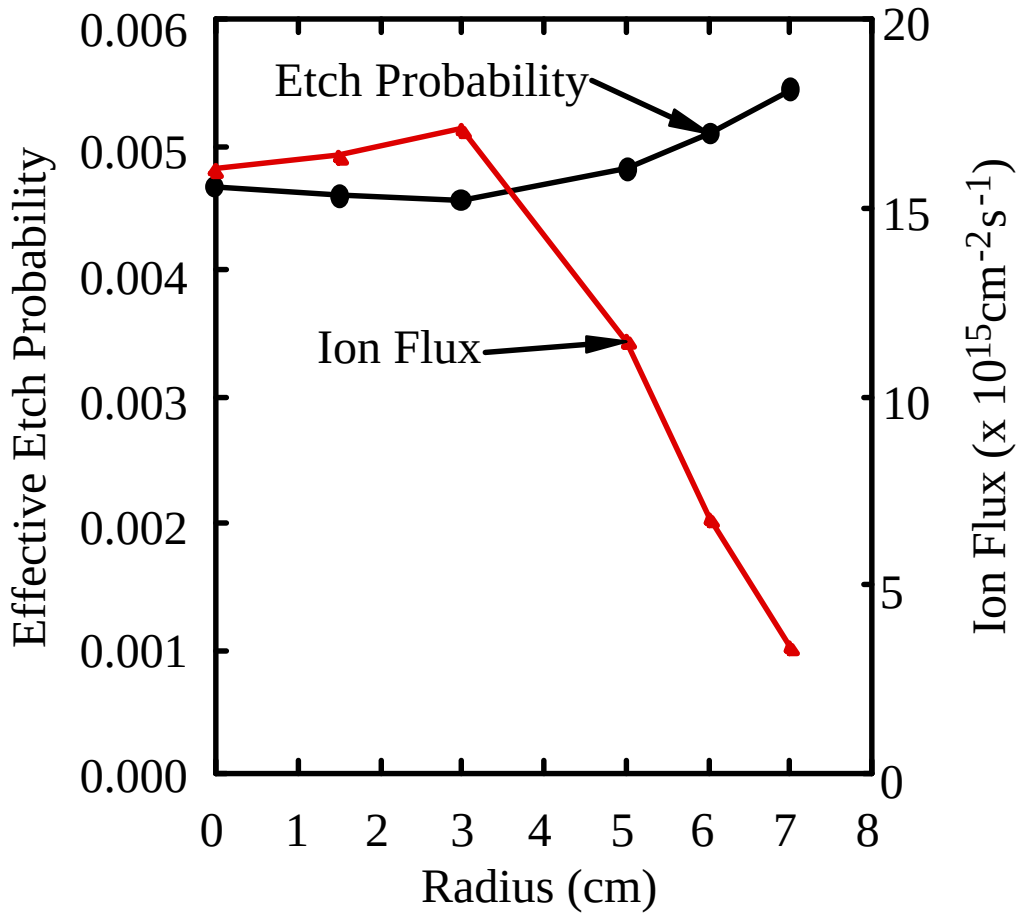

Fig. 5.6. Etch probability and ion flux to the surface as a function of radius. The etch probability increases slightly as the flux decreases, although the etch rate, which is the product of ion flux and etch probability, closely follows the ion flux.

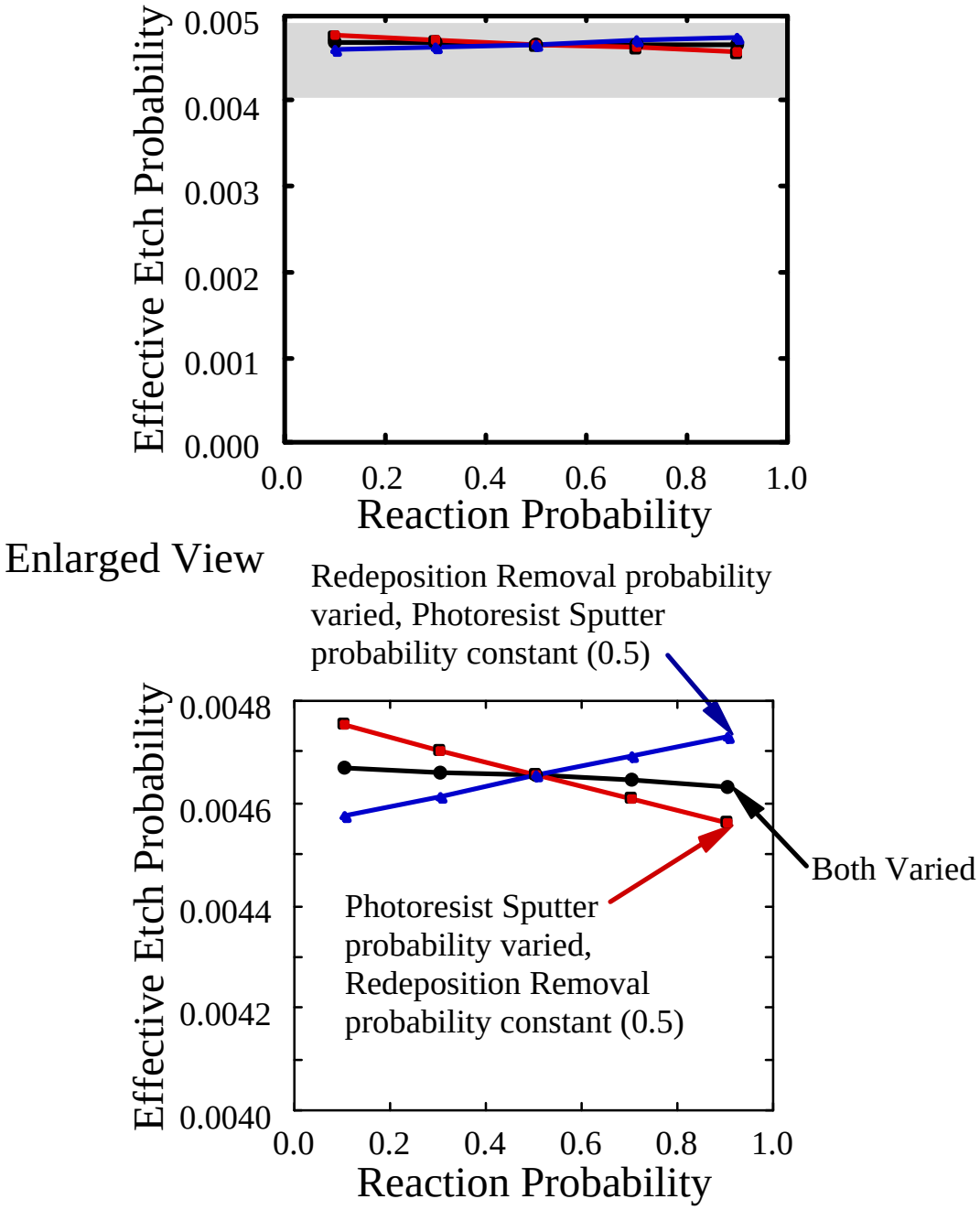

Fig. 5.7. Etch probability as a function of the reaction probabilities for redeposition removal and photoresist sputtering. The triangles represent the variation as the redeposition probability is varied while the photoresist sputter probability is held constant. The squares represent the variation as the photoresist sputter probability is varied while the redeposition removal rate is held constant. The circles represent the variation which occurs when the two values are kept equal and varied at the same time.

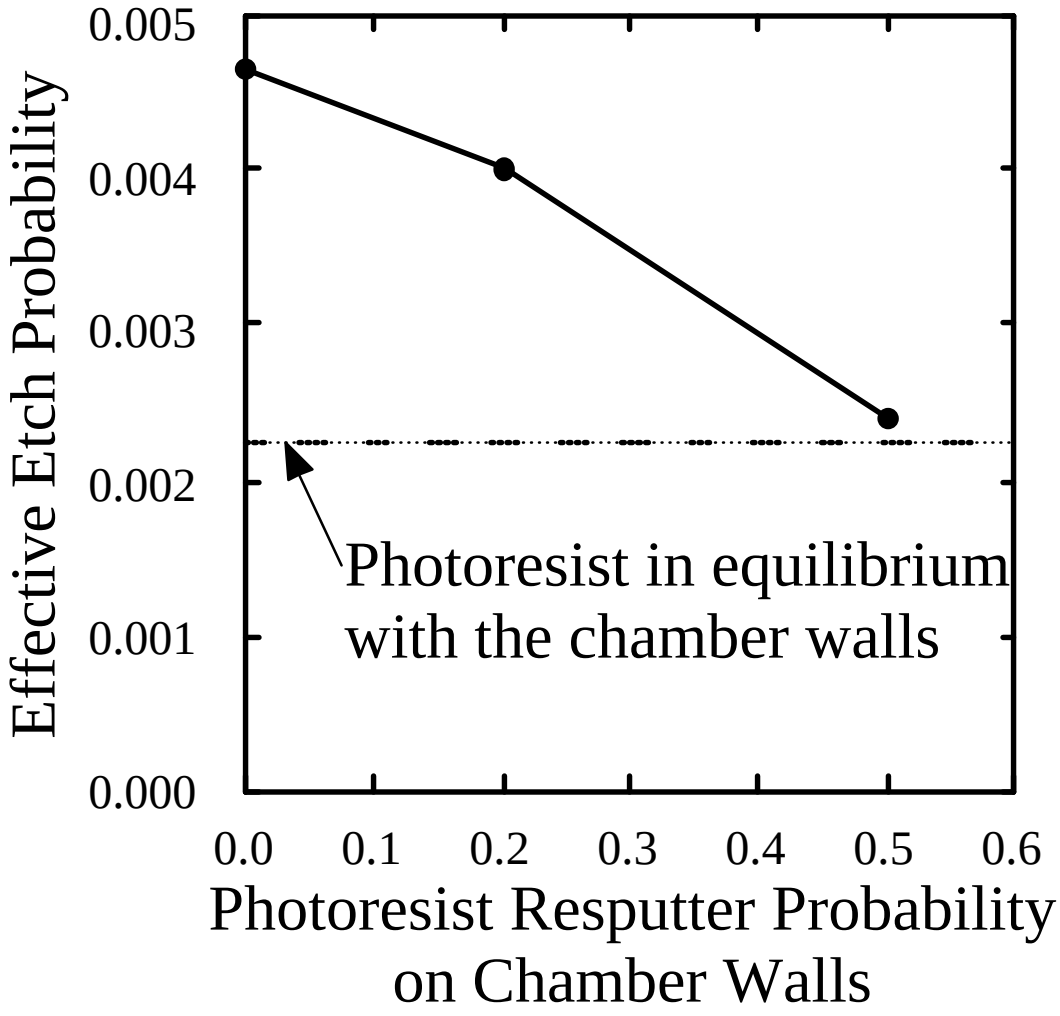

Fig. 5.8. Etch probability as the photoresist resputter probability on the walls is varied. A value of zero represents the case where photoresist sticks to the walls and does not resputter. The dotted line is the value obtained when the photoresist is assumed to be in equilibrium with the walls so that there is no net deposition.

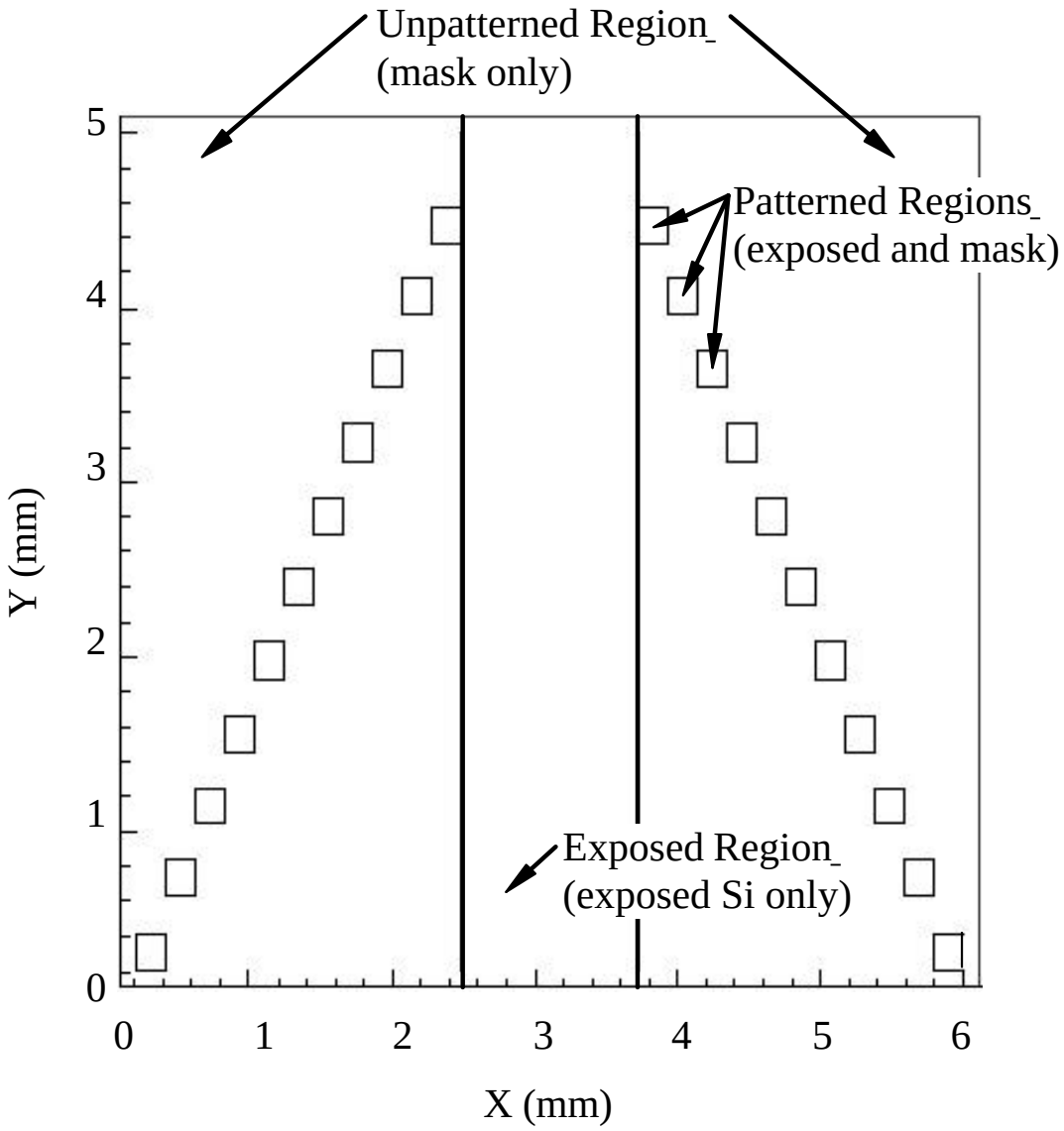

Fig. 5.9. Second test structure for a surface die. The central open field is completely exposed Si, while the smaller structures on the sides have 10% exposed Si and the remainder of the surface is covered by photoresist. The exposed areas here are nearly fully chlorinated.

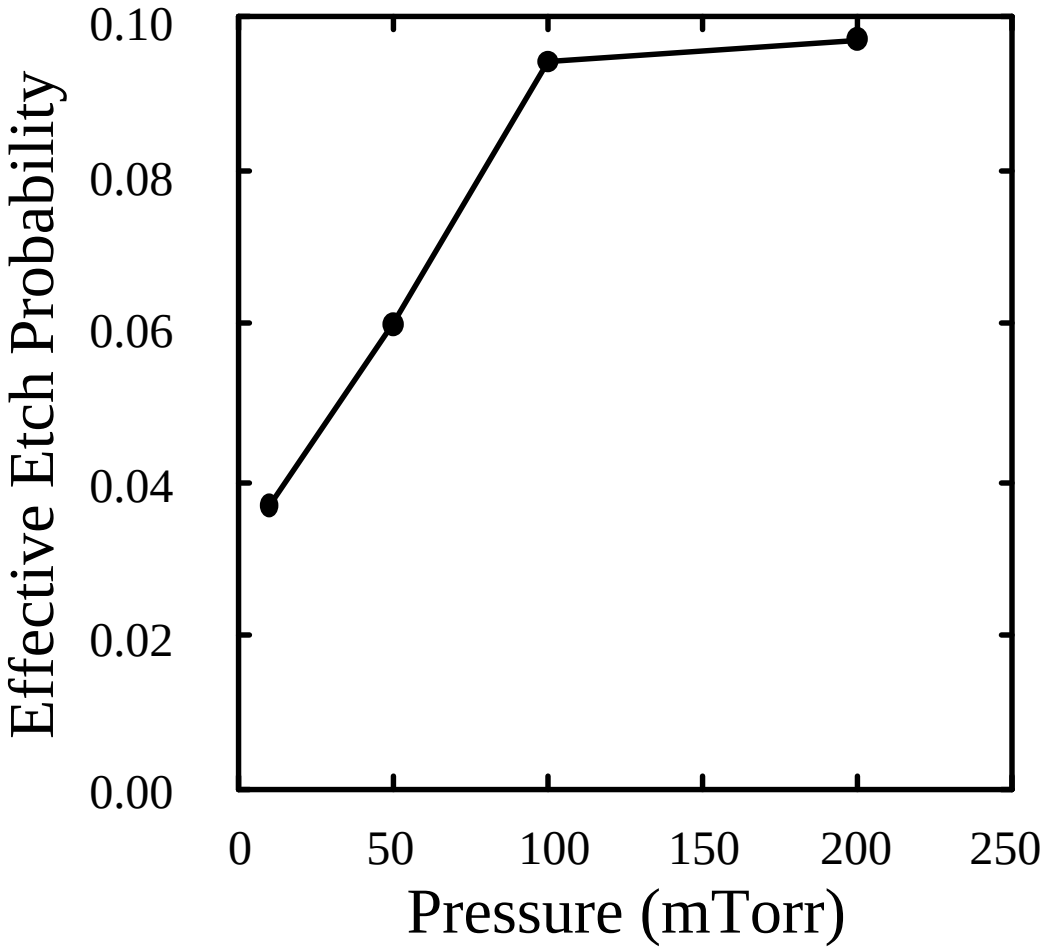

Fig. 5.10. Variation of the etch probability with gas pressure.

5.5. **References**

[1] P. A. Miller, G. A. Hebner, K. E. Greenberg, P. D. Pochan and B. P. Aragon, *J. Res. Nat. Inst. Stds. Tech.* **100**, 427 (1995).

[2] C. Hedlund, H.-O. Blom, and S. Berg, *J. Vac. Sci. Technol. A*, vol. 12, p. 1962, 1994.

6. CONCLUSIONS

Plasma equipment modeling has taken on increased importance in the design of plasma equipment as the cost of these tools has risen sharply in recent years. Modeling gives the ability to design an effective tool more quickly, saving time and money. The ability of a model to accomplish this requires that the physics of the plasma modeled is represented realistically, which necessitates the modeling of the disparate length and time scales present in these plasmas. To this end, the HPEM has been improved by the inclusion of several physics models.

Accurate representation of the radio frequency (rf) sheath has been implemented. This was accomplished by tracking the total charge in the sheath region as a function of time, and then using a one-dimensional analytic sheath model to join the surface to the plasma region. Inclusion of the sheath model in the plasma equipment model was shown to improve predictions of the plasma potential and the plasma density. In addition, inclusion of the sheath model gives more realistic two-dimensional distributions within the reactor, which are typically more uniform than those predicted without the sheath model. With the use of the sheath model, the uniformity of ion fluxes to the wafer was seen to be relatively uniform. Uniformity of the flux to the surface was seen to scale primarily with the applied capacitive bias power, while the magnitude of the ion flux depended primarily on the inductively coupled power.

Modeling of an ionized metal physical vapor deposition (IMPVD) system was also performed. Sputtering of atoms from surfaces in the plasma tool, as well as, their kinetic transport and slowing in the plasma volume, was incorporated by using a Monte Carlo simulation to generate a Green's function for the slowing-down location of an atom sputtered from a given source location. The total source of sputtered atoms to the fluid simulation and fast neutral fluxes to the wafer were then determined using the total flux

of ions and hot neutrals to each source point and the input sputter properties convolved with the Green's function. In addition, the motion of electrons in the strong magnetic field region near the cathode was improved by modification of the time-stepping algorithm in the electron Monte Carlo module.

In IMPVD systems, a clear transition is seen as the pressure is increased. At low pressure, a majority of sputtered atoms traverse the reactor volume with few collisions and strike the wafer or walls without thermalizing. As the pressure increases, sputtered atoms are slowed in the reactor volume and ionized before deposition on the wafer. However, increases in pressure result in additional diffusive losses to surface, resulting in a lower total deposition rate for a given sputter rate. In addition, the immersion of the coils in the plasma results in capacitive coupling of the coils, which can generate a dc self bias that can accelerate ions, causing sputtering of the coils. This can be complicated by the fact that the plasma density may be largest in the plasma because of the inductive power deposition of the coils. Sputtering of the coils was seen to be a significant contribution of sputtered material in the plasma, leading to nonuniformities in the deposition flux, and could contribute to a decreased lifetime for the coils themselves.

A self-consistent model coupling the die-scale surface chemistry to the bulk plasma was also developed. This was done by implementing a Monte Carlo simulation to track ion and reactive species as they travel to and react with the surface and release products back into the bulk plasma. Surface chemistry is resolved on the die scale, with position-dependent surface coverage tracked through the simulation. Boundary conditions for the ions and reactive species in the fluid simulation were updated based on the species returning to the plasma from the Monte Carlo simulation, thus capturing the effects of pattern density and surface coverage.

The bulk plasma is influenced by the presence of the surface chemistry through release of etching products and sputtering of photoresist material. This was seen to

decrease plasma density and impact uniformity. In addition, the presence of these products in the plasma affects the surface chemistry by changing reactant and ion fluxes to the surface and through redeposition of sputtered photoresist on the surface. The effects of the state of the reactor chamber itself was examined, and it was seen that as the chamber becomes more seasoned, causing a reduction in the net deposition on the walls, the etching rate is decreased. Variations with pressure show that as the pressure decreases, the etch probability per ion decreases, although the total etch rate increases because of the higher plasma density at lower pressure for a fixed power. No variations with position were seen for the surface chemistry, operating conditions and assumptions used in this model.

Modeling of plasma processing equipment has become increasingly sophisticated, representing more plasma scales present in the plasma as well as more coupling between these scales. As computing power increases, even more accurate representations can be made which can yield results in an amount of time reasonable for use in the design cycle of a plasma processing tool.

VITA

Michael Grapperhaus was born in Breese, Illinois, in 1969. He attended Southern Illinois University at Edwardsville and then the University of Illinois at Urbana-Champaign, where he received his B.S. degree in May 1991. He also received his M.S. at the University of Illinois at Urbana-Champaign in May 1993. He has studied fueling of magnetically confined fusion reactors, plasma arc railgun armatures, and under the direction of Professor Mark J. Kushner, plasma processing equipment. His work has resulted in six reviewed papers and five conference presentations. He is an Oak Ridge Institute for Science and Education Magnetic Fusion Science fellow, a member of the American Physical Society and IEEE, and of the Alpha Nu Sigma and Tau Beta Pi honor societies.